



THÈSE

Pour obtenir le grade de
Docteur

Délivré par l'**Ecole Nationale Supérieure de Chimie
de Montpellier**

Préparée au sein de l'école doctorale 459 Sciences
Chimiques Balard
Et de l'unité de recherche UMR3080 LSFC

Spécialité : Chimie et Physico-Chimie des Matériaux

Présentée par **Corinne SALLES**

Performances et vieillissement de membranes céramiques à transport d'oxygène

Soutenue le 15/02/2018 devant le jury présidé par David CORNU
et composé de

| | | |
|----------------------------|----------------------------|--------------|
| M. Henny BOUWMEESTER, Pr. | Univ. Twente (Netherlands) | Rapporteur |
| M. Truls NORBY, Pr. | Univ. Oslo (Norway) | Rapporteur |
| M. Sylvain DEVILLE, Dr. | LSFC, Cavaillon | Directeur |
| M. Daniel MARINHA, Ir. | LSFC, Cavaillon | Co-encadrant |
| M. Marlu César STEIL, Ir. | LEPMI, Grenoble | Co-encadrant |
| Mme Florence ANSART, Pr. | Cirimat, Toulouse | Examinatrice |
| M. David CORNU, Pr. | ENSCM, Montpellier | Examinateur |
| Mme Caroline PIROVANO, Mdc | UCCS, Lille | Examinatrice |
| M. Jacques FOLETIER, Pr. | LEPMI, Grenoble | Invité |



Résumé

Les membranes à transport d'oxygène (OTM) sont des membranes céramiques denses qui sont capables de transporter l'oxygène de manière totalement sélective à travers un gradient de pression partielle d'oxygène. Elles peuvent être utilisées pour diminuer les émissions de gaz à effet de serre dans le cadre de la capture et du stockage du CO₂ ou pour augmenter l'efficacité de l'oxydation partielle du méthane. La semi-perméabilité de l'oxygène est proportionnelle à la conductivité ambipolaire du matériau. Cependant, les OTM avec des conductivités ambipolaires élevées sont plus susceptibles de se dégrader rapidement dans les conditions d'utilisation. Pour être compétitives, les OTMs doivent donc remplir plusieurs critères, notamment avoir un flux élevé mais être aussi stables chimiquement, thermiquement, mécaniquement et être peu chères. CaTi_{0.9}Fe_{0.1}O_{3-δ} (CTF) a été récemment présenté comme étant un matériau prometteur pouvant remplir ces critères et mérite d'être étudié plus en détail.

Cette thèse se focalise sur les performances (mesurées par le flux d'oxygène) et la stabilité chimique et thermique du CTF. Pour améliorer les performances d'une membrane, il est nécessaire de savoir si la semi-perméation est limitée par les réactions en surface ou par la diffusion en volume. Les premiers résultats de ces travaux détaillent les étapes limitantes du transport de l'oxygène dans le CTF. En particulier, grâce à un montage expérimental spécifique et des expériences complémentaires, il a été montré que le CTF est limité à la fois par la diffusion en volume et les réactions de surfaces pour T < 750 °C mais est majoritairement limité par la diffusion en volume à plus haute température. Les chapitres suivants détaillent la diffusion dans le volume et la conductivité électrique en fonction de la pression partielle d'oxygène et de la température, au vu de la chimie des défauts du CTF. Dans les conditions de fonctionnement, le CTF doit être considéré comme étant un conducteur mixte, avec une conductivité ionique qui devient prédominante pour des températures supérieures à 800 °C.

La seconde partie est consacrée à l'étude de la stabilité du CTF sous des atmosphères réactives, spécifiques aux OTM, qui sont connues comme provoquant des dégradations pour certains matériaux. Des tests de vieillissement sous atmosphères de CO₂, CO, H₂ n'ont montré aucune dégradation du flux de semi-perméation sur plusieurs centaines d'heures. Seulement une légère diminution du flux (- 35%) a été observée en présence de CO₂ et de vapeur d'eau mais après cent heures sous hélium, le flux initial a été retrouvé. Des analyses DRX, MEB et Raman post-mortem n'ont révélé aucun signe notable de dégradation en surface et dans le volume. Un test sous CH₄ a également été effectué, et la formation de CO, CO₂, H₂ et H₂O a été suivie pendant des centaines d'heures. Malgré la présence de ces gaz réactifs, la même valeur du flux de semi-perméation a été retrouvée après 1000 heures de test sous méthane, témoignant d'une très bonne stabilité du CTF dans ces conditions réductrices.

En conséquence, malgré des valeurs de flux relativement faibles (5×10^{-3} mL.min⁻¹.cm⁻¹ à 900 °C), ce matériau est plein de promesse et son excellente stabilité sous méthane notamment peut être très intéressante pour certaines applications.

Mots clés

Membranes céramiques, OTM, vieillissement, électrochimie du solide, CTF

Abstract

Oxygen transport membranes (OTM) are dense ceramic membranes that allow oxygen diffusion along a chemical potential gradient. OTMs can increase the efficiency of oxycombustion processes or partial oxidation of methane, resulting in lower CO₂ emissions overall. The oxygen transport is proportional to the ambipolar conductivity of the OTM material. However, OTM materials with the highest ambipolar conductivity are more prone to fast degradation under operation conditions. To be competitive, OTMs must associate high oxygen transport properties but also must be chemically, thermally, and mechanically stable, and preferably not expensive. CaTi_{0.9}Fe_{0.1}O_{3-δ} (CTF) has recently been shown to match these demands, appearing as a promising OTM material that is worth studying in further detail.

This PhD is therefore dedicated to study the performance and stability of CTF in typical operation conditions of an OTM. To improve the performance of a membrane, it is necessary to determine if the semi-permeation is limited by surface exchange reactions or by bulk diffusion. The first results of this work will detail the nature of the limiting reaction step for oxygen transport in CTF. Specifically, CTF is co-limited by bulk diffusion and surface exchange reactions at $T < 750$ °C, but is mainly limited by bulk diffusion at higher temperatures. The following chapter details the bulk diffusion process and electrical conductivity in light of the defect chemistry of CTF, as a function of oxygen partial pressure and temperature. Under typical operation conditions, CTF must be regarded as a mixed ionic and electronic conductor, with increasing predominance of ionic conductivity at $T > 800$ °C.

The second part is dedicated to the stability of the CTF under atmospheric compositions typically found in standard operating conditions, known to degrade the performance of usual membrane materials. The oxygen transport of CTF is shown to remain stable under CO₂, CO, and H₂ atmospheres over several hundred hours. Some degradation (- 35% of oxygen semi permeation flux) was observed when exposed to humidified CO₂, but returning to initial values when exposed to dry helium for a hundred hour. Post-mortem XRD, SEM and Raman analyses did not show any obvious signs of surface or bulk degradation. CTF was tested for CH₄ oxidation for a thousand hours and the formation of CO, CO₂ and H₂O was followed. Despite this reactive environment, the oxygen transport CTF membrane fully regenerates upon returning to helium atmosphere.

Therefore, despite relatively low performance (5×10^{-3} mL.min⁻¹.cm⁻¹ at 900 °C), this material is full of promises and especially its outstanding stability under methane can be very interesting for some applications.

Keywords

Ceramic membrane, OTM, stability, solid state electrochemistry, CTF

ACKNOWLEDGEMENTS

Ce travail de thèse a été effectué au laboratoire de Synthèse et de Fonctionnalisation des Céramiques (LSFC, UMR 3080) à Cavaillon, grâce au support financier de l'ANRT et de la société Saint-Gobain.

My acknowledgements first concern both the opponents of this thesis, Professor Henny Bouwmeester and Professor Truls Norby. I am honored they accepted to spend time evaluating this work and for their interest with respect to this thesis subject.

Je remercie également les autres membres du jury, Florence Ansart, David Cornu et Caroline Pirovano venus parfois de loin pour juger ce travail.

Je remercie Sylvain Deville, El director, pour avoir accepté d'être le directeur officiel de cette thèse et pour nos discussions « nourritures et Valrhona ».

Cette thèse a été effectuée en partie au LEPMI à Grenoble sous la direction de César Steil et de Jacques Fouletier. Je les remercie chaleureusement d'avoir accepté de participer à cette thèse et d'avoir répondu à mes nombreuses questions. Je suis notamment très honorée d'avoir eu la chance d'être du coup une des dernières thésardes que Jacques aura « encadrée ». Je remercie également Sandrine Baudin qui m'a énormément aidée au début sur le montage expérimental ainsi que Etienne Omnès.

Je remercie aussi chaleureusement Daniel Marinha qui m'a encadrée à Cavaillon au LSFC. Merci du temps que tu as pris pour les discussions que nous avons eues et pour ton aide. Nous n'avons pas forcément les mêmes caractères mais ces 3 années à travailler avec toi ont été extrêmement agréables et enrichissantes et m'ont permis d'apprendre énormément.

Je souhaite également remercier toutes les personnes avec qui j'ai pu collaborer au cours de cette thèse. Jean-Marc Bassat, merci pour les mesures d'échange isotopique et les discussions que nous avons eues, notamment lors du congrès à Padoue. Un immense merci également pour avoir trouvé une erreur dans l'article et donc dans le manuscrit juste à temps... Merci également de nous avoir mis en contact avec Alain Wattiaux qui a réalisé les mesures de spectroscopie Mössbauer pour nous et je l'en remercie. Merci également à Pascal Roussel pour les mesures de DRX et d'ATG sous hydrogène.

Au labo-mixte, je remercie Caroline Tardivat qui m'a accueillie dans son laboratoire et sans qui cette thèse n'aurait pas été possible. Je remercie les autres chercheurs actuels ou présents durant ces 4 années : Adam, Helena et Michaela. Je remercie aussi les techniciens du labo, Stéphane et Dany, pour le travail fait ensemble, mais aussi pour les nombreuses discussions et pactes en tout genre que nous avons eus. Je remercie également Claire et Régine qui occupent (ont occupé) une place importante bien que pas très visible au sein du labo.

Je remercie bien sûr les doctorants et post-doctorants que j'ai croisés tout au long de cette thèse : P-A ou Puky plutôt, je ne retiendrai pas forcément les découvertes culinaires à base de tarama au petit déjeuner mais merci pour ces années, ces jeux de société, parties de badminton, etc... c'est toi

le prochain du labo donc bon courage ; Zane, tu resteras la seule fille de la plateforme, ne te laisse pas faire ! Sidhanth et Hassan, vous êtes les petits derniers, bon courage, occupez-vous bien du café et tout se passera bien ! Rémi merci d'avoir pris le relais des jeux de mots et blagues en tout genre sur la plateforme, ça se perdait un peu avant ton arrivée ! Merci également à Mangesh et Félix que, rédaction oblige, je n'ai pas trop eu le temps de connaître vraiment, et aussi merci à Jordi, Dmytro, Khadija, Jean-Matthieu et les stagiaires successifs !

Bien sûr un immense merci à mon co-thésard Amin ! On s'est mutuellement supporté pendant ces presque 4 années ! Merci d'avoir rendu cette aventure aussi belle ! Les amis c'est là dans les bons et mauvais moments, merci d'avoir été là dans les deux cas. Il y a des souvenirs qui resteront toujours gravés dans ma mémoire (notamment les craquages de la période de rédaction !!) et n'oublions pas, c'est toujours mieux mais pas la chouette ! Encore un énorme merci !

Je souhaite également remercier Benoit Watremetz et Franceline Villermaux qui m'ont respectivement choisie et encadrée lors de mon stage de fin d'études au CREE et sans qui je n'aurais certainement pas eu cette offre de thèse.

Je remercie vivement également les différentes personnes du CREE, notamment Anthony pour sa gentillesse tout au long de ces 4 années, sa disponibilité et sa passion partagée pour le badminton, Christophe pour le partage du bureau quand j'étais en stage, Brice pour les analyses de PSD notamment, ainsi que Laura, Lionel, Sébastien et les autres pour les bons moments au CREE ou en dehors (remplis de badminton, de jeux de société et de gâteaux au chocolat entre autres). Merci également à Pascal et à son équipe pour le restaurant d'entreprise qui permet de bien remonter le moral, avec toujours plus de desserts notamment faits avec du chocolat Valrhona !

Je remercie mes amis venus assister à la soutenance, Mathilde et Thibaut. Merci d'avoir été là essentiellement lors de ces derniers moments et maintenant pas le choix on se serre les coudes Thibaut et on va s'en sortir ! Merci à Guillaume également. Je pense aussi à ceux qui n'ont pas vu venir parce que trop loin (Anne-Marie), ou occupée (Fanny tu as eu une bonne raison, bienvenu Alexander !).

Enfin, je remercie mes parents, qui m'ont soutenue et sont venus avec ma sœur pour assister à la soutenance et m'ont écoutée de nombreuses heures assez incompréhensibles pour eux.

Pour terminer, je souhaite dédier cette thèse à Florian qui, en quelque sorte, était quand même là avec nous.

GENERAL INTRODUCTION

In the current situation, especially after the Paris agreements, it is important to keep finding a way to limit the increasing global warming and to decrease CO₂ emissions. In addition to the development of renewable energies, it is interesting also to develop the Carbon Capture and Storage (CCS) technology, which is one of the solutions to fulfill the commitments taken in term of maximal global warming [1]. One of the key steps of this technology is the separation of oxygen from air, which is usually performed with cryogenic air separation. However, this technique decreases the efficiency of a power plant by around 8–10% [2]. Oxygen transport membranes (OTMs) are being studied as alternative to cryogenic air separation and can also be used as catalytic membrane reactor (CMR), combining several stages of the CCS process.

Oxygen transport membranes (OTM) are dense ceramic that are able to selectively transport high-purity oxygen through a mechanism of oxygen vacancy and electronic defects diffusion along a chemical potential gradient (Figure 1).

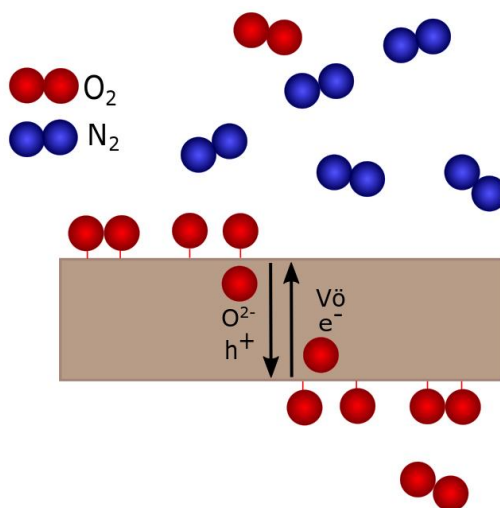


Figure 1: Schematic representation of a mixed ionic-electronic OTM.

First, oxygen adsorbs on the surface of the membrane then dissociate to form O²⁻ ions. These ions diffuse through the material and there is an electron flux in the opposite direction to maintain charge neutrality. The oxygen transport is related to the ambipolar conductivity of the OTM material but the surface exchange reaction will also influence the semi-permeation flux performance of the OTM.

The study presented in this manuscript is the result of a cooperation between the Ceramic Synthesis and Functionalization Laboratory which is a joint CNRS / Saint-Gobain research unit, doing fundamental research on functional ceramic materials, and the LEPMI laboratory (Laboratory of Electrochemistry and Physical-chemistry of Materials and Interfaces) of the University Grenoble Alpes.

This PhD focuses mainly on two aspects of the OTM: the mechanisms of oxygen transport, and its long-term stability near operation conditions. To be competitive, OTMs must associate high oxygen transport properties but also must be chemically, thermally, and mechanically stable, and preferably not expensive and respect green chemistry. However, OTM materials with the highest semi-permeation performances are more prone to fast degradation under operation conditions. Consequently, this study was focused on the CaTi_{1-x}Fe_xO_{3-δ} (CTF), which offers a reasonable compromise between performance and long-term stability, making it a good candidate for the rigorous conditions of industrial applications.

One important part of this study is focused on the oxygen semi-permeation flux, especially on the role of both surface and bulk. Indeed, to improve performance, it is important to determine whether the oxygen transport process is limited by surface exchange or by bulk diffusion. Among other experiments, a specific setup developed in the LEMPI was used to experimentally determine the limiting step. Another important part of this study is the characterization of the CTF stability, especially its long-term stability under reactive atmospheres.

This manuscript is organized in seven chapters. The first chapter is a brief literature review on OTMs and perovskites. Chapter 2 details the experimental setups and procedures used for the oxygen semi-permeation and characterization of the different samples. The third chapter presents some classical characterization of the CTF powder and membranes. The semi-permeation results and the identification of the limiting step are presented in Chapter 4 along with experiments on a surface modified pellet. The role of the surface polarization is studied in more detail and oxygen diffusion is also analyzed, independently from the surface reaction. This leads to question on the defect chemistry of the CTF. Chapter 5 is dedicated to the defect chemistry of the CTF, especially of its conductivity to explain results obtained during semi-permeation experiments. The long-term stability under non-reactive and reactive atmospheres is studied in Chapter 6, especially under 1% CO₂, 2% CO, and 3% H₂. The presence and effect of carbonate as well as the effect of the reducing atmosphere on the lean side are then studied. The steam effect is also investigated. Finally, a study on the stability under methane and the observation of the oxidation of methane is completed to give a first idea on the potential application of the CTF. Finally, the conclusion and perspectives are summarized.

[1] IPCC, Climate Change 2014 Synthesis Report Summary Chapter for Policymakers, Ipcc. (2014) 31.

[2] A.C. Bose, G.J. Stiegel, P.A. Armstrong, B.J. Halper, E.P. Foster, Chapter 1: Progress in Ion Transport Membranes for Gas Separation Applications, 2009.

| | |
|----------------------------------|----------|
| RESUME | 3 |
| ABSTRACT | 4 |
| AKNOLEDGMENTS..... | 5 |
| GENERAL INTRODUCTION..... | 7 |
| TABLE OF CONTENT..... | 9 |

CHAPTER 1: LITERATURE REVIEW

| | |
|--|----|
| 1. Context | 14 |
| 2. OTMs | 17 |
| 2.1 Fundamentals | 17 |
| 2.1.1 Oxygen transport limited by oxygen bulk diffusion..... | 18 |
| 2.1.2 Oxygen transport limited by surface exchange reactions | 19 |
| 2.1.3 Mixed-limited regime | 19 |
| 2.1.4 OTM requirements | 20 |
| 2.2 State of the art..... | 21 |
| 3. Perovskites..... | 23 |
| 3.1 Electrical properties of perovskites | 23 |
| 3.1.1 Oxygen–ion conductivity | 23 |
| 3.1.2 Electronic conductivity..... | 24 |
| 3.1.3 Oxygen semi-permeability | 25 |
| 3.2 Stability | 25 |
| 3.3 CTF | 27 |

CHAPTER 2: EXPERIMENTAL SECTION

| | |
|---|----|
| 1. Introduction..... | 38 |
| 2. Oxygen permeation setups..... | 39 |
| 2.1 Standard setups | 39 |
| 2.2 Electrochemical surface probes..... | 42 |
| Reactivity test between YSZ and CTF | 45 |
| 3. Isotopic exchange | 47 |

| | | |
|----|--------------------------------|----|
| 4. | TPR measurements..... | 48 |
| 5. | Impedance spectroscopy..... | 49 |
| 6. | XRD | 50 |
| 7. | Redox stability potential..... | 51 |
| 8. | Mössbauer spectroscopy..... | 52 |

CHAPTER 3: CTF CHARACTERIZATION

| | | |
|----|---------------------------------|----|
| 1. | Introduction..... | 57 |
| 2. | Powder characterization..... | 58 |
| 3. | Membrane preparation | 62 |
| 4. | Porous layer..... | 63 |
| 5. | Modified Pechini synthesis..... | 64 |
| 6. | Conclusion | 69 |

CHAPTER 4: CTF SEMI-PERMEABILITY

| | | |
|-----|--|----|
| 1. | Introduction..... | 73 |
| 2. | Oxygen permeation measurements..... | 74 |
| 3. | Identifying the limiting step..... | 76 |
| 3.1 | Critical thickness obtained by isotopic exchange | 76 |
| 3.2 | B_c number obtained with electrochemical probes..... | 77 |
| 3.3 | Effect of a porous layers on the limiting steps | 79 |
| 4. | Oxygen transport mechanisms within the bulk..... | 83 |
| 5. | Surface polarization study | 85 |
| 6. | Conclusion | 87 |

CHAPTER 5: CTF DEFECTS

| | | |
|-----|--|----|
| 1. | Introduction..... | 91 |
| 2. | Conduction properties..... | 92 |
| 2.1 | Comparison with theory | 93 |
| 3. | Determination of the oxygen non-stoichiometry..... | 97 |

| | | |
|-------|--|-----|
| 3.1 | Under standard conditions / atmosphere | 97 |
| 3.1.1 | Effect of temperature | 97 |
| 3.2 | Effect of reducing atmosphere | 100 |
| 3.2.1 | XRD study | 100 |
| 3.2.2 | TGA study | 100 |
| 3.2.3 | TPR study | 101 |
| 3.2.4 | Interpretation | 102 |
| 4. | Ionic conductivity | 106 |
| 4.1 | Ionic conductivity obtained by isotopic exchange | 106 |
| 4.2 | Comparison between ionic conductivity calculated from different techniques at different PO_2 | 106 |
| 5. | Conclusion | 110 |

CHAPTER 6: CTF STABILITY

| | | |
|-----|---|-----|
| 1. | Introduction | 114 |
| 2. | Aging and stability under non-reactive atmosphere | 115 |
| 3. | Aging under reactive gases | 118 |
| 3.1 | Under CO/CO_2 | 118 |
| 3.2 | Experiment under wet CO_2 | 123 |
| 3.3 | Hydrothermal treatment | 126 |
| 3.4 | Effect of H_2 | 128 |
| 3.5 | Oxidation of methane | 128 |
| 4. | Redox stability potential | 134 |
| 4.1 | Basic principle | 134 |
| 4.2 | Electrochemical reduction (Pt electrode) | 135 |
| 4.3 | Chemical reduction by hydrogen (Pt electrode) | 135 |
| 4.4 | Chemical and electrochemical reduction using iron electrode | 136 |
| 4.5 | First synthesis of the results | 137 |
| 5. | Conclusion | 138 |

CONCLUSION AND PERSPECTIVES 141

ANNEXE 1: CTF 20 143

CHAPTER 1

LITERATURE

REVIEW

Selon la belle formule de Pessoa, la vie ne suffit pas et [...] la littérature est là pour nous élever un peu au-dessus de nous-mêmes.
Jean d'Ormesson (Odeur du temps, 2007)

Table of content

| | |
|--|----|
| 1. Context | 14 |
| 2. OTMs | 17 |
| 2.1 Fundamentals | 17 |
| 2.1.1 Oxygen transport limited by oxygen bulk diffusion | 18 |
| 2.1.2 Oxygen transport limited by surface exchange reactions | 19 |
| 2.1.3 Mixed-limited regime | 19 |
| 2.1.4 OTM requirements | 20 |
| 2.2 State of the art..... | 21 |
| 3. Perovskites..... | 23 |
| 3.1 Electrical properties of perovskites | 23 |
| 3.1.1 Oxygen-ion conductivity | 23 |
| 3.1.2 Electronic conductivity | 24 |
| 3.1.3 Oxygen semi-permeability..... | 25 |
| 3.2 Stability..... | 25 |
| 3.3 CTF | 27 |

1. Context

In November 2016, the Paris agreement to combat climate change came into effect [1]. In the agreement, 169 countries pledged to limit the average global warming temperature to well below 2 °C, and reach the global emission peak as quickly as possible.

Anthropogenic CO₂ emissions keep increasing worldwide since the 1950's (Figure 1). The evolution of the amount of these emissions will impact the global warming and different trends exist in the literature. In 2014, the Intergovernmental Panel on Climate Change (IPCC) published a report [2] which took into consideration the wide range emission scenarios. The so-called RCP8.5 and RCP6.0 correspond to scenarios where no additional efforts are done to constrain CO₂ emissions, RCP4.5 is an intermediate scenario and RCP2.6 corresponds to the goals of the Paris agreement.

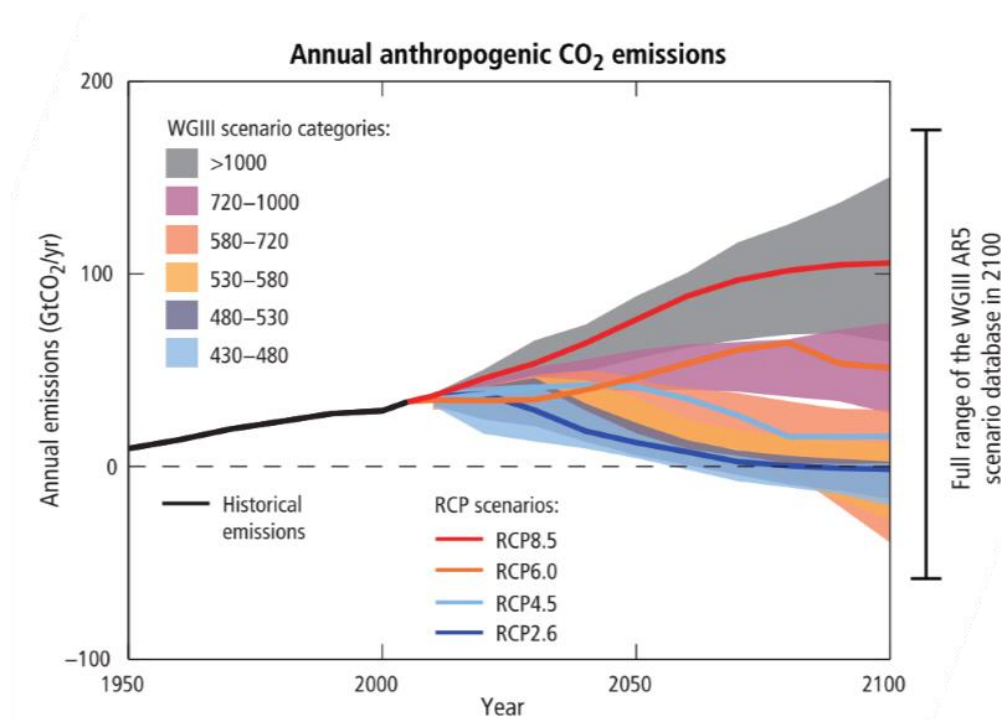


Figure 1: Emissions of carbon dioxide (CO₂) alone in the Representative Concentration Pathways (RCPs) which represent different scenarios [3]. The WGIII scenario categories represent the errors margin of the 4 RCP scenarios.

To comply with the Paris agreement, the annual emission of CO₂ has to decrease drastically to follow the RCP2.6 scenario.

It has been determined that coal-fired power plants caused one third of total global emissions [4]. To mitigate these emissions, different strategies are being studied, including replacing carbon by renewable energy sources, or natural gas (a less pollutant source). However, even these are not necessarily carbon-neutral alternatives when the full energy production lifecycle is considered. Regardless, the IPCC estimates that the replacement strategy alone may be insufficient to curb enough carbon emissions, while requiring unrealistically large economic investments.

Instead, the panel recommends combining such strategies with carbon capture and storage (CCS) technologies, which are equally efficient in reducing CO₂ emissions. CCS technologies can limit up to 90% of the CO₂ emitted in a standard plant, and are comparably cheaper by 72% [2] because they can be retrofitted into existing production lines.

There are 3 main industrial processes to capture CO₂ (Figure 2), after which CO₂ is compressed, transported and finally stored.

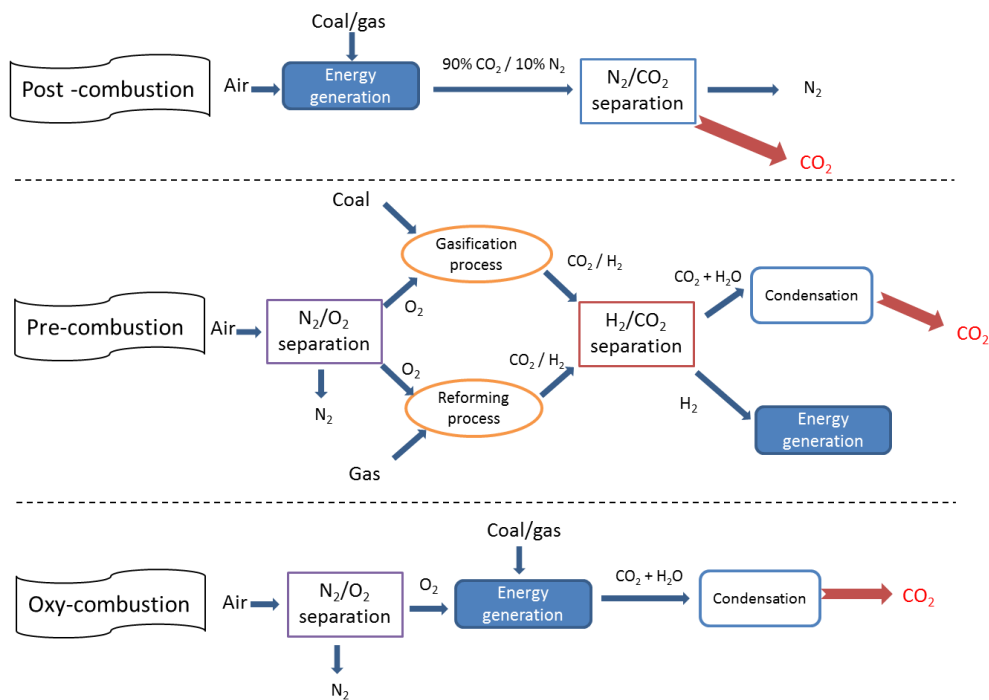


Figure 2: Diagrams of post-, pre-, and oxy-combustion carbon capture processes [5,6]. The separation steps are highlighted in these diagrams.

Post-combustion process captures CO₂ after the combustion of air with coal or gas. The fuel is burned with excess air, producing a flue gas mostly consisting of N₂ (75-80%), and CO₂ (15-20%) at atmospheric pressure. CO₂ is then separated from N₂. For CO₂ recovery, the flue gas goes through a column filled with a solvent (usually an aqueous liquid amine solution). The CO₂-saturated amine solution is then heated to release the captured CO₂. The amines themselves can be recycled and re-used but the chemical regeneration still needs to be improved.

Post-combustion capture is the most mature CCS technology but the low CO₂ purity of the captured gas affects the efficiency [7,8].

Pre-combustion process captures CO₂ before the combustion (or use) of H₂. The pre-combustion process can be applied to natural gas or coal-based plants. Fuel is converted to syngas (CO₂ /CO and H₂) by reforming or gasification. Carbon monoxide reacts with steam in a water gas shift (WGS) reactor to produce a mixture of CO₂ and H₂. CO₂ is then separated from H₂ which can be use as fuel in gas turbine combined cycle.

Pre-combustion capture is used in industrial processes because it can retrofit to existing plants [9], however, it is still expensive, mainly due to the cost of shift conversion and air separation unit.

Oxy-combustion process captures CO₂ after the combustion of fuel with excess O₂ previously separated from air. To control the flame temperature, recycled gas can be added to the oxygen. After combustion, there are mainly CO₂ and water vapor which is then condensed before capturing CO₂. A step of purification of CO₂ could also be needed [7,8].

Oxy-combustion capture can produce high CO₂ purity (higher than 98%) however, the air separation unit (when cryogenic O₂ is used) represents a huge part of the total cost.

Unfortunately, CSS implementation decreases the energy efficiency of the plant and raises the production and maintenance costs. Assuming 90% CO₂ capture rate, the overall efficiency of a power plant would drop by about 30–35% [10]. Different studies [7,11] summed up different power plant efficiencies with and without the different types of CCS (Table 1). The three CCS technologies lead to a higher electricity costs (slightly higher for oxy-combustion). However, the cost of CO₂ avoided has to be taken into account, and is strongly dependent on the implemented policies.

Table 1: Cost comparison for different CCS process, assuming CO₂ compression to 110 bar, and excluding storage and transportation costs [7,12].

| Fuel type | Parameter | Different technologies | | | |
|-----------|---------------------------------|------------------------|-----------------|----------------|----------------|
| | | Without CCS | Post-combustion | Pre-combustion | Oxy-combustion |
| Coal | <i>Electricity cost (c/kWh)</i> | 5.4 | 7.5 | 6.9 | 7.8 |
| Gas | <i>Electricity cost (c/kWh)</i> | 6.2 | 8.0 | 9.7 | 10.0 |

To make CCS more attractive, it is then very important to increase the efficiency of the CCS technologies. There are basically two ways: by improving the performance and decreasing cost of CCS process, or by heat recovering [13].

One financial hard point of the process is the air separation unit (ASU). When using cryogenic air separation, an optimum O₂ purity has to be found because the higher the O₂ purity, the more energy purification consumes, but then less energy for CO₂ compression is needed. Studies defined that 95% O₂ purity is the best compromise [13]. Cryogenic air separation is a method which is already mature (world's first patent in 1902) but it decreases efficiency of a power plant by around 8–10% [14].

Studies on the ASU were performed and alternatives to cryogenic air separation were investigated [15]. Pressure swing adsorption (PSA) which is an adsorption/desorption method is less expensive than cryogenic distillation but produces low purity oxygen. Another alternative is to use ceramic oxygen transport membranes (OTM). OTM could replace cryogenic ASU especially in power plant using CCS. It enables to obtain very high purity oxygen (>99 %) and particularly the effective energy demand for oxygen production can be further reduced (-40 %) [10]. Using OTM instead of cryogenic air separation enables to reduce the drop on net efficiency of an oxy-combustion plant from 8-11% to 2-5% [5]. Moreover, it will consume 50% less water than cryogenic ASU and require 50% less area. But the question of long term stability is critical.

2. OTMs

2.1 Fundamentals

Oxygen transport membranes (OTM) are dense ceramic devices that are able to selectively transport high-purity oxygen through a mechanism of oxygen vacancy diffusion (Figure 3). In the simplest design, the ceramic membrane separates two atmospheres with different oxygen partial pressures, creating a chemical potential gradient that drives the oxygen flux towards the low oxygen partial pressure (P_{O_2}) side.

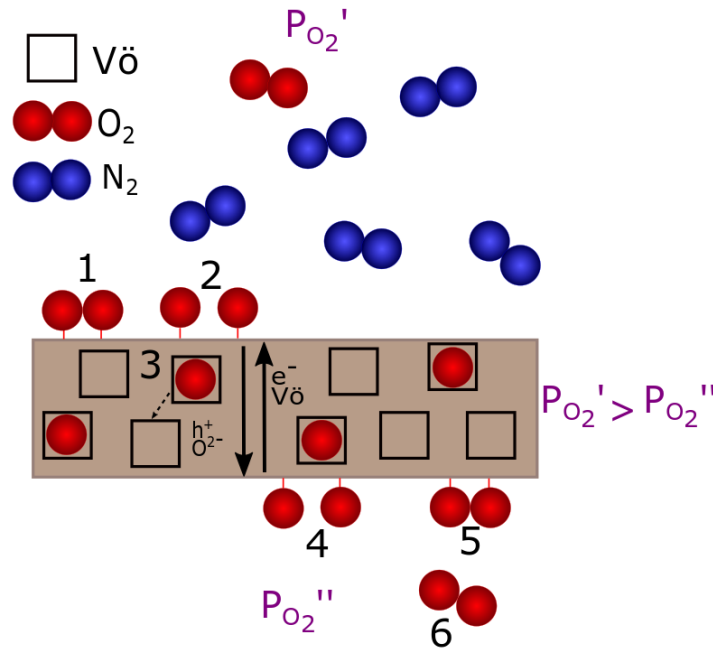


Figure 3: Schematic representation of a mixed ionic-electronic OTM.

Oxygen is transported in the form of O^{2-} ions, and there must be an electron flux in the opposite direction to maintain charge neutrality. Consequently, mixed ionic and electronic conductors (MIEC) are materials of choice because both the ionic and electronic fluxes can occur within the membrane and do not require any electrodes.

Oxygen transport can be schematically considered a three-step process (Figure 3) [16]: (1) adsorption of oxygen through a surface exchange on the oxygen-rich (oxidizing) side; (3) bulk diffusion of oxygen ions inside the membrane; (6) desorption through a second surface exchange into the oxygen-lean (reducing) side. Moreover, a step of oxygen reduction occurs (2) at the surface of the oxygen-rich side (also named feed side) (Equation 1). Similarly, on the other side of the membrane, i.e. the oxygen-lean side, the oxygen ions recombine into molecular oxygen (5), which can be recovered or used as a reagent.



The rate-limiting step may be the result of either bulk diffusion or surface exchange reactions, or both (mixed limitation). An efficient strategy to improve the performance of the membrane will focus on the rate-limiting step, which is already a challenge in itself. Setup to determine experimentally this limiting step will be presented in Chapter 2. According to the limiting step, different theories can be applied.

2.1.1 Oxygen transport limited by oxygen bulk diffusion

When bulk diffusion is the limiting factor, Wagner's theory describes the oxygen flux, j_{O_2} , with Equation 2.

$$j_{O_2} = \frac{1}{4^2 F^2 L} \int_{\mu_{O_2}^{lean}}^{\mu_{O_2}^{rich}} \sigma_{amb} d\mu_{O_2} \quad \text{Equation 2}$$

j_{O_2} : Oxygen flux (mol.cm⁻².s⁻¹)

$\sigma_{amb} = \frac{\sigma_i \sigma_e}{\sigma_i + \sigma_e}$: Ambipolar conductivity (S.cm⁻¹)

σ_i : Ionic conductivity (S.cm⁻¹)

σ_e : Electronic conductivity (S.cm⁻¹)

F : Faraday constant (96 485 C.mol⁻¹)

L : Thickness of the membrane (cm)

$\mu_{O_2}^{lean}$ and $\mu_{O_2}^{rich}$: Chemical potential of oxygen on the lean side and on the rich side of the membrane, respectively (J.mol⁻¹).

With respect to the oxygen transport, the ionic conductivity corresponds to the oxygen vacancy conductivity $\sigma_{V_{O}^{\bullet\bullet}}$, and the electronic conductivity is the sum of both electrons and electron holes contributions. Assuming an ideal thermodynamic system, the chemical potential of oxygen is $d\mu_{O_2} = RT d\ln(P_{O_2})$.

Equation 2 can be simplified when the MIEC oxide exhibits a majority carrier, either ionic or electronic defects.

For most perovskite-based mixed ionic–electronic conductors, $\sigma_e \gg \sigma_i$ then $\sigma_{amb} \approx \sigma_i$. It follows that:

$$j_{O_2} = \frac{RT}{4^2 F^2 L} \int_{P_{O_2}^{lean}}^{P_{O_2}^{rich}} \sigma_i d\ln(P_{O_2}) \quad \text{Equation 3}$$

Ionic conductivity is generally constant over a large range of P_{O_2} ; thus, Equation 3 becomes:

$$j_{O_2} = \frac{RT \sigma_i}{4^2 F^2 L} \ln \left(\frac{P_{O_2}^{rich}}{P_{O_2}^{lean}} \right) \quad \text{Equation 4}$$

For $\sigma_i \gg \sigma_e$, $\sigma_{amb} \approx \sigma_e$:

$$j_{O_2} = \frac{RT}{4^2 F^2 L} \times \int_{P_{O_2}^{lean}}^{P_{O_2}^{rich}} \sigma_e d\ln(P_{O_2}) \quad \text{Equation 5}$$

If the additional electronic conductivity is p-type, then the equilibrium of the oxide with oxygen can be written:



Using the law of mass action, we obtain an electron hole concentration that is proportional to $P_{O_2}^{1/4}$, and the electronic conductivity is expressed as: $\sigma_h^0 \times P_{O_2}^{1/4}$. Therefore,

$$j_{O_2} = \frac{RT\sigma_h^0}{4F^2L} (P_{O_2}^{rich}{}^{1/4} - P_{O_2}^{lean}{}^{1/4}) \quad \text{Equation 7}$$

Equation 4 and Equation 7 are useful to describe the performances of an OTM membrane when limited by bulk diffusion. It is then possible to link the oxygen flux to the conductivities and to forecast performances under different P_{O_2} .

2.1.2 Oxygen transport limited by surface exchange reactions

The Wagner equation fails to accurately describe oxygen flux performance when the surface exchange reactions are rate-limiting. Different equations are proposed in the literature [17] to characterize the surface exchange reactions (Equation 8 to Equation 12 are examples of surface exchange processes with s representing an adsorption site and (ad) meaning for adsorbed):



Equation 8 corresponds to the associative adsorption of oxygen on the surface which occurs usually at low temperature. Equation 9 corresponds to the dissociative adsorption of oxygen on the surface which occurs usually at high temperature. Equation 10 and Equation 11 represent the reduction of the adsorbed oxygen (in the case of the dissociative adsorption) before the oxygen ion incorporation into the lattice (Equation 12) [18].

A simple relationship between the oxygen flux and the oxygen partial pressure on both sides of the membrane was used and verified for permeation measurements of dense $Bi_2V_{0.9}Cu_{0.1}O_{5.35}$ without a catalytic layer deposited onto the membrane surfaces [19].

$$j = \alpha \left[(P_{O_2}^{rich})^{1/2} - (P_{O_2}^{lean})^{1/2} \right] \quad \text{Equation 13}$$

Again, if this relation is verified, for a membrane limited by surface exchange reaction, it is possible to forecast performances under different P_{O_2} .

2.1.3 Mixed-limited regime

It has been demonstrated forty years ago [20–22] that the oxygen permeation flux through a zirconia membrane induces a deviation from equilibrium on both sides of the electrolyte. Consequently, Wagner's theory cannot be applied in this case, because it assumes that both oxide surfaces are in equilibrium with the gas phase. Since these findings were published, it has been observed that, for most OTM materials, the oxygen permeation flux is controlled simultaneously by diffusion and by surface exchanges.

With a mixed regime, it is difficult to obtain an explicit relationship between the oxygen flux, the rate constants of the steps involved in the permeation process, and the actual partial pressures on both sides of the membrane. Various approaches have been developed and are explained in a published paper [23].

Experimentally, solutions exist to determine the limitations of the oxygen transport.

Surface reaction is characterized by the surface exchange coefficient, k_s . The oxygen diffusion coefficient, D^* , characterizes the bulk diffusion. A characteristic thickness, L_c , has been defined which indicates the membrane thickness at which the oxygen flux is equally limited by the bulk diffusion and the surface exchange kinetics (Equation 14).

$$L_c = \frac{D^*}{k_s} \quad \text{Equation 14}$$

For a membrane thickness $L \gg L_c$, at a given temperature, permeation of oxygen will be limited by bulk diffusion. If $L \ll L_c$, it will be limited by surface exchange kinetics. Experimentally, it is difficult to determine this thickness and several semi-permeation experiments are needed. Isotopic exchange or relaxation techniques can be used to determine these parameters.

This thesis is based on the experimental approach proposed by Kleitz et al. [20], showing that oxygen partial pressure $P_{O_2}^{rich}$ and $P_{O_2}^{lean}$ can be replaced by the actual oxygen activity on the rich and lean surfaces, respectively. As detailed in chapter 2, two electrochemical surface probes can be used to measure the oxygen activity *in situ* [19,20,24,25] and consequently identify rapidly the rate limiting step.

2.1.4 OTM requirements

The flux performances have been widely studied and they depend mainly on the electrical properties of the material and the geometry of the membrane. The performance of the material can then be optimized by tailoring electrical properties of the material, commonly via chemical doping.

However, performance is not the only key parameter for the OTM. Indeed, OTMs should be chemically stable when exposed to different atmosphere compositions, which include (CO/CO₂, CH₄, H₂/H₂O), at high temperatures (> 800 °C) over 10000 h [26–28]. Figure 4 sums up the different requirements needed for an OTM.

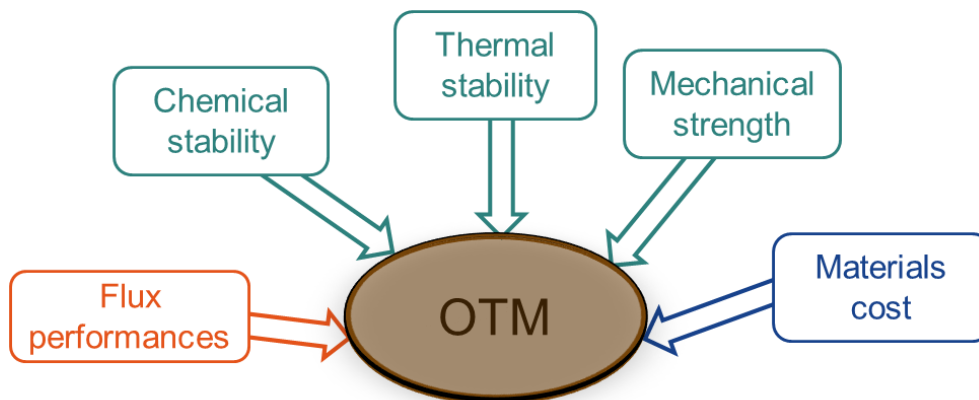


Figure 4: Requirements for an OTM [29].

In this PhD thesis, I will mainly focus both on the performances and chemical and thermal stability. It is important to note that performance improvements often come at the expense of stability, and vice versa. A balance needs to be found between all these requirements. Yet, it is important to assess the stability under reactive atmospheres to meet the demand of certain applications.

2.2 State of the art

Owing to their potential interest, OTMs are the subject of investigation and development both in academic and industrial research centers [15,30–33]. In October 2007, the “MEM-Brain” project started and is a part of the Alliance Programme of the German Helmholtz Association regrouping twelve European research institutions and five industrial partners. The project has a time horizon for significant commercialization after 2020 [30] and focuses on the development and integration of ceramic and polymeric gas separation membranes for zero-emission fossil power plants.

In oxy-combustion, to be economically viable, heat recovering has to be implemented. The heat needed for the OTM can be brought using a part of the recycled CO_2 from the combustion process. Moreover, this would increase the oxygen partial pressure drop across the membrane. However, this concept cannot be deployed in the near future because there is no stable ceramic membrane resistant to CO_2 and SO_2 (present as impurity in the plant) and that is why European programs such as MEM-Brain or Green-CC, finance several studies on stable new ceramics [30,34,35].

Praxair and Air Product invest on research on OTM. Praxair works on an Advanced Power Cycle (APC) to incorporate OTM into coal-fired plant [15]. It consists on the integration of OTM in the boiler and also on the use of OTM for a post gasification partial oxidation (P_{Ox} , conversion of methane in CO and H_2) (Figure 5). Usually, the efficiency of these plants with CCS is around 32%. With this kind of process integration an efficiency of 37% is expected [32]. It has recently been tested in an experimental coal gasifier [15].

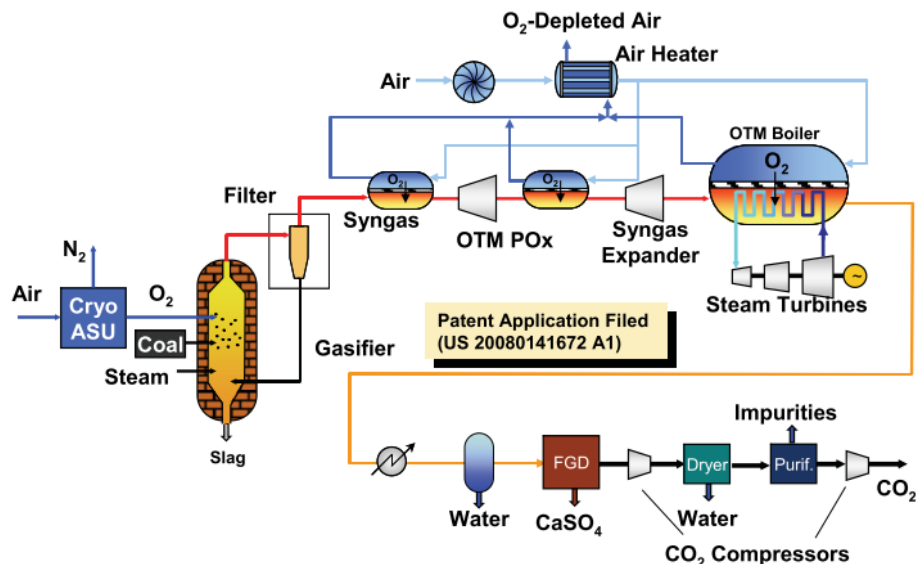


Figure 5: Process for integration of OTM into power generation cycle with CO_2 capture from Praxair [32].

Air Product also works on membrane development for oxygen production for several years and they have operated a test unit which can produce up to 100 tons per day of oxygen using OTM [33]. Several studies on the use of membranes in integrated gasification combined cycle (IGCC) power plant are published in the literature [36,37]. One of the advantages is that they can be easily integrated and are easier to operate and

maintain because the membrane modules involve no moving parts [37]. It is important to note that, unlike in oxy-combustion plant operated where membranes have to be CO₂ tolerant; membranes should be resistant to steam. CCS can be implemented to these plant [38]. They expect up to 1.8% points efficiency advantage compared to a process without OTM [33,38,39].

OTM can also combine both the air separation and the auto thermal reforming (ATR) (during reforming process in pre-combustion capture described in Figure 2) [40,41]. The membrane is then used as a catalytic membrane reactor (CMR) where both separation and catalytic process occur. Air Product [42] reported that it could be 30% less expensive than the cryogenic air separation unit with an ATR.

The use of OTM as CMR brings several advantages [26,27]. First it avoids the costly separation of oxygen from air (which is usually done with cryogenic units). Then, it could increase the overall chemical reaction performance (i.e. either the rate of the reaction or the selectivity or the yield) because of the removal of some products through the membrane or the gradual introduction of reactant (oxygen)... Three main reactions have been widely studied: the partial oxidation of methane (POM) into syngas (Figure 6), the oxidation reforming of methane, and the oxidative coupling of methane (OCM) [26,43].

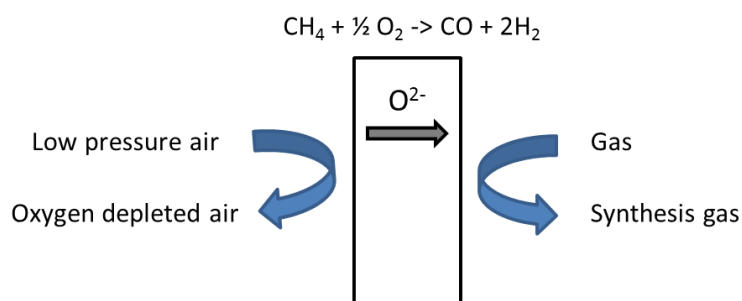


Figure 6: Schema for OTM syngas (POM).

It was estimated that the use of OTM in methane conversion could be beneficial in term of productivity (+ 21% in hydrogen yield) and from an environmental point of view (- 50% NO_x emissions and - 20% CO₂ emissions) [28,44]. However, the membrane should resist to the reductive atmosphere of methane and the extreme oxygen gradient created by the oxygen containing atmosphere.

The material used as OTM has then to bring the highest oxygen semi-permeation flux, but also to be resistant to pollutants present on the plants and/or to reactive gases which are used for some application. The challenge is then to find the best material and the best geometry of the membrane.

Several reviews studied the best material for OTM [45–47] which should answer to numerous requirements; it should be a highly conducting mixed conductor to provide a high oxygen semi-permeation rate, be chemically stable under reactive atmospheres and a wide range of temperature, be inexpensive, and have high mechanical strength and good creep resistance. Most of the studies focus on the performances of the OTM. Consequently, a wide range of materials have been screened and especially materials with a perovskites crystal structure, due to their known high ionic and electronic conductivities [16,45,46,48,49].

3. Perovskites

Perovskite is the name of both the mineral CaTiO_3 and of the crystalline structure family ABO_3 . Ideal perovskite crystallizes in cubic symmetry, with the B cations at the corners, the A atom in the center and the oxygen in the center of the cube edges (Figure 7). This induces the creation of the BO_6 octahedron while the A site has 12-fold coordination. Cations of various valences can compose the perovskite structure, the valence of the A atom varying from 3 to 1 and the one of the B atom varying from 3 to 5.

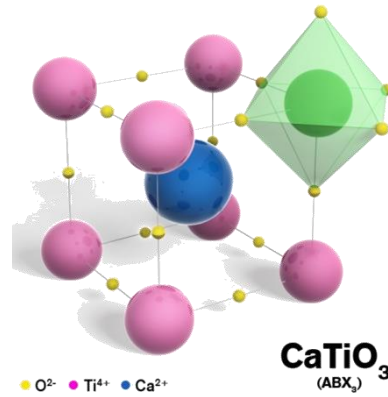


Figure 7: Structure type of CaTiO_3 [50].

Perovskites can accommodate different cation sizes in their lattice. The chemical stability of the perovskite structure is often described by the Goldschmidt tolerance factor, t (Equation 15) with R_A , R_B , and R_O , the ionic radii of the cations on the A site, cations on the B site, and oxygen respectively. It is considered that a structure is stable within $0.8 < t < 1$ range. A cubic arrangement is obtained for $0.97 < t < 1.03$ [49]. However, the majority of perovskite structures are distorted and do not have cubic symmetry at room temperature (especially the $\text{A}^{\text{III}}\text{B}^{\text{IV}}\text{O}_3$ [45,46]) but tend to the cubic structure when temperature increases.

$$t = \frac{R_A + R_O}{\sqrt{2} (R_B + R_O)} \quad \text{Equation 15}$$

The valence of the cations should be lower than five and their size in the range of 0.45–0.75 or 1–1.4 a.u. (atomic unit) [16,51]. This makes perovskites relatively easy to dope. From an electrical point of view, dopants can introduce electronic or ionic defects to control electrical conductivity.

The concentration of defects depends on the temperature and atmospheric partial pressure of their components (usually oxygen in oxides), and therefore the electrical behavior too.

3.1 Electrical properties of perovskites

3.1.1 Oxygen-ion conductivity

Oxygen diffuses via a hopping mechanism through the oxygen vacancies [26,52,53]. Oxygen vacancies are especially present in the material from doping. Indeed, doping a perovskite $\text{A}^{\text{II}}\text{B}^{\text{IV}}\text{O}_3$ with a D atom (with a valence of 3) generates oxygen vacancies via a local electrostatic compensation mechanism (cf. Equation 16 with the Kröger-Vink notation).



The result is a material with the composition, $AB_{1-x}D_xO_{3-\delta}$, where δ expresses oxygen non-stoichiometry. In this case, if all the D atoms have a valence of 3 and are in the B sites, then $\delta = x/2$ because, according to Equation 16, two D atoms create one oxygen vacancy.

Several parameters influence the ionic conductivity which is, in this case, ensured by the ionic diffusion of the O^{2-} through the material.

The concentration and availability of oxygen vacancies is a key parameter of the oxygen diffusion. An optimal value of oxygen non stoichiometry, δ , is 0.2 [46,49,54]. When too many oxygen vacancies are present in the material, their mobility decreases due to ordering. That means that the vacancies are less available for the oxygen diffusion because it is less energetically favorable.

On the other hand, the crystal lattice should be the most symmetrical, i.e. a cubic symmetry, to provide stress-free lattice [45,46,55]. The hopping mechanism through the vacancies along the octahedral edge is easier in the cubic structure [55,56].

Consequently, there is a balance to find, between the amount of dopant (i.e. the amount of oxygen vacancies) and the symmetry of the crystal lattice which will be more distorted when adding dopants. A good compromise was found with a $t \approx 0.96$ and $\delta < 0.2$ [46,49,54].

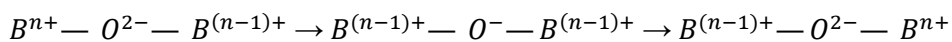
3.1.2 Electronic conductivity

The electronic conductivity is ensured by the displacement of electrons or electron holes within the material. For perovskites, it occurs along the B-O-B chains because the valence of the B-site cations can change [45,46]. Doping the B site of the perovskite can change the properties of the B-O-B chain and affect the electronic conductivity. Indeed, defects created during doping (Equation 17) can be further oxidized or reduced (Equation 18 and Equation 19).



There are different mechanisms for the electronic conductivity. The large polaron mechanism, the small polaron mechanism and the free electron band type conduction.

When an electron (or electron hole) move through ionic oxides, the lattice around it is polarized and it causes a local deformation of the structure. The electron (or electron hole) with the local deformation is termed a polaron [57]. When the interaction with lattice is weak, the polaron is considered as a large polaron. The large polarons move in bands and their mobility is proportional to $T^{-1/2}$. In the case of the perovskite, usually electronic conductivity is p-type and follow the small polaron mechanism [58]. Hopping can occur between two neighboring B cations in the perovskite lattice, with the mediation of the 2p orbital of the oxygen:



There are few examples of free electron band type conduction because there is a very small overlap between the d orbitals of transition metals in the cubic symmetry [58]. However, the electronic conductivity of $\text{La}_{1-x}\text{Sr}_x\text{MnO}_{3-\delta}$ has been investigated and for $x < 0.2$, the hopping mechanism was evidenced whereas for $x > 0.3$, the semi-metallic behavior was observed, meaning that the electronic conductivity decreases with temperature increase.

3.1.3 Oxygen semi-permeability

The oxygen semi-permeability was tested on several materials [16] (Figure 8).

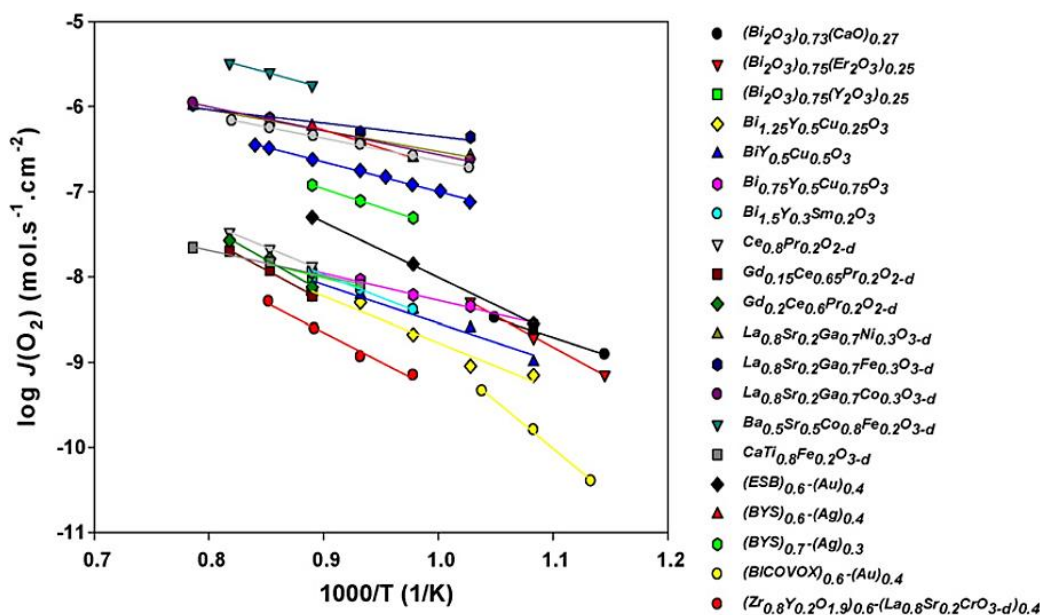


Figure 8: Temperature dependence of oxygen flux [16].

The highest oxygen flux is obtained for $\text{Ba}_{1-x}\text{Sr}_x\text{Co}_{1-y}\text{Fe}_y\text{O}_{3-\delta}$ (BSCF). For instance, a 1.8 mm thick $\text{Ba}_{0.5}\text{Sr}_{0.5}\text{Co}_{0.8}\text{Fe}_{0.2}\text{O}_{3-\delta}$ membrane exhibits a specific oxygen permeability of $0.38 \text{ mL}\cdot\text{min}^{-1}\cdot\text{cm}^{-1}$ at 900°C [16]. Regardless, it is below the $0.9\text{-}1.8 \text{ mL}\cdot\text{min}^{-1}\cdot\text{cm}^{-1}$ target for economic viability [46].

3.2 Stability

The academic research is very focused on oxygen flux performance characterization and optimization. Comparatively, few studies concern the stability of OTMs, particularly in the long term ($> 500 \text{ h}$). A review [46] summed up some generalities about stability of materials with a perovskites crystal structure. The chemical stability of an ABO_3 perovskite structure depends on the redox character of the cations on the B-site and the ionic-covalent character of the A-O bond.

The resistance to gases is also linked to the chemical composition. Indeed, under CO_2 , carbonates are likely to be formed, especially for large alkaline-earth cations or when the Gibbs enthalpy of formation of the corresponding carbonates is low. Consequently, the A atom can be sorted from the more to the less stable: $\text{La} > \text{Ca} > \text{Sr} > \text{Ba}$. The B atoms also influence the CO_2 tolerance. OTMs with titanium are more resistant than with gallium, chromium, manganese, iron and cobalt [46].

Other gases such as CO , H_2S , and H_2O can also react with the membrane. CO can have a similar effect as CO_2 , whereas steam may have an impact on the microstructure of the membrane. Besides, the presence of sulfur may induce surface degradations [59]. Patents report that the oxygen semi-permeation flux of Mg, Ca,

Sr, Ba-based perovskites decrease roughly by 30-50% during 100 h, when the gas used on the feed side (usually air) contains a few percent of H₂O and ppm level of CO₂ (Figure 9) [16,60–62].

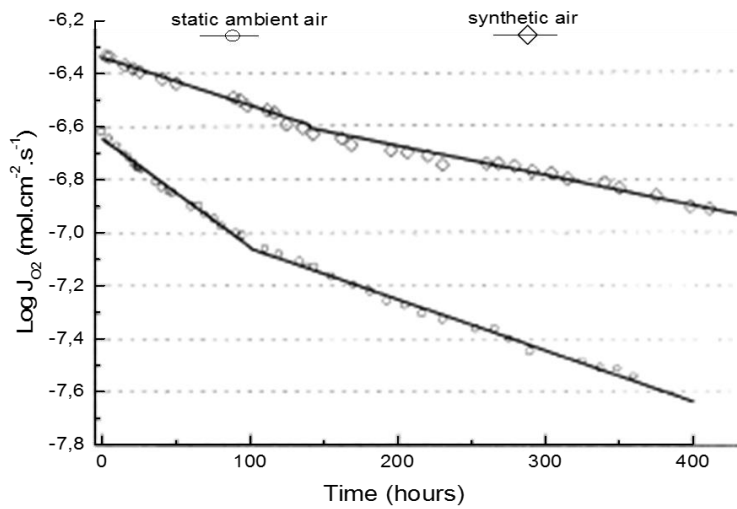


Figure 9: Influence of the presence of CO₂ and water vapor in the ambient air (vs. clean synthetic air) on the semi-permeation flux of BSCF at 750 °C as a function of time [62].

The applicability of BSCF is limited in practice by severe chemical and mechanical degradations. For instance, in CO₂/H₂O atmospheres, formation of carbonates and/or hydroxides on the surface were reported, decreasing the flux performance by at least two orders of magnitude almost immediately (Figure 10) [63]. It was also reported that, when pure CO₂ is sent as sweep gas, it immediately stops the oxygen semi-permeation flux, but this can be recovered by sweeping helium (Figure 11) [64]. The perovskite structure shows signs of decomposition over a depth of 40–50 μm.

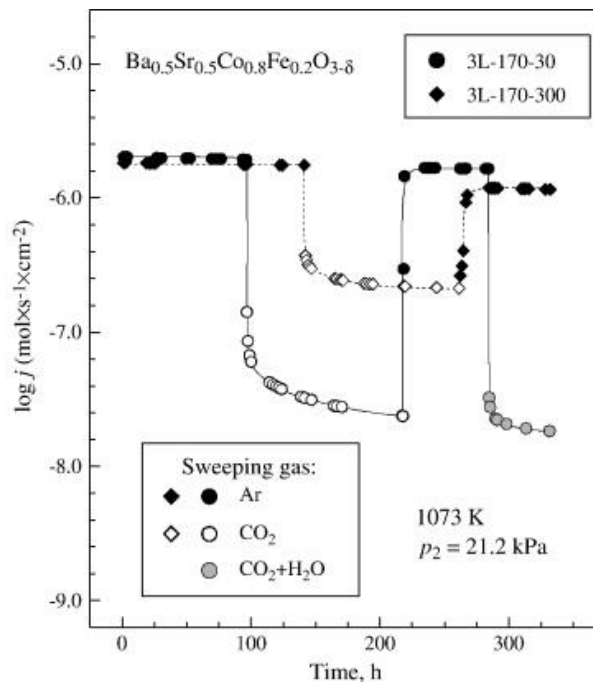


Figure 10: Time dependence of oxygen permeation fluxes through three-layer BSCF membranes exposed to CO₂ and H₂O containing atmospheres [63].

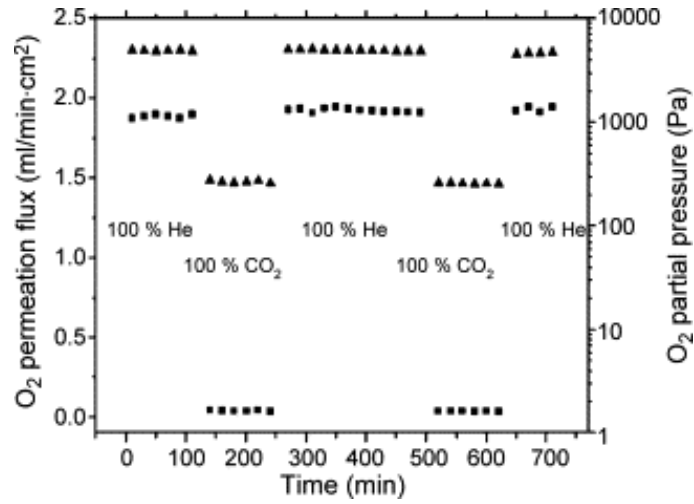


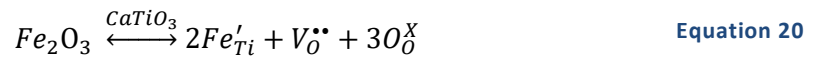
Figure 11: Oxygen permeation flux (■) under pure helium and CO₂ of a Ba_{0.5}Sr_{0.5}Co_{0.8}Fe_{0.2}O_{3-δ} membrane. (▲) represent the oxygen partial pressure [64].

Steam also affects the BSFC performance, especially because of carbonic acid in distilled water used to generate steam. It was reported that the oxygen semi-permeation flux decreases by half after 90 h under steam exposure [65]. However, the loss was essentially attributed to the formation of carbonates due to the presence of the acid which formed a porous structure inside the hollow fiber membrane in this example. Nevertheless, the structure of the BSFC was also changed, reducing the crystal size [65].

It is then very difficult to use BSCF as is for OTM applications. As high performances often involve poor stability, the choice of a perovskite material with lower flux performances can represent a good compromise for OTM applicability.

3.3 CTF

CaTi_{1-x}Fe_xO_{3-δ} (CTF) is the perovskite studied in this thesis. CTF is a mixed ionic and electronic perovskite material where iron substitutes titanium in the lattice according to Equation 20.



The Goldschmidt tolerance factor on the CTF doped with 10% iron, referred to as CTF10, is equal to 0.97. The presence of Ti⁴⁺ and Fe³⁺ cations with different valences cause an excess negative charge in the lattice which is compensated by oxygen loss, thus creating the vacancies responsible for oxygen transport.

For two iron added, one V_O^{••} is created (Equation 20) thus oxygen vacancy concentration increases with iron concentration. However, the binary system CaTiO₃-CaFeO_{2.5} was analyzed [66–68] and evidenced the presence of ordered phases at high iron concentration (Figure 12). These ordered phases limit oxygen diffusion, consequently there is an optimum iron doping to obtain the highest oxygen diffusion.

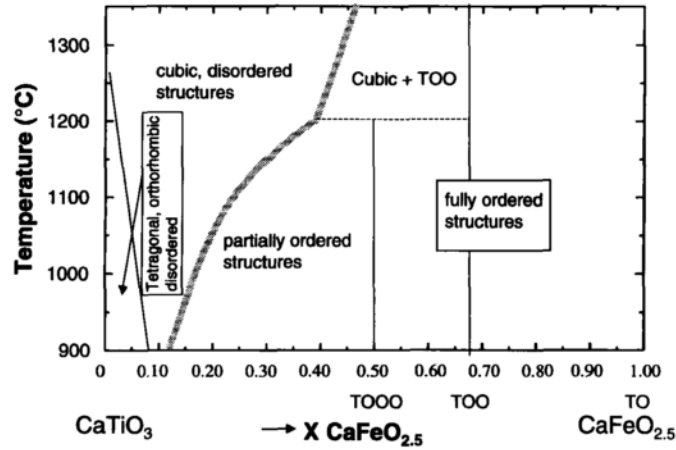


Figure 12: Phase diagram for the system $\text{CaTiO}_3\text{-CaFeO}_{2.5}$ as a function of temperature and composition. TO, TOO, and TOO indicate the sequence of tetrahedral (T) and octahedral (O) layers in the ordered structure [68].

According to the phase diagram (Figure 12) and to conductivity measurements [69,70], the optimal amount of iron is around 10 to 20%, compositions already tested as OTM [71–76].

CTF has a reported specific oxygen permeability of $3.0 \times 10^{-3} \text{ mL} \cdot \text{min}^{-1} \cdot \text{cm}^{-1}$ at 900°C [75], which is considerably lower than the best flux measured in state-of-the-art membrane materials such as lanthanum or barium-iron cobaltites [53,72,77].

Table 2: Oxygen permeation flux of CTF membranes ($P_{O_2, \text{feed side}} = 0.21 \text{ bar}$ for all the values).

| Material | Temperature ($^\circ\text{C}$) | Thickness (mm) | J_{O_2} ($\text{ml} \cdot \text{cm}^{-2} \cdot \text{min}^{-1}$) | Ref. |
|---|----------------------------------|----------------|--|------|
| $\text{CaTi}_{0.8}\text{Fe}_{0.2}\text{O}_{3-\delta}$ | 950 | 1.7 | 0.05 | [73] |
| $\text{CaTi}_{0.85}\text{Fe}_{0.15}\text{O}_{3-\delta}$ | 900 | 1 | 0.0005 | [72] |
| $\text{CaTi}_{0.85}\text{Fe}_{0.15}\text{O}_{3-\delta}$ | 1000 | 0.91 | 0.05 | [75] |
| $\text{CaTi}_{0.75}\text{Fe}_{0.15}\text{Mg}_{0.05}\text{O}_{3-\delta}$ | 1000 | 1.36 | 0.055 | [75] |
| $\text{CaTi}_{0.75}\text{Fe}_{0.15}\text{Mn}_{0.1}\text{O}_{3-\delta}$ | 1000 | 1.0 | 0.07 | [75] |
| $\text{CaTi}_{0.73}\text{Fe}_{0.18}\text{Mg}_{0.09}\text{O}_{3-\delta}$ | 1000 | 0.9 | 0.25 | [76] |

Table 2 sums up the results of oxygen semi-permeation flux of CTF materials found in the literature. However, it is difficult to compare them because the total amount of dopant varies and this influences the number and availability of oxygen vacancy. Moreover, according to the different thicknesses and surface states of the membranes, the measured oxygen flux can be either limited by bulk diffusion, surface exchange or both, so the comparison is again very difficult. However, in several articles, the flux is around $0.05 \text{ ml} \cdot \text{cm}^{-2} \cdot \text{min}^{-1}$. A study [76] found a much higher flux, but this value is questionable because when literature values are reported they are largely overestimated. We assume that an error occurred during the unit conversion. Results from another study [72] are rather low but the oxygen partial pressures gradient across the membrane is very low which can explain this behavior. In this work, I will focus on the 10% doped CTF, CTF10.

Recent studies have shown that CTF offers a reasonable compromise between performance and long-term stability, making it a good candidate for the rigorous conditions of industrial applications.

weight loss of LSF was higher than the one of BCF and of CTF (6.12 vs 3.23 and 1.21% respectively). After 5 cycles, the weight loss was stable for CTF (1.22%) but still decreasing for LFS and BCF (6.31 and 3.42%). Among these three perovskites, CTF appeared to be the most stable under reducing atmosphere.

Although the first results on CTF stability are promising, long-term experiments under CO_2 and CH_4 for instance were not performed. Yet, it is important to assess the stability under these reactive atmospheres to meet the demand of certain applications.

- [1] United Nations, Paris Agreement, 2015.
- [2] Edenhofer O., R. Pichs-Madruga, Y. Sokona, S. Kadner, J. C. Minx, S. Brunner, S. Agrawala, G. Baiocchi, I. A. Bashmakov, G. Blanco, J. Broome, T. Bruckner, M. Bustamante, L. Clarke, M. Conte Grand, F. Creutzig, X. Cruz-Núñez, S. Dhakal, N. K. Dubash, P. Eickemeier, E. Farahani, M. Fishedick, M. Fleurbaey, R. Gerlagh, L. Gómez-Echeverri, S. Gupta, J. Harnisch, K. Jiang, F. Jotzo, S. Kartha, S. Klasen, C. Kolstad, V. Krey, H. Kunreuther, O. Lucon, O. Masera, Y. Mulugetta, R. B. Norgaard, A. Patt, N. H. Ravindranath, K. Riahi, J. Roy, A. Sagar, R. Schaeffer, S. Schlömer, K. C. Seto, K. Seyboth, R. Sims, P. Smith, E. Somanathan, R. Stavins, C. von Stechow, T. Sterner, T. Sugiyama, S. Suh, D. Ürge-Vorsatz, K. Urama, A. Venables, D. G. Victor, E. Weber, D. Zhou, J. Zou, and T. Zwickel, 2014: Technical Summary. In: *Climate Change 2014: Mitigation of Climate Change. Contribution of Working Group III to the Fifth Assessment Report of the Intergovernmental Panel on Climate Change* [Edenhofer, O., R. Pichs-Madruga, Y. Sokona, E. Farahani, S. Kadner, K. Seyboth, A. Adler, I. Baum, S. Brunner, P. Eickemeier, B. Kriemann, J. Savolainen, S. Schlömer, C. von Stechow, T. Zwickel and J. C. Minx (eds.)]. Cambridge University Press, Cambridge, United Kingdom and New York, NY, USA.
- [3] IPCC, *Climate Change 2014 Synthesis Report Summary Chapter for Policymakers*, IPCC. (2014) 31.
- [4] J.G.J. Olivier, G. Janseens-Maenhout, M. Muntean, J.A.H.W. Peters, *Trends in Global CO₂ Emissions 2016 Report*, PBL Netherlands Environ. Assess. Agency Eur. Comm. Jt. Res. Cent. (2016) 6–86.
- [5] M. Cyperek, P. Zapp, H.J.M. Bouwmeester, M. Modigell, K. Ebert, I. Voigt, W.A. Meulenber, L. Singheiser, D. Stvöer, *Gas separation membranes for zero-emission fossil power plants: MEM-BRAIN*, *J. Memb. Sci.* 359 (2010) 149–159.
- [6] M.A. Habib, M. Nemitallah, R. Ben-Mansour, *Recent development in oxy-combustion technology and its applications to gas turbine combustors and ITM reactors*, *Energy and Fuels.* 27 (2013) 2–19.
- [7] D.Y.C. Leung, G. Caramanna, M.M. Maroto-Valer, *An overview of current status of carbon dioxide capture and storage technologies*, *Renew. Sustain. Energy Rev.* 39 (2014) 426–443.
- [8] M. Kanniche, R. Gros-Bonnivard, P. Jaud, J. Valle-Marcos, J.M. Amann, C. Bouallou, *Pre-combustion, post-combustion and oxy-combustion in thermal power plant for CO₂ capture*, *Appl. Therm. Eng.* 30 (2010) 53–62.
- [9] Global CCS institute, *The Global Status of CCS 2016 Summary Report*, (2016) 1–28.
- [10] H. Stadler, F. Beggel, M. Habermehl, B. Persigehl, R. Kneer, M. Modigell, P. Jeschke, *Oxyfuel coal combustion by efficient integration of oxygen transport membranes*, *Int. J. Greenh. Gas Control.* 5 (2011) 7–15.
- [11] J. Davison, *Performance and costs of power plants with capture and storage of CO₂*, *Energy.* 32 (2007) 1163–1176.
- [12] S. Gupta, M.K. Mahapatra, P. Singh, *Lanthanum chromite based perovskites for oxygen transport membrane*, *Mater. Sci. Eng. R Reports.* 90 (2015) 1–36.
- [13] R. Castillo, *Thermodynamic analysis of a hard coal oxyfuel power plant with high temperature three-end membrane for air separation*, *Appl. Energy.* 88 (2011) 1480–1493.
- [14] A.C. Bose, G.J. Stiegel, P.A. Armstrong, B.J. Halper, E.P. Foster, *Chapter 1: Progress in Ion Transport Membranes for Gas Separation Applications*, 2009.
- [15] S. Gupta, J.J. Adams, J.R. Wilson, E.G. Eddings, M.K. Mahapatra, P. Singh, *Performance and post-test characterization of an OTM system in an experimental coal gasifier*, *Appl. Energy.* 165 (2016) 72–80.
- [16] J. Sunarso, S. Baumann, J.M. Serra, W.A. Meulenber, S. Liu, Y.S. Lin, J.C. Diniz da Costa, *Mixed*

ionic-electronic conducting (MIEC) ceramic-based membranes for oxygen separation, *J. Memb. Sci.* 320 (2008) 13–41.

- [17] T. Ishihara, Oxygen surface exchange and diffusion in LaGaO₃ based perovskite type oxides, *Solid State Ionics*. 113–115 (1998) 593–600.
- [18] P.M. Geffroy, A. Vivet, J. Fouletier, N. Richet, P. Del Gallo, T. Chartier, Influence of Oxygen Surface Exchanges on Oxygen Semi-Permeation through La_(1-x)Sr_xFe_(1-y)Ga_yO_{3-δ} Dense Membrane, *J. Electrochem. Soc.* 158 (2011) B971.
- [19] M. Guillodo, J. Fouletier, L. Dessemond, P. Del Gallo, Oxygen Permeation Through Dense Bi₂V_{0.9}Cu_{0.1}O_{5.35} Ceramic Membranes, *J. Electrochem. Soc.* 149 (2002) 93–99.
- [20] J. Fouletier, P. Fabry, M. Kleitz, Electrochemical Semipermeability and the Electrode Microsystem in Solid Oxide Electrolyte Cells, *J. Electrochem. Soc.* 123 (1976) 204.
- [21] M. Kleitz, Réactions d'électrode dans les oxydes électrolytes solides, Grenoble University, 1968.
- [22] M. Kleitz, P. Fabry, E. Schouler, Electrode polarization and electronic conductivity determination in solid electrolytes, in: *Fast Ion Transp. Solids*, W. van Goo, Amsterdam : North Holland Pub. Co, 1973: pp. 439–451.
- [23] C. Salles, J. Fouletier, D. Marinha, M.C. Steil, Determining the rate-limiting step during oxygen semi-permeation of CaTi_{0.9}Fe_{0.1}O_{3-δ} oxygen transport membranes, *J. Memb. Sci.* 527 (2017) 191–197.
- [24] P.M. Geffroy, A. Vivet, J. Fouletier, N. Richet, P. Del Gallo, T. Chartier, Influence of Oxygen Surface Exchanges on Oxygen Semi-Permeation through La_(1-x)Sr_xFe_(1-y)Ga_yO_{3-δ} Dense Membrane, *J. Electrochem. Soc.* 158 (2011) B971.
- [25] M.C. Steil, J. Fouletier, P.-M. Geffroy, Surface exchange polarization vs. gas concentration polarization in permeation through mixed ionic-electronic membranes, *J. Memb. Sci.* 541 (2017) 457–464.
- [26] J. Sunarso, S.S. Hashim, N. Zhu, W. Zhou, Perovskite oxides applications in high temperature oxygen separation, solid oxide fuel cell and membrane reactor: A review, *Prog. Energy Combust. Sci.* 61 (2017) 57–77.
- [27] Y. Wei, W. Yang, J. Caro, H. Wang, Dense ceramic oxygen permeable membranes and catalytic membrane reactors, *Chem. Eng. J.* 220 (2013) 185–203.
- [28] D.A. Slade, Mixed Ionic/Electronic Conducting Ceramic Membranes for Oxygen-Assisted CO₂ Reforming, Kansas School of Engineering, 2010.
- [29] S.M. Hashim, A.R. Mohamed, S. Bhatia, Current status of ceramic-based membranes for oxygen separation from air, *Adv. Colloid Interface Sci.* 160 (2010) 88–100.
- [30] S.F.P. Donkelaar, Development of Stable Oxygen Transport Membranes, Twente University, 2015.
- [31] S. Engels, F. Beggel, M. Modigell, H. Stadler, Simulation of a membrane unit for oxyfuel power plants under consideration of realistic BSCF membrane properties, *J. Memb. Sci.* 359 (2010) 93–101.
- [32] L. Rosen, N. Degenstein, M. Shah, J. Wilson, S. Kellya, J. Peck, M. Christie, Development of oxygen transport membranes for coal-based power generation, *Energy Procedia.* 4 (2011) 750–755.
- [33] L.L. Anderson, P.A. Armstrong, R.R. Broekhuis, M.F. Carolan, J. Chen, M.D. Hutcheon, C.A. Lewinsohn, C.F. Miller, J.M. Repasky, D.M. Taylor, C.M. Woods, Advances in ion transport membrane technology for oxygen and syngas production, *Solid State Ionics.* 288 (2016) 331–337.

- [34] F. Schulze-Küppers, S.F.P. ten Donkelaar, S. Baumann, P. Prigorodov, Y.J. Sohn, H.J.M. Bouwmeester, W.A. Meulenbergh, O. Guillon, Structural and functional properties of $\text{SrTi}_{1-x}\text{Fe}_x\text{O}_{3-\delta}$ ($0 < x < 1$) for the use as oxygen transport membrane, *Sep. Purif. Technol.* 147 (2015) 414–421.
- [35] J. Garcia-Fayos, V.B. Vert, M. Balaguer, C. Solís, C. Gaudillere, J.M. Serra, Oxygen transport membranes in a biomass/coal combined strategy for reducing CO_2 emissions: Permeation study of selected membranes under different CO_2 -rich atmospheres, *Catal. Today.* 257 (2015) 221–228.
- [36] A. Leo, S. Liu, J.C.D. da Costa, Development of mixed conducting membranes for clean coal energy delivery, *Int. J. Greenh. Gas Control.* 3 (2009) 357–367.
- [37] S.S. Hashim, A.R. Mohamed, S. Bhatia, Oxygen separation from air using ceramic-based membrane technology for sustainable fuel production and power generation, *Renew. Sustain. Energy Rev.* 15 (2011) 1284–1293.
- [38] V. White, J.M. Repasky, M.F. Carolan, P.A. Armstrong, V.E. Stein, E.P.T. Foster, ITM Oxygen Technology for Gasification Applications, in: *New Horizons Gasif.*, Rotterdam, 2014.
- [39] P.N. Dyer, R.E. Richards, S.L. Russek, D.M. Taylor, Ion transport membrane technology for oxygen separation and syngas production, *Solid State Ionics.* 134 (2000) 21–33.
- [40] C.F. Miller, J. Chen, M.F. Carolan, E.P. Foster, Advances in ion transport membrane technology for Syngas production, *Catal. Today.* 228 (2014) 152–157.
- [41] H. Jiang, H. Wang, S. Werth, T. Schiestel, J. Caro, Simultaneous production of hydrogen and synthesis gas by combining water splitting with partial oxidation of methane in a hollow-fiber membrane reactor, *Angew. Chemie - Int. Ed.* 47 (2008) 9341–9344.
- [42] J.M. Repasky, M.F. Carolan, D. Studer, C.M. Lowe, K.F. Gerdes, J. Smit, B. Bredmen, ITM Syngas: ceramic membrane technology for lower cost conversion of natural gas, in: *AIChE Spring Natl. Meet.* Vol. 4, 2010.
- [43] D.A. Slade, A.M. Duncan, K.J. Nordheden, S.M. Stagg-Williams, Mixed-conducting oxygen permeable ceramic membranes for the carbon dioxide reforming of methane, *Green Chem.* 9 (2007) 577.
- [44] E. Robinson, S. Aasland, Chen J., The application of oxygen transport membranes for syngas or hydrogen production, in: *AIChE Spring Meet.*, 2004.
- [45] J. Richter, P. Holtappels, T. Graule, T. Nakamura, L.J. Gauckler, Materials design for perovskite SOFC cathodes, *Monatshefte Fur Chemie.* 140 (2009) 985–999.
- [46] P.M. Geffroy, J. Fouletier, N. Richet, T. Chartier, Rational selection of MIEC materials in energy production processes, *Chem. Eng. Sci.* 87 (2013) 408–433.
- [47] A.F. Sammells, R.L. Cook, J.H. White, J.J. Osborne, R.C. MacDuff, Rational selection of advanced solid electrolytes for intermediate temperature fuel cells, *Solid State Ionics.* 52 (1992) 111–123.
- [48] V.V. Kharton, F.M.B. Marques, A. Atkinson, Transport properties of solid oxide electrolyte ceramics: A brief review, *Solid State Ionics.* 174 (2004) 135–149.
- [49] S. Hull, Superionics: crystal structures and conduction processes, *Reports Prog. Phys.* 67 (2004) 1233–1314.
- [50] <https://3dciencia.wordpress.com/2013/01/25/perovskite>.
- [51] R. ROY, Multiple Ion Substitution in the Perovskite Lattice, *J. Am. Ceram. Soc.* 37 (1954) 581–588.
- [52] V.V Kharton, A.A. Yaremchenko, A.V Kovalevsky, A.P. Viskup, E.N. Naumovich, P.F. Kerko, Perovskite-

type oxides for high-temperature oxygen separation membranes, 163 (1999) 307–317.

- [53] S. Xie, W. Liu, K. Wu, P.H. Yang, G.Y. Meng, C.S. Chen, Mixed oxygen ionic and electronic conduction in $\text{CaFe}_{0.2}\text{Ti}_{0.8}\text{O}_{3-\delta}$: a combined oxygen permeation and electrical conductivity study, *Solid State Ionics*. 118 (1999) 23–28.
- [54] H. Hayashi, H. Inaba, M. Matsuyama, N.G. Lan, M. Dokiya, H. Tagawa, Structural consideration on the ionic conductivity of perovskite-type oxides, *Solid State Ionics*. 122 (1999) 1–15.
- [55] M. Mogensen, D. Lybye, N. Bonanos, P.V. Hendriksen, F.W. Poulsen, Factors controlling the oxide ion conductivity of fluorite and perovskite structured oxides, *Solid State Ionics*. 174 (2004) 279–286.
- [56] M. Cherry, M.S. Islam, C.R.A. Catlow, Oxygen Ion Migration in Perovskite-Type Oxides, *J. Solid State Chem*. 118 (1995) 125–132.
- [57] P. Kofstad, T. Norby, *Defects and transport in crystalline solids*, 2007.
- [58] H.J.M. Bouwmeester, Dense ceramic membranes for oxygen separation, in: *Membr. Sci. Technol.*, Elsevier, 1996: pp. 435–528.
- [59] Y. Liu, X. Zhu, M. Li, H. Liu, Y. Cong, W. Yang, Stabilization of low-temperature degradation in mixed ionic and electronic conducting perovskite oxygen permeation membranes., *Angew. Chem. Int. Ed. Engl.* 52 (2013) 3232–6.
- [60] M.F. Carolan, P.N. Dyer, S.M. Fine, J.M. LaBar Sr., R.M. Thorogood, Process for recovering oxygen from gaseous mixtures containing water or carbon dioxide which process employs ion transport membranes, (1992).
- [61] M.F. Carolan, P.N. Dyer, J.M. LaBar Sr., R.M. Thorogood, Process for recovering oxygen from gaseous mixtures containing water or carbon dioxide which process employs ion transport membranes, (1992).
- [62] Z. Shao, W. Yang, Y. Cong, H. Dong, J. Tong, G. Xiong, Investigation of the permeation behavior and stability of a $\text{Ba}_{0.5}\text{Sr}_{0.5}\text{Co}_{0.8}\text{Fe}_{0.2}\text{O}_{3-\delta}$ oxygen membrane, *J. Memb. Sci.* 172 (2000) 177–188.
- [63] A.V. Kovalevsky, A.A. Yaremchenko, V.A. Kolotygin, F.M.M. Snijkers, V.V. Kharton, A. Buekenhoudt, J.J. Luyten, Oxygen permeability and stability of asymmetric multilayer $\text{Ba}_{0.5}\text{Sr}_{0.5}\text{Co}_{0.8}\text{Fe}_{0.2}\text{O}_{3-\delta}$ ceramic membranes, *Solid State Ionics*. 192 (2011) 677–681.
- [64] M. Arnold, H. Wang, A. Feldhoff, Influence of CO_2 on the oxygen permeation performance and the microstructure of perovskite-type $(\text{Ba}_{0.5}\text{Sr}_{0.5})(\text{Co}_{0.8}\text{Fe}_{0.2})\text{O}_{3-\delta}$ membranes, *J. Memb. Sci.* 293 (2007) 44–52.
- [65] A. Leo, S. Liu, J.C. Diniz Da Costa, Production of pure oxygen from BSCF hollow fiber membranes using steam sweep, *Sep. Purif. Technol.* 78 (2011) 220–227.
- [66] J.-C. Grenier, F. Menil, M. Pouchard, P. Hagenmuller, Mössbauer resonance studies in the CaTiO_3 - $\text{Ca}_2\text{Fe}_2\text{O}_5$ system, *Mater. Res. Bull.* 13 (1978) 329–337.
- [67] A. Becerro, F. Langenhorst, The transition from short-range to long-range ordering of oxygen vacancies in $\text{CaFe}_x\text{Ti}_{1-x}\text{O}_{3-x/2}$ perovskites, *J. Phys. Condens. Matter.* (2000) 3933–3941.
- [68] A.I. Becerro, C. McCammon, F. Langenhorst, F. Seifert, R. Angel, Oxygen vacancy ordering in CaTiO_3 - $\text{CaFeO}_{2.5}$ perovskites: From isolated defects to infinite sheets, *Phase Transitions*. 69 (1999) 133–146.
- [69] H. Iwahara, T. Esaka, T. Mangahara, Mixed conduction and oxygen permeation in the substituted oxides for CaTiO_3 , *J. Appl. Electrochem.* 18 (1988) 173–177.

- [70] S. Marion, A.I. Becerro, T. Norby, Ionic and electronic conductivity in $\text{CaTi}_{1-x}\text{Fe}_x\text{O}_{3-\delta}$ ($x=0.1-0.3$), *Ionics* (Kiel). 5 (1999) 385–392.
- [71] M.-L. Fontaine, J.B. Smith, Y. Larring, R. Bredesen, On the preparation of asymmetric $\text{CaTi}_{0.9}\text{Fe}_{0.1}\text{O}_{3-\delta}$ membranes by tape-casting and co-sintering process, *J. Memb. Sci.* 326 (2009) 310–315.
- [72] F.M. Figueiredo, V.V. Kharton, A.P. Viskup, J.R. Frade, Surface enhanced oxygen permeation in $\text{CaTi}_{(1-x)}\text{Fe}_x\text{O}_{3-\delta}$ ceramic membranes, *J. Memb. Sci.* 236 (2004) 73–80.
- [73] F.M. Figueiredo, V.V. Kharton, J.C. Waerenborgh, A.P. Viskup, E.N. Naumovich, J.R. Frade, Influence of Microstructure on the Electrical Properties of Iron-Substituted Calcium Titanate Ceramics, *J. Am. Ceram. Soc.* 87 (2004) 2252–2261.
- [74] J.M. Polfus, W. Xing, M. Riktor, M.F. Sunding, P.I. Dahl, S.M. Hanetho, T. Mokkelbost, Y. Larring, M.-L. Fontaine, R. Bredesen, Enhanced O_2 Flux of $\text{CaTi}_{0.85}\text{Fe}_{0.15}\text{O}_{3-\delta}$ Based Membranes by Mn Doping, *J. Am. Ceram. Soc.* 99 (2016) 1071–1078.
- [75] J.M. Polfus, W. Xing, M.F. Sunding, S.M. Hanetho, P.I. Dahl, Y. Larring, M.-L. Fontaine, R. Bredesen, Doping strategies for increased oxygen permeability of CaTiO_3 based membranes, *J. Memb. Sci.* 482 (2015) 137–143.
- [76] M. Balaguer, S. Escolástico, J.M. Serra, Oxygen permeation and stability of $\text{CaTi}_{0.73}\text{Fe}_{0.18}\text{Mg}_{0.09}\text{O}_{3-\delta}$ oxygen-transport membrane, *J. Memb. Sci.* 524 (2017) 56–63.
- [77] V.V. Kharton, A.V. Kovalevsky, A.P. Viskup, F.M. Figueiredo, A.A. Yaremchenko, E.N. Naumovich, F.M.B. Marques, Oxygen permeability and faradaic efficiency of $\text{Ce}_{0.8}\text{Gd}_{0.2}\text{O}_{2-d}-\text{La}_{0.7}\text{Sr}_{0.3}\text{MnO}_{3-d}$ composites, *J. Eur. Ceram. Soc.* 21 (2001) 1763–1767.
- [78] G.B. Haxel, J.B. Hedrick, G.J. Orris, Rare Earth Elements — Critical Resources for High Technology, *United States Geol. Surv. Fact Sheet.* 87 (2002) 4.
- [79] European Commission, Critical raw materials for the EU, Report of the Ad-hoc Working Group on defining critical raw materials, *Eucom.* 39 (2010) 1–84.
- [80] F.M. Figueiredo, M.R. Soares, V. V. Kharton, E.N. Naumovich, J.C. Waerenborgh, J.R. Frade, Properties of $\text{CaTi}_{1-x}\text{Fe}_x\text{O}_{3-\delta}$ Ceramic Membranes, *J. Electroceramics.* 13 (2004) 627–636.
- [81] Y. Chen, N. Galinsky, Z. Wang, F. Li, Investigation of perovskite supported composite oxides for chemical looping conversion of syngas, *Fuel.* 134 (2014) 521–530.
- [82] F.M. Figueiredo, V.V. Kharton, J.C. Waerenborgh, A.P. Viskup, E.N. Naumovich, J.R. Frade, Influence of Microstructure on the Electrical Properties of Iron-Substituted Calcium Titanate Ceramics, *J. Am. Ceram. Soc.* 87 (2004) 2252–2261.
- [83] F.M. Figueiredo, M.R. Soares, V.V. Kharton, E.N. Naumovich, J.C. Waerenborgh, J.R. Frade, Properties of $\text{CaTi}_{1-x}\text{Fe}_x\text{O}_{3-\delta}$ Ceramic Membranes, *J. Electroceramics.* 13 (2004) 627–636.

CHAPTER 2

EXPERIMENTAL SECTION

La vie est un voyage expérimental, accompli involontairement.
Fernando Pessoa (Le Livre de l'intranquillité, 1982)

Table of content

| | | |
|-----|---|----|
| 1. | Introduction..... | 38 |
| 2. | Oxygen permeation setups..... | 39 |
| 2.1 | Standard setups..... | 39 |
| 2.2 | Electrochemical surface probes | 42 |
| | Reactivity test between YSZ and CTF | 45 |
| 3. | Isotopic exchange | 47 |
| 4. | TPR measurements..... | 48 |
| 5. | Impedance spectroscopy..... | 49 |
| 6. | XRD | 50 |
| 7. | Redox stability potential..... | 51 |
| 8. | Mössbauer spectroscopy..... | 52 |

1. Introduction

This chapter summarizes the main techniques used during this PhD, namely the setups for the oxygen permeation measurements, isotopic exchange measurements, Temperature programmed reduction (TPR) measurements, impedance spectroscopy, XRD, Redox stability potential and Mössbauer spectroscopy.

Because the technique to measure the oxygen semi-permeability is unconventional, the OTM techniques section contains an overview of more standard oxygen measurement techniques so that differences can be better understood. An important part in this chapter is dedicated to the description of the specific setup which enables to measure the oxygen activity on the surface of the membrane. This is important to be able to determine the limiting steps. This can also be done by isotopic exchange measurements, technique which is also introduced in this chapter.

Conditions of some standard techniques (XRD, impedance spectroscopy) are described in this chapter as well as techniques less common as Temperature Programmed Reduction (TPR) measurements, Mössbauer spectroscopy, and Redox stability potential which investigate the CTF behavior under reductive atmospheres.

2. Oxygen permeation setups

The driving force for oxygen permeation is the oxygen partial pressure gradient across the OTM. Experimentally, this gradient was imposed by feeding an oxidizing atmosphere (oxygen-rich gas) and an inert or reducing atmosphere (oxygen lean gas) to each side of the membrane. On the oxygen-rich side, a wide range of partial pressures was obtained by mixing oxygen, air, and nitrogen using calibrated mass flow controllers. On the lean side, different inert or reducing atmosphere compositions were used: argon or helium but also 1% CO₂, 2% CO, and 5% CH₄ balance helium, and 3% H₂ balance argon.

In the setups used during this study, the membrane is sealed between two alumina tubes with gold rings to obtain a tight system. The gold seals can sustain higher testing temperatures and are less prone to contaminate the membrane than glass seals. In a temperature range, varying usually between 500 and 1000 °C, oxygen content in the sweep gases is commonly monitored using a Yttria-stabilized Zirconia-based oxygen sensor.

Another type of setup exists in the literature [1,2] which consists of a tubular zirconia oxygen electrochemical pump with a disk-shaped zirconia oxygen sensor, and the ceramic membrane. This setup is used only with a small difference between the oxygen partial pressures of the both sides of the membrane. This enables the authors to make some assumptions, especially on the constant conductivity within this oxygen partial pressure range, which can be discussed.

2.1 Standard setups

Two different setups were used during this PhD. The first one, setup A, was developed in LEPMI and the second one, setup B, was installed in Saint-Gobain CREE during the PhD.

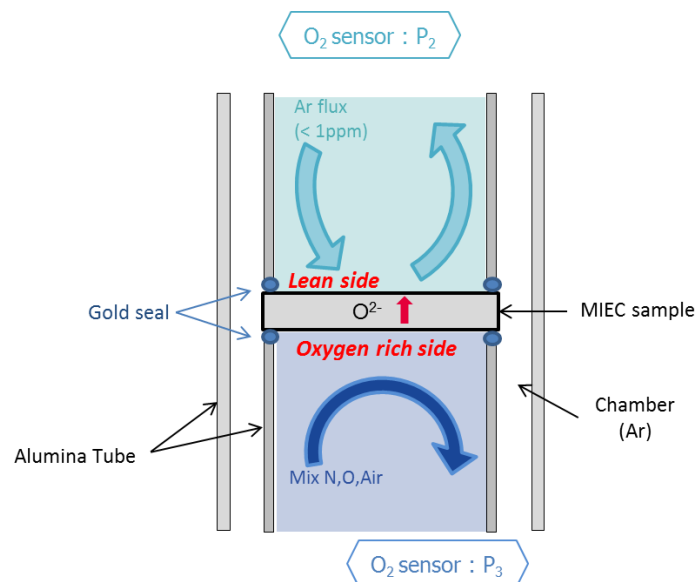


Figure 1: Schematic representation of the setup A used to measure the oxygen semi-permeation flux in Grenoble.

Permeability measurements are performed on a dense membrane. In LEPMI, sealing is achieved with gold O-rings pressed at high temperature between two alumina tubes and the membrane. To ensure a good alignment of the tubes, the gold-O-rings, and the pellet, glue was used to fix first a gold-O rings and the pellet on the lower alumina tube (Figure 2 a)). The other gold O-ring is also glued to the upper tube (Figure 2 b)).

This system is placed inside another alumina tube to create a guard-chamber with argon flow to limit the impact of eventual leakage (Figure 1). The whole equipment is inside a tubular furnace.

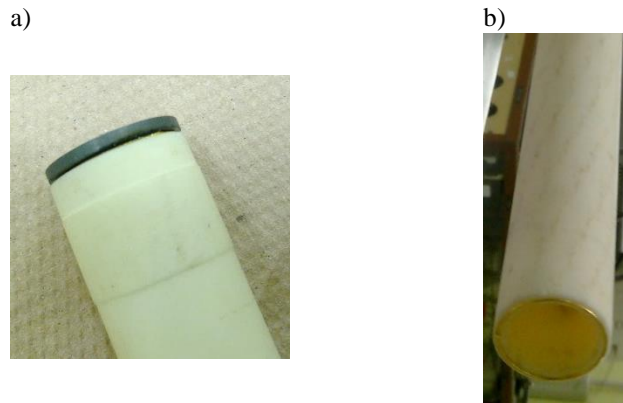


Figure 2: a) Lower alumina tube with a gold-O-ring and the membrane b) Upper alumina tube with gold -O-ring.

On the oxygen-rich side of the membrane, the oxygen partial pressure P_3 is monitored with a laboratory made oxygen sensor [3,4]. A wide range of partial pressures can be obtained by mixing oxygen, air, and nitrogen fluxes with mass flow sensors. On the lean side of the membrane, the carrier gas is argon ($P_{O_2} \approx 10^{-6}$) with a flow rate, $d = 6 \text{ L h}^{-1}$.

In LEPMI, permeability measurements were performed on a dense membrane with an effective oxygen semi-permeation surface area of 2.01 cm^2 . We measured a leak of the order 10^{-5} bar or less at $500 \text{ }^\circ\text{C}$, in the absence of permeation, which was used to correct all flux values reported in this manuscript.

In Saint-Gobain CREE, the setup B is a commercial system (ProboStat™, NorECs), which is integrated in a split furnace and connected to an oxygen gauge (SETNAG) to monitor the semi-permeation. A gas area with different reactive gases is also connected to simulate different conditions (Figure 3).

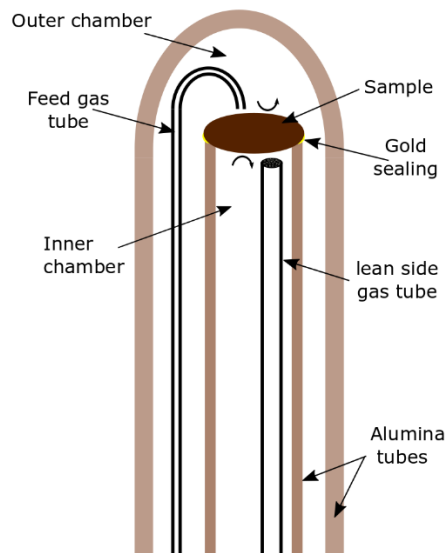


Figure 3: Schematic of the ProboStat™ inside the enclosing tube

Permeability measurements are performed on a dense membrane. Sealing was achieved with a gold O-ring pressed between an alumina tube and a spring load system (Figure 3, Figure 4). The system was heated until $1060 \text{ }^\circ\text{C}$ and the sealing is followed with specific connections.



Figure 4: a) Support tube, gold seal, sample, spring load system, and gas supply tube [5]. b) Picture of the bench B in Saint-Gobain CREE.

Air was used as oxidizing atmosphere on the outer chamber. In the inner chamber, i.e. the lean side of the membrane, different sweep gases flew to simulate different atmospheres. An oxygen gauge (SETNAG) can either measure the oxygen partial pressure before or after the inner chamber and measurements were constantly recorded. The exit of the inner chamber is connected to the SETNAG with some valves and pressure sensors on the way so there is a certain distance between the two equipment. However, the tightness was verified, pressurizing the line to confirm that no air leakage influences the oxygen measurement.

Permeability measurements were performed on a dense membrane with an effective oxygen semi-permeation surface area of 3.46 cm^2 . We measured a leak of the order 10^{-5} bar at $500 \text{ }^\circ\text{C}$, in the absence of permeation, which was used to correct all flux values reported in this manuscript.

For both setups, the specific oxygen permeability, J_{O_2} , was calculated assuming that the inlet and outlet flow rate of the lean side were identical (Equation 1).

$$J_{O_2} = \frac{\Delta P (d \cdot L)}{P_t \cdot V_m A} \quad \text{Equation 1}$$

J_{O_2} : Specific oxygen permeability ($\text{mol} \cdot \text{cm}^{-1} \cdot \text{s}^{-1}$)

d : Flow-rate of the carrier gas on the lean side of the membrane ($\text{L} \cdot \text{s}^{-1}$ NTP)

$\frac{L}{A}$: Ratio between thickness and effective reactive area of the membrane (cm^{-1})

V_m : Molar volume of an ideal gas at 1 atm and $25 \text{ }^\circ\text{C}$

$\Delta P = P_2 - P_1$: Change in oxygen partial pressure as a result of oxygen semi-permeability on the lean side (bar)

P_1 : Oxygen partial pressure in the carrier gas upstream of the membrane (bar)

P_2 : Oxygen partial pressure downstream of the membrane (bar)

P_t : Total pressure: 1 bar in our experiments

It is worth noting that through this work, all flux semi-permeability values are specific oxygen permeability, J_{O_2} , which corresponds to the oxygen flux semi permeability, j_{O_2} , normalized by the membrane thickness, L , such that $j_{O_2} = J_{O_2}/L$.

2.2 Electrochemical surface probes

As explained before, oxygen-semi permeation can either be limited by the surface exchange reactions or the bulk diffusion or both of them. The straightforward way to identify which is the rate limiting step is to perform multiple oxygen semi-permeability flux measurements while changing the membranes dimensions. However, this is extremely time-consuming considering that the characteristic time for measuring a single specimen is at least one week.

Alternatively, it is possible to determine the rate limiting step with a single sample with the use of electrochemical surface probes [6–8]. The principle involves measuring the oxygen activity on the lean side surface (which is associated with a corresponding equivalent oxygen partial pressure P_2^*) with electrochemical surface probes. The measurements focus on the lean side because it was demonstrated that surface polarization on the oxygen-rich side was negligible compared with the oxygen lean side, indicating that the former was not limiting. Indeed, at 850 °C, the polarization was ≈ 1 mV on the oxygen-rich side, which was considered as negligible, compared to the ≈ 38 mV on the oxygen lean side.

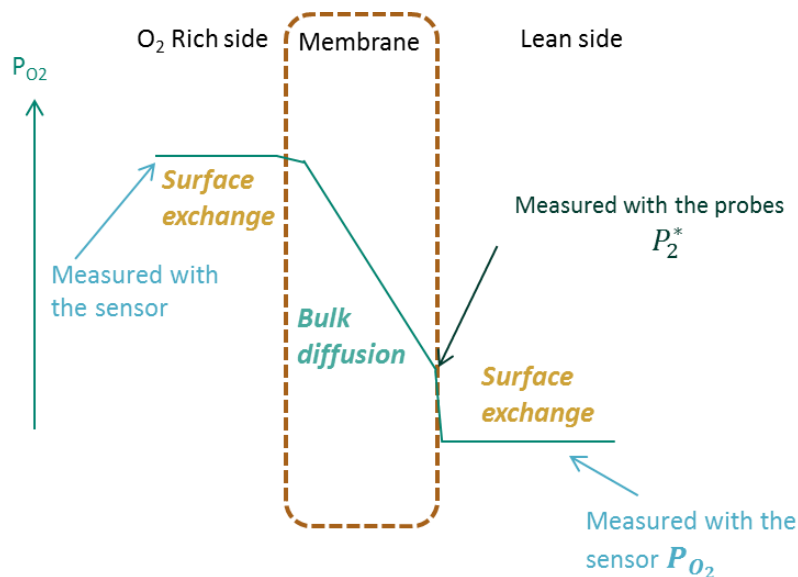


Figure 5 : Schematic representation of the oxygen partial pressures measured with the setup with the micro probes.

The use of an ionic conductor ceramic and a metallic probes creates, with the MIEC, an electrochemical chain. The measurements of the electromotive force enables to determine the oxygen activity on the lean surface of the membrane, which is considered to be equal to oxygen partial pressure on the surface of the membrane P_2^* . This enables to determine the drop in oxygen partial pressure between both surfaces and between the lean side surface and the gas. This gives information on the impact of surface exchange reactions and oxygen bulk diffusion.

Two probes are put on the surface of the membrane as described in Figure 6. One is metallic, and the other one is a cone shaped oxygen-ion conductive ceramic (Figure 7). Probes in platinum, gold or silver and in gadolinia doped ceria (*GDC*), yttria stabilized zirconia (*YSZ*) or in apatite were used during the study to ensure the nature of the probes do not affect the semi-permeation process.

The ceramic probe is a pure ionic conductor under operation condition. These two probes create, with the material, an electrochemical chain. There are different interfaces:

- α : between the Pt-I wire and the metallic probe;
- β : between the metallic probe and the MIEC where electrons are in equilibrium.
- χ : between the MIEC and the ceramic probe where oxygen ions are in equilibrium.
- δ : between the ceramic probe, the platinum wire which is around the probe and the oxygen from the gas. This is the place where oxygen from the gas react with the electrons to form the oxygen ions inside the probe.
- ε : between the platinum wire around the probe and the Pt II where electrons are also in equilibrium.

Figure 7 shows a representation of the qualitative variation of the electric potential along this chain. The electromotive force, E_s , measured between the two probes (between Pt-I and Pt-II) enables to calculate the oxygen activity on the surface (Equation 13).

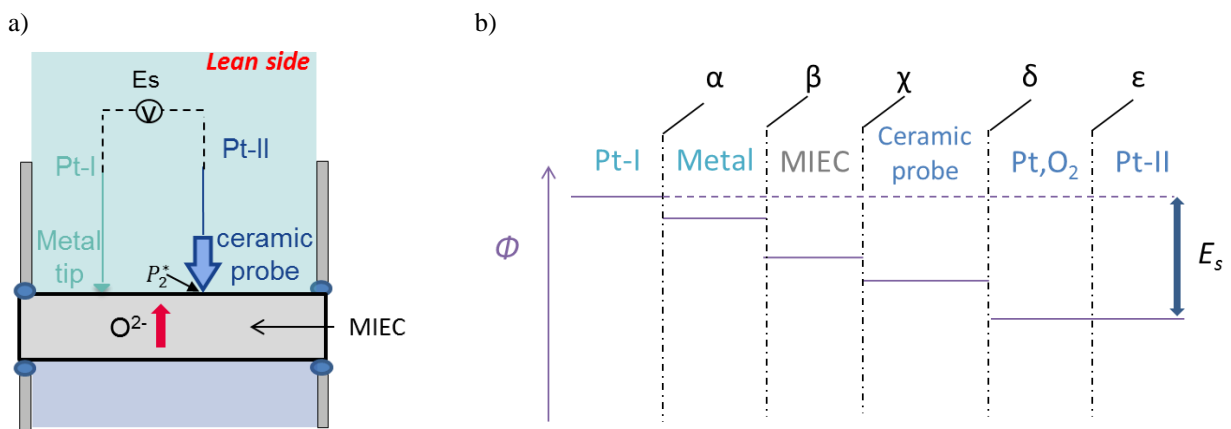


Figure 6: a) Schematic of the setup allowing the measurement of the oxygen activity on the lean side of the membrane with the two electrochemical surface probes. b) : Qualitative variation of the potential Φ along the chain, with the metallic probes and the ceramic cone-shaped probe (inspired from [8]). The α , β , χ , δ , ε represent the different interfaces within the chain.

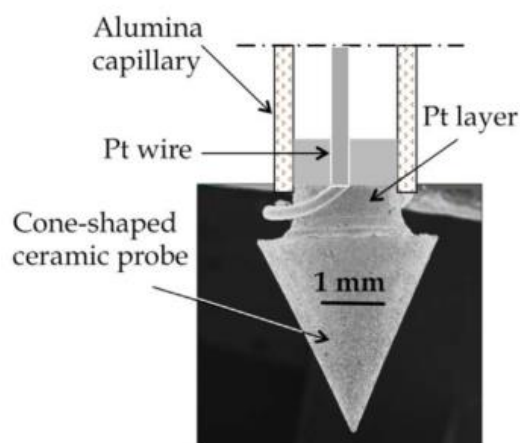


Figure 7: Cone shaped ceramic probes with the Pt wire around it.

The different equilibria are written:

- Electronic equilibrium at interfaces α and β (assuming that there is no catalytic activity of the metal for the oxygen electrode reaction)

$$\tilde{\mu}_e^{Pt-I} = \tilde{\mu}_e^{Me} = \tilde{\mu}_e^{MIEC} \quad \text{Equation 2}$$

- Ionic equilibrium at interface χ

$$\tilde{\mu}_{O_2^{2-}}^{MIEC} = \tilde{\mu}_{O_2^{2-}}^{ceramic} \quad \text{Equation 3}$$

- Electrochemical equilibrium at interface δ :

$$\frac{1}{2}O_{2(gas)} + 2e_{Pt}^- = O_{ceramic}^{2-} \quad \text{Equation 4}$$

$$\frac{1}{2}\mu_{O_2} + 2\tilde{\mu}_e^{Pt} = \tilde{\mu}_{O_2^{2-}}^{ceramic} \quad \text{Equation 5}$$

- Electronic equilibrium at interface ε :

$$\tilde{\mu}_e^{Pt-II} = \tilde{\mu}_e^{Pt} \quad \text{Equation 6}$$

It was shown that the oxygen activity on the surface of the material (defined as an equivalent of the oxygen partial pressure on the surface of the material P_2^*) is different from the oxygen partial pressure in the gas, P_{O_2} . Oxygen activity on the surface can be expressed according to the following equilibrium:

$$\frac{1}{2}O_{2(surface)} + 2e_{MIEC}^- = O_{MIEC}^{2-} \quad \text{Equation 7}$$

Leading to:

$$\frac{1}{2}\mu_{O_2}^* + 2\tilde{\mu}_e^{MIEC} = \tilde{\mu}_{O_2^{2-}}^{MIEC} \quad \text{Equation 8}$$

The electrochemical potential is defined according to Equation 9:

$$\tilde{\mu}_e^{MIEC} = \mu_e^{MIEC} - F\phi^{MIEC} \quad \text{Equation 9}$$

Consequently, Equation 8 becomes:

$$\frac{1}{2}\mu_{O_2}^* + 2\mu_e^{MIEC} - 2F\phi^{MIEC} = \tilde{\mu}_{O_2^{2-}}^{MIEC} \quad \text{Equation 10}$$

Combining Equation 3, Equation 5 and Equation 10:

$$\frac{1}{2}\mu_{O_2} + 2\tilde{\mu}_e^{Pt} = \frac{1}{2}\mu_{O_2}^* + 2\mu_e^{MIEC} - 2F\phi^{MIEC} \quad \text{Equation 11}$$

Assuming that $\mu_{O_2} = RT \ln P_{O_2}$, Equation 2 and Equation 11 become

$$\frac{RT}{2} \ln P_{O_2} + 2\mu_e^{Pt} - 2F\phi^{Pt} = \frac{RT}{2} \ln P_{O_2}^* + 2\mu_e^{Pt-I} - 2F\phi^{Pt-I} \quad \text{Equation 12}$$

$$E_s = \phi^{Pt-I} - \phi^{Pt-II} = \frac{RT}{4F} \ln \left(\frac{P_{O_2}^*}{P_{O_2}} \right) \quad \text{Equation 13}$$

The measurement of the electromotive force between the probes (E_s) enables then to determine P_2^* and to quantify the surface polarization (Equation 13).

It is then possible to separate the influence of the bulk diffusion (a driving force proportional to the oxygen pressure gradient across the bulk between P_3 and P_2^*) from the influence of surface exchange reactions (a driving force proportional to the oxygen pressure gradient between P_2^* and P_2) (Figure 5).

These equations depend on some conditions.

First, the oxygen partial pressure measured at the top of the ceramic tip is considered identical to the one measured downstream of the cell. This is in accordance with previous studies, because of the cell design and the oxygen partial pressure range in the lean chamber [8–10].

Then, the surface of the MIEC is considered to be equipotential, which was confirmed moving the probes across the membrane and verifying that the electromotive force is constant.

Further, it was assumed that there is no catalytic activity of the metal with the MIEC, which was confirmed measuring a constant electromotive force for a long duration measurement under the same experimental conditions. Reactivity tests were also performed between YSZ (which is more reactive than apatite) and CTF to see if any reaction phases are formed.

Reactivity test between YSZ and CTF

To use zirconia as a ceramic point electrode, it requires to verify that there is no reactivity with the CTF, which could distort the results. A mix of 50% YSZ-8Y and 50% CTF-SG powders was calcined at 1000 °C for 10 h. The presence of reaction phases was verified by XRD (Figure 8), which shows only the peaks corresponding to the initial YSZ and CTF phases. Based on these experiments we expect no interaction between zirconia and CTF under experimental conditions.

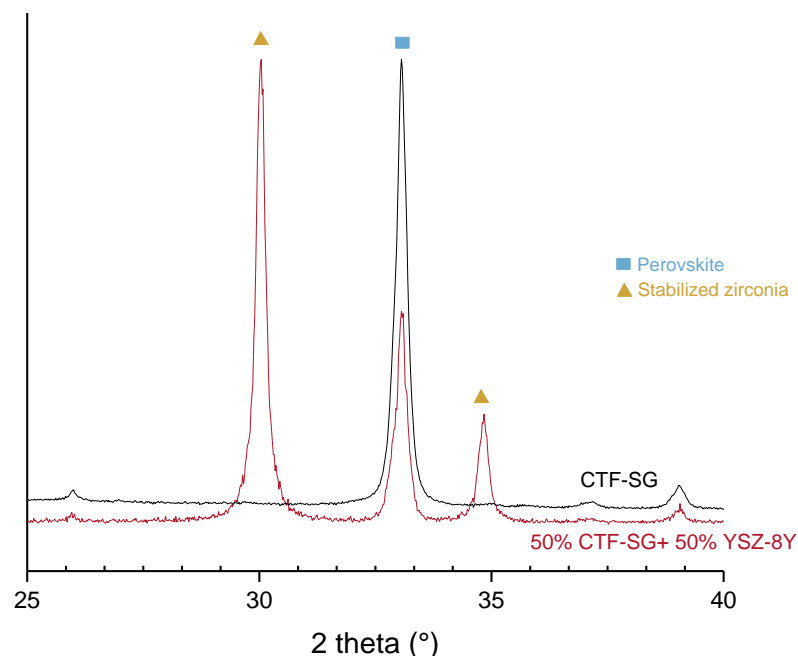


Figure 8: Details of the main normalized peaks of the stabilized zirconia and perovskite phase of CTF. Comparison between the XRD graphs of CTF-SG and the mix of CTF-SG and zirconia showing no additional reflections. Data are collected with the D5000 diffractometer, using procedure Q-PRO-STR-08-30 with a, 0.02 ° step and 1 s/step rate.

To confirm this results a method more sensitive to chemical changes than XRD, conductivity measurement, was used. Indeed, even small amounts of insulating phase formation at the interface would result in current constriction and a significant increase of resistance.

A pellet of YSZ-8Y was pressed and sintered at 1400 °C for 5 h then a solution of CTF (6 g of water, 0.26 g of ProxBO₃, 8 g of CTF) was spin-coated on it. The pellet was fired again at 1400 °C for 5 h. The total conductivity of the assembled sample was continuously measured by Impedance spectroscopy at 1000 °C during 5 days. Results show an initial decrease of total resistance, which stabilizes after 1 day. And so, it can be concluded that no insulating phases are being formed.

3. Isotopic exchange

Isotopic exchange experiments were performed to determine the oxygen diffusion coefficient, D^* , and the isotopic oxygen exchange coefficient, k^* . This method is based on the diffusion of ^{18}O within the material, measured with Secondary Ion Mass Spectroscopy (SIMS).

The sample is first annealed under ^{16}O at atmospheric pressure at a sufficiently high temperature to ensure that the material reaches thermodynamic equilibrium with the gas. Then, the material is quenched, the atmosphere switched to ^{18}O , and the system is reheated. During this second annealing step, the ^{18}O will exchange with ^{16}O and diffuse within the material. The annealing time should be sufficiently long to be able to observe diffusion but short enough to avoid ^{18}O to diffuse all the way over to the middle of the membrane. In this study, samples were annealed for 20 to 40 minutes depending on the temperature. The oxygen partial pressure is set at 210 mbar.

Pellets were cross sectioned in half. They are polished and SIMS analyses are completed on both pellet cross-sections. Profiles for both sides of the pellets can be then recorded. The normalized ^{18}O concentration profiles are fitted using the Crank relation, solution of the Fick's second law of the diffusion of a gas into a solid to obtain D^* and k^* . To validate the experiment, the concentration of ^{18}O at the end should be equal to 0.2%, the natural abundance of the isotope.

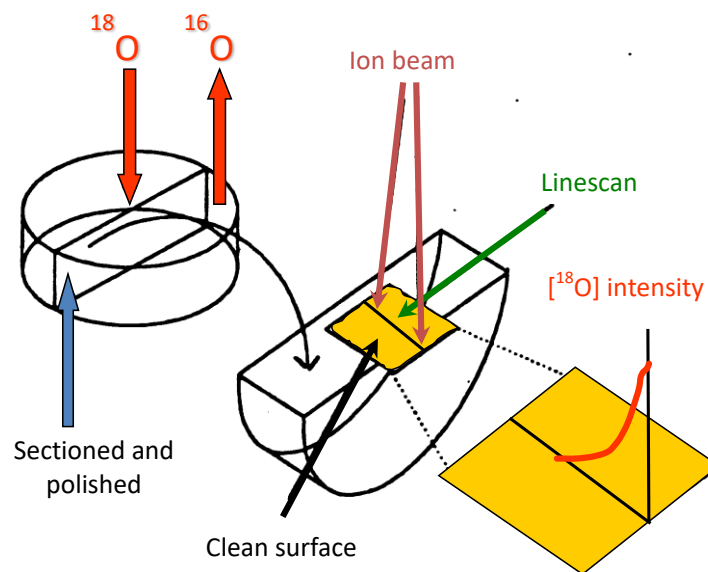


Figure 9: Schematic of the isotopic exchange.

4. TPR measurements

Temperature programmed reduction (TPR) experiments were performed on CTF powder to quantify the change in oxygen content as a function of temperature under H₂ (Autochem 2920 Micromeritics). A thermal conductivity detector (TCD) is used to measure changes in the thermal conductivity of the gas stream. The TCD signal is converted to concentration of active gas using a level calibration.

The powder is first heated (10 °C/min) under oxygen (30 ml/min) up to 800 °C. The sample is held at maximum temperature for 2 h to eliminate all the possible pollutant / carbonates, and then cooled under helium. 3% H₂ in argon (30 ml/min) is then sent at ambient temperature for 90 min to equilibrate the material. After that, the TCD recording starts and the sample is heated at 10 °C/min up to 1000 °C. Different peaks on the TCD signal can be seen, resulting to reduction of metal ions from the material.

Both qualitative and quantitative interpretation can be performed. First the peak position gives information at what temperature oxygen is released and metal ions are reduced, and comparison between different powders can be done. But it also enables to calculate the amount of metallic ion reduced during heating. A calibration of the equipment with different amount of hydrogen has to be done beforehand and according to the area under the TCD signal, the amount of hydrogen consumed can be obtained.

5. Impedance spectroscopy

The electrical conductivity of CTF was measured by impedance spectroscopy as a function of temperature and oxygen partial pressure. For this, dense CTF pellets were used and platinum electrodes (METALOR®) were painted to the surfaces, followed by drying for 3 h at 100 °C and fired at 1050 °C for 1 h. Impedance measurements (AMEL 7260) were performed between 150 - 800 °C, with a frequency range between 10 MHz - 0.1 Hz and with signal amplitude of 500 mV.

The oxygen partial pressure was controlled using an oxygen pump/gauge system (Gen'air_SETNAG) and different carrier gases (3% H₂/Ar, O₂ (Air liquid, 99.9995% purity) and O₂ (Messer, 99.9995% purity)).

The impedance spectra were interpreted assuming an equivalent circuit with one resistance in series with an R/CPE circuit corresponding to a slightly depressed semicircle in a typical Z'' versus Z' plot.

6. XRD

The crystal structure of CTF was examined at room temperature by a diffractometer (X'Pert from PANalytical) using Cu $K\alpha_m$ radiation. Standard qualitative measurements were recorded from 5 to 80° (2θ) with 0.03° step and 150 s per step. When lattice parameters were measured, diffraction patterns of the samples in the range of 10-125 °C were recorded with 0.017° step and 100 s per step. Phase identification was performed using Eva software (Bruker) and the lattice parameters were calculated with HighScore Plus software. Diffraction peaks were indexed using the CaTiO_3 crystal phase (PDF 00-042-0423) from ICDD 2016.

Additional spectra were recorded as a function of temperature in an Anton Paar HTK2000 reactor chamber. The diffractograms were recorded from 20 to 120° with 0.03° step and 100 s per step, every 100 °C between 600 and 1300 °C.

CTF theoretical density TD was calculated with the lattice volume obtained by XRD [11].

$$TD = \frac{Z \times M_{CTF}}{N_A \times V}$$

With Z the number of formula unit per cell which is equal to 4 for the CTF (because of the $Pnma$ structure), N_A the Avogadro number and M_{CTF} the molar weight of the CTF.

7. Redox stability potential

A method was proposed to determine the potentials at which reduction reactions of a ceramic conductor occur [12]. Basically the method consists of electrochemically reducing the investigated material by passing an appropriate cathodic direct current. As described previously [13], and shown in Figure 10, a small cylinder of the studied CTF material was put in contact with the bottom of a closed-ended yttria-stabilized zirconia tube. The top of the cylinder was covered by a platinum layer. The current intensity and the reduction time are chosen so that only the top of the CTF sample is reduced. The platinized external surface of the zirconia tube, in contact with air, serves as reference electrode.

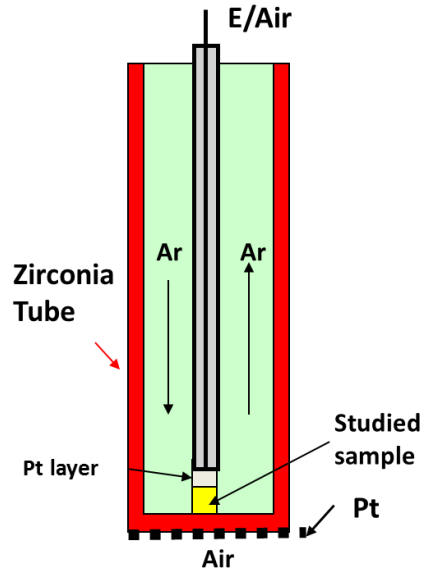


Figure 10: Schematic representation of the setup.

Figure 11 shows an example of the recorded relaxation potential of the cylinder-shape electrode vs. air. The depolarization curves show waves with inflexion points (referred to as (A), (B), and (C)) characteristic of dissolved redox systems. The study of these systems gives information of the valence state of species in CTF. In Figure 11, the inflexion points referred to as (D) and (E) are ascribed to superficial defects. It should be pointed out that the relaxation potentials were found to be independent of the oxygen pressure in the working chamber, whereas the shape of the curves depends on the oxygen concentration in the flowing gas.

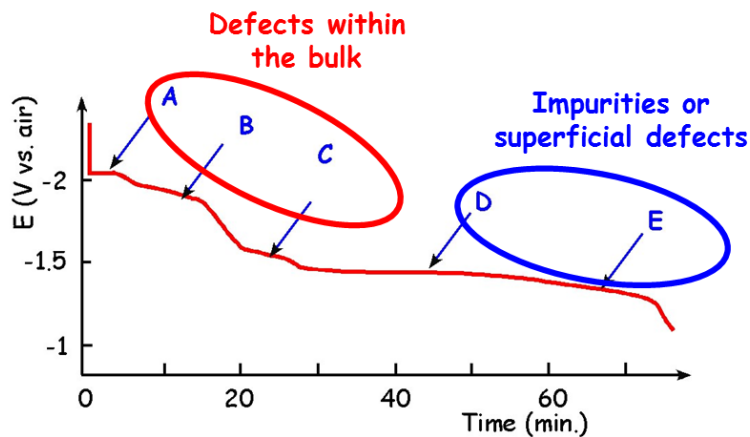


Figure 11: Example of depolarization curve.

8. Mössbauer spectroscopy

Mössbauer spectroscopy was used to study the iron valence and coordination on the CTF samples. The Mössbauer effect is a recoilless nuclear γ -rays resonance effect. A source produces a gamma nuclear radiation due to the transition between its excited to its fundamental state. This radiation is absorbed by the absorber, leading to a reverse transition. The Lamb-Mössbauer factor, f , is the fraction of nuclear transition which occur without recoil. The Mössbauer effect is observable only for this fraction. Only a small number of elements can be easily analyzed by Mössbauer spectroscopy, and the most important one ($\approx 90\%$ of publications) is iron⁵⁷. Usually, in the case of iron⁵⁷, a radioactive source of cobalt⁵⁷ is used in a rhodium matrix. Different parameters are calculated when analyzing a Mössbauer spectrum [14].

Due to the different electron density, nuclear radius and atom environment of the source and the absorber material, their transitions energies are not equal. The difference between these transition energies is referred to the isomer shift δ ($\delta = E_A - E_S$). On a typical Mössbauer spectrum, it corresponds to the difference between the barycenter of the resonance signal and the origin (zero velocity for the reference αFe) (Figure 12).

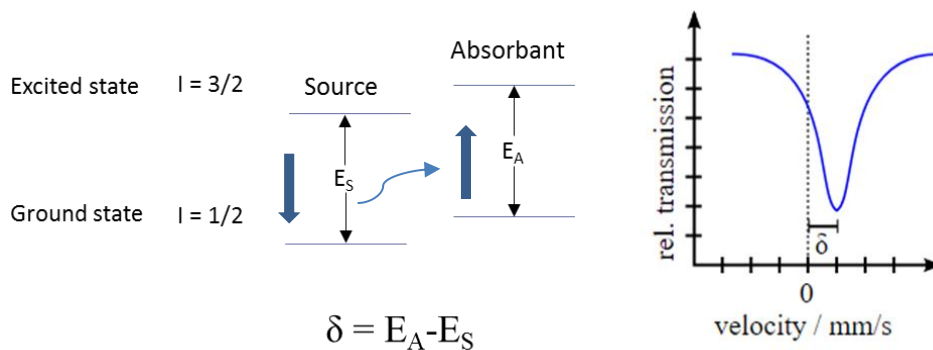


Figure 12: Schematic representation of the isomer shift δ .

Besides providing information on the electron distribution, the spin state, the local coordination, it is important to note that the isomer shift decreases with increasing the oxidation state [15]. Typical isomer shift values are given in Figure 13 for iron. It has to be noted that some isomer shifts for Fe^{III} and Fe^{IV} are on the same range so experimentally it may be difficult to differentiate them.

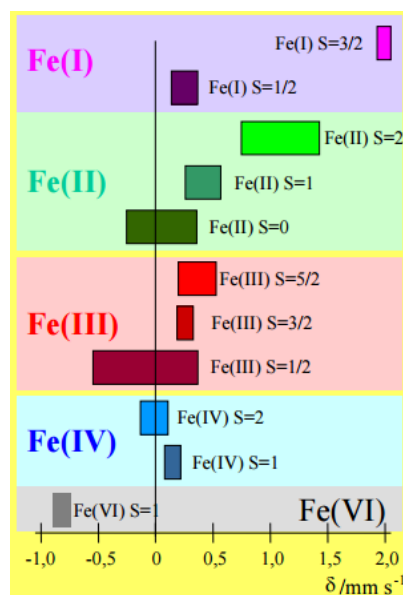


Figure 13: Typical isomer shifts for iron [16].

Nuclei with a spin higher than $\frac{1}{2}$ (i.e. the excited state of ^{57}Fe) have an electric quadrupole moment. The electric interaction between this electric quadrupole moment and the electric field gradient (EFG) (which is due to non-cubic valence electron distribution and/or non-cubic lattice site symmetry) splits the degenerate $I = 3/2$ level, described by a quadrupole splitting (Δ). On a typical Mössbauer spectrum, it is represented by the distance between the two peaks of the quadrupole doublet (Figure 14). The isomeric shift corresponds to the difference between the barycenter of the two peaks and the origin. It gives information on the local symmetry of the Mössbauer atom.

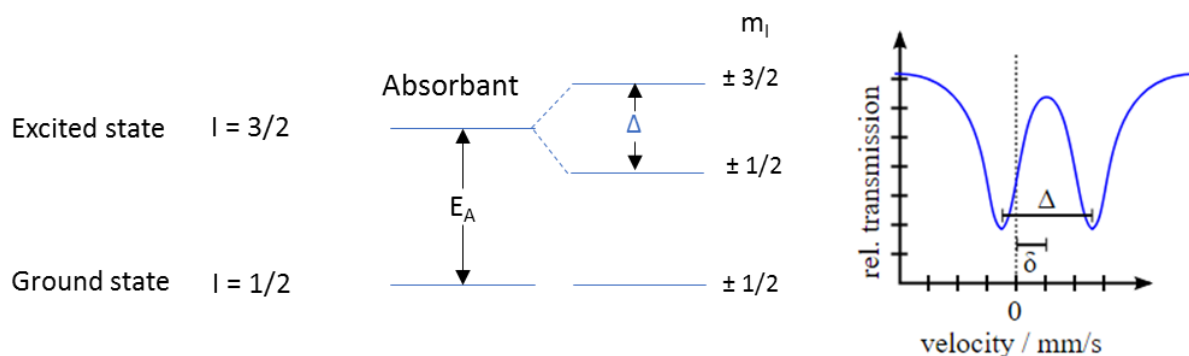


Figure 14: Schematic representation of the chemical splitting Δ .

^{55}Fe and ^{54}Fe for instance, can have a different coordination number (4, 5 or 6), then each atom with its particular valence and coordination number will induce a different pattern. The area of the pattern provides information on the relative population of the different phases but it was assumed in the calculation that the Lamb-Mössbauer factor, f , was identical for all the components.

In this study, Mössbauer measurements were performed with a constant acceleration Halder-type spectrometer using a room temperature ^{57}Co source (Rh matrix) in the transmission geometry. The polycrystalline absorbers containing about 10 mg/cm^2 of iron were used to avoid the experimental widening of the peaks. The velocity was calibrated using pure iron metal as the standard material.

At 293 K, a preliminary refinement using Lorentzian profile lines showed that the spectrum consists of two doublets assigned to two sites of Fe^{3+} . Nevertheless, the large values of the line width implied the existence of distributions of quadrupole splitting. Thus, a second calculation has been performed. For that, the value of the half height width was fixed at 0.30 - 0.40 mm/s and the isomer shift values were those determined in the first calculation.

- [1] F.M. Figueiredo, V.V. Kharton, J.C. Waerenborgh, A.P. Viskup, E.N. Naumovich, J.R. Frade, Influence of Microstructure on the Electrical Properties of Iron-Substituted Calcium Titanate Ceramics, *J. Am. Ceram. Soc.* 87 (2004) 2252–2261.
- [2] V.V. Kharton, E.N. Naumovich, A.V. Nikolaev, Materials of high-temperature electrochemical oxygen membranes, *J. Memb. Sci.* 111 (1996) 149–157.
- [3] J. Fouletier, E. Mantel, M. Kleitz, Performance characteristics of conventional oxygen gauges, *Solid State Ionics.* 6 (1982) 1–13.
- [4] J. Fouletier, E. Siebert, A. Caneiro, Accurate monitoring of low oxygen activity in gases with conventional oxygen gauges and pumps, in: *Sci. Technol. Zirconia II*, 1983: p. 618–626.
- [5] Home - NorECs - Norwegian Electro Ceramics AS.
- [6] J. Fouletier, P. Fabry, M. Kleitz, Electrochemical Semipermeability and the Electrode Microsystem in Solid Oxide Electrolyte Cells, *J. Electrochem. Soc.* 123 (1976) 204.
- [7] P.M. Geffroy, a. Vivet, J. Fouletier, N. Richet, P. Del Gallo, T. Chartier, Influence of Oxygen Surface Exchanges on Oxygen Semi-Permeation through $\text{La}_{(1-x)}\text{Sr}_x\text{Fe}_{(1-y)}\text{Ga}_y\text{O}_{3-\delta}$ Dense Membrane, *J. Electrochem. Soc.* 158 (2011) B971.
- [8] M.C. Steil, J. Fouletier, P.-M. Geffroy, Surface exchange polarization vs. gas concentration polarization in permeation through mixed ionic-electronic membranes, *J. Memb. Sci.* 541 (2017) 457–464.
- [9] P.M. Geffroy, A. Vivet, J. Fouletier, C. Steil, E. Blond, N. Richet, P. Del Gallo, T. Chartier, The Impact of Experimental Factors on Oxygen Semi-Permeation Measurements, *J. Electrochem. Soc.* 160 (2013) F60–F68.
- [10] K. Akiba, M. Ueda, K. Kawamura, T. Maruyama, Continuous Monitoring of Oxygen Chemical Potential at the Surface of Growing Oxide Scales during High Temperature Oxidation of Metals, *Mater. Trans.* 49 (2008) 629–636.
- [11] W.G. Schlecht, Calculation of density from X-Ray Data, *Geol. Surv.*
- [12] P. Fabry, M. Kleitz, C. Déportes, Sur l'utilisation d'une Electrode Ponctuelle dans les Cellules à Oxyde Electrolyte Solide I . Application aux Mesures Thermodynamiques et à la Détermination du Nombre de Transport Electronique de l'Electrolyte, *J. Solid State Chem.* (1972) 1–10.
- [13] S. Boulfrad, E. Djurado, J. Fouletier, Electrochemical characterization of nanostructured zirconias, *Solid State Ionics.* 180 (2009) 978–983.
- [14] J.-M. Greneche, A. Wattiaux, La spectroscopie Mössbauer, *Sci. Fr.* (2012).
- [15] G. Filoti, Basic principles of Mossbauer spectroscopy and applications, in: Springer (Ed.), *NMR-MRI, μ SR Moessbauer Spectrosc. Mol. Magnets*, Milano, 2007: p. 227.
- [16] P. Gütlich, *Mössbauer Spectroscopy – Principles and Applications*, University of Mainz, 2005.

CHAPTER 3

CHARACTERIZATION

Presque tout ce qui caractérise l'humanité se résume par le mot culture.

François Jacob (Le Jeu des possibles, 1981)

Table of content

| | |
|------------------------------------|----|
| 1. Introduction..... | 57 |
| 2. Powder characterization | 58 |
| 3. Membrane preparation..... | 62 |
| 4. Porous layer..... | 63 |
| 5. Modified Pechini synthesis..... | 64 |
| Characterization | 65 |
| 6. Conclusion | 69 |

1. Introduction

This chapter presents the main characterizations performed on the CTF powder. Some XRD measurements, thermogravimetric and dilatometric measurements were completed to determine the crystallographic structure and the thermal stability of the CTF.

Information on the membrane preparation and porous layer deposition on some membranes is also given in this chapter.

Then a section is dedicated to the synthesis of CTF powder via modified Pechini methods.

2. Powder characterization

The CTF ($\text{CaTi}_{0.9}\text{Fe}_{0.1}\text{O}_{3-\delta}$) powder was synthesized by Saint-Gobain (CTF-SG) via electrofusion. The chemical composition was determined by X-Ray fluorescence (XRF) with the PANalytical PW2540 VRC (Table 1). We obtain $\text{CaTi}_{0.87}\text{Fe}_{0.10}\text{O}_{3-\delta}$ which is close to the expected stoichiometry $\text{CaTi}_{0.90}\text{Fe}_{0.10}\text{O}_{3-\delta}$ (and in the error margin of the equipment). The powder has an average grain size, D_{50} , of 1.22 μm (HORIBA Laser Scattering Particle Size Distribution Analyzer LA-950).

Table 1: Chemical composition of CTF powders in wt.%.

| | TiO ₂ | CaO | Fe ₂ O ₃ | SiO ₂ | MgO |
|--------|------------------|------|--------------------------------|------------------|-----|
| CTF-SG | 52.2 | 41.8 | 5.71 | <0.05 | 0.1 |

XRD performed as a function of temperature (Figure 1) shows that, at room temperature, the crystal structure of initial CTF powders corresponds to a pseudo-cubic perovskite of the $Pnma$ group space (Figure 2), such as expected given its Goldschmidt tolerance factor $t = 0.97$.

Diffraction peaks were indexed using the CaTiO_3 crystal phase (PDF 00-042-0423) from ICDD 2016 and lattice parameters were calculated via Rietveld refinement using the software HighScore plus.

Table 2: Lattice parameters of initial CTF powder, calculated via Rietveld refinement.

| a (Å) | b (Å) | c (Å) | v (Å ³) |
|--------|--------|--------|---------------------|
| 5.4403 | 7.6413 | 5.3820 | 223.73 |

We calculated a theoretical density of 4.04 g/cm^3 at room temperature.

$$TD = \frac{Z \times M_{CTF}}{N_A \times V} = \frac{4 \times 135.94}{6.022 \times 10^{23} \times 223.73 \times 10^{-24}} = 4.04 \text{ g.cm}^{-3}$$

During heating, the crystal structure becomes increasingly symmetrical, transitioning from orthorhombic to tetragonal ($I4/mcm$) at ≈ 1200 °C, and to cubic ($Pm\bar{3}m$) at ≈ 1300 °C (Figure 2), followed by a 5.5% cell volume expansion. This is shown in Figure 2, with the disappearance of certain reflections while temperature increases. For instance, the peak centered around 36.5 ° is present only in the orthorhombic symmetry and no more present for the tetragonal and cubic symmetry while the pic centered at 38.5 ° corresponds to a triplet in orthorhombic symmetry, only one reflection in the tetragonal symmetry and is no more present in cubic symmetry.

Higher symmetry and larger volume at operation conditions are expected to facilitate oxygen diffusion, as it was demonstrated that the lattice distortion (lattice stress and deviation from cubic symmetry) is one of the most important parameters which influence the ionic conductivity [1].

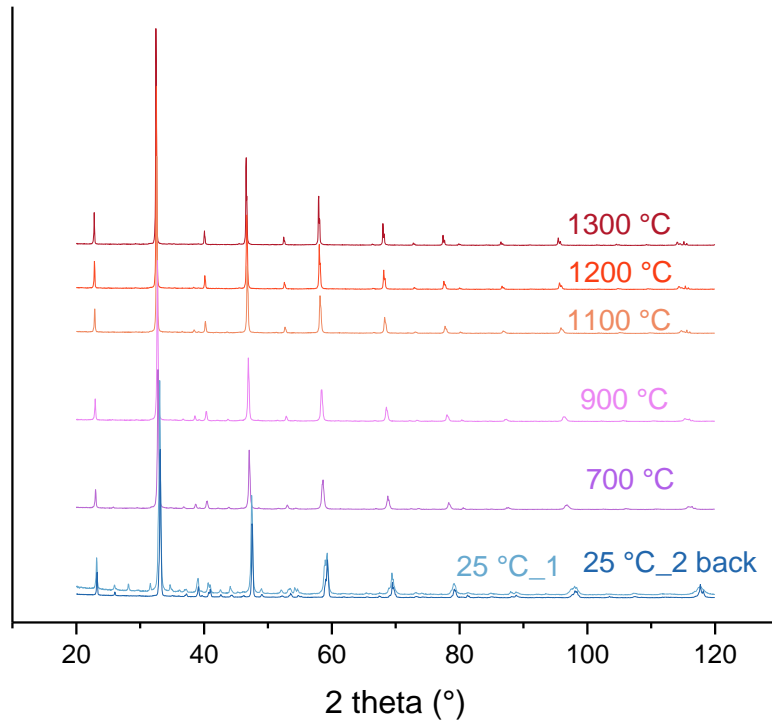


Figure 1: Normalized XRD patterns of the CTF as a function of temperature.

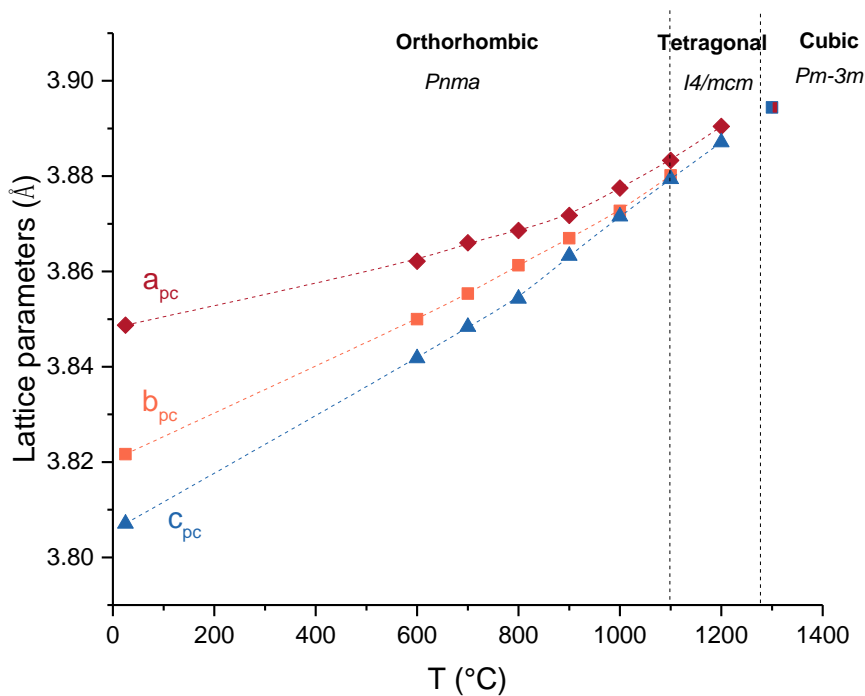


Figure 2: Pseudo cubic lattice parameters as a function of temperature. Lattice parameters of the orthorhombic ($Pnma$) and tetragonal ($I4/mcm$) phases are expressed according to a pseudo cubic lattice to make the comparison easier ($a_{pc}=a/\sqrt{2}$; $b_{pc}=b/2$; $c_{pc}=c/\sqrt{2}$).

At room temperature, peaks corresponding to a minority hydroxide phase ($Ca_3Fe_2TiO_4(OH)_8$) are indexed, but disappear upon heating above 700 °C (Figure 1 and Figure 3). This phase is not found upon cooling down to room temperature. No other significant differences were found after thermal cycling, indicating that the CTF is chemically stable up to 1400 °C (Figure 3).

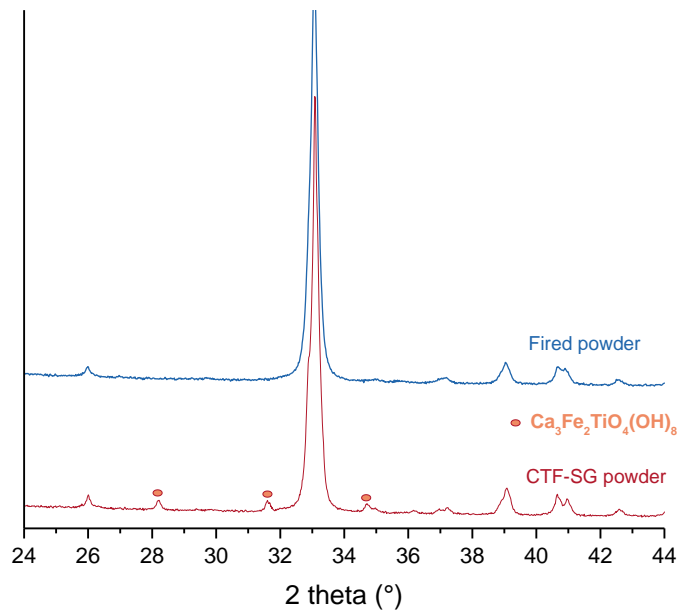


Figure 3: Details of the normalized XRD patterns of the CTF-SG powder before and after calcining at 1400 °C.

Thermogravimetric analyses performed under air on powders between 25 and 1600 °C show an initial loss of above 1.4 wt.% up to 350 °C, followed by a loss of 0.7 wt.% up to 650 °C (Figure 4). This behavior can be likely ascribed to dehydration and hydroxide decomposition (XRD image), respectively. The scan shows no other events during further heating to 1600 °C, or during cooling down to room temperature, indicating that the sample is stable in this temperature range. Therefore, one does not expect major composition or phase changes during sintering of CTF-SG up to 1550 °C.

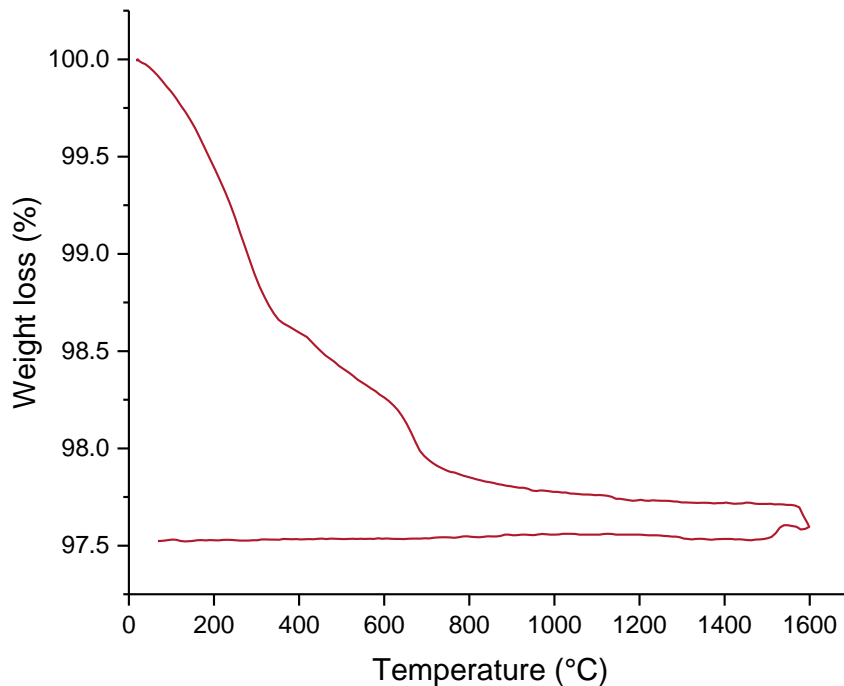


Figure 4: Thermogravimetry curve of initial CTF-SG powder using the STA NETZSCH type STA 409C with a heating rate of 10 °C/min.

Dilatometric measurements performed on powders between 20 and 1450 °C (10 °C/min) show that the sintering begins around 950 °C and a shrinkage of 14% is obtained after cooling to room temperature (Figure 5). We note that the sintering is not finished at 1450 °C, but we stopped at this temperature to avoid any reaction with the equipment.

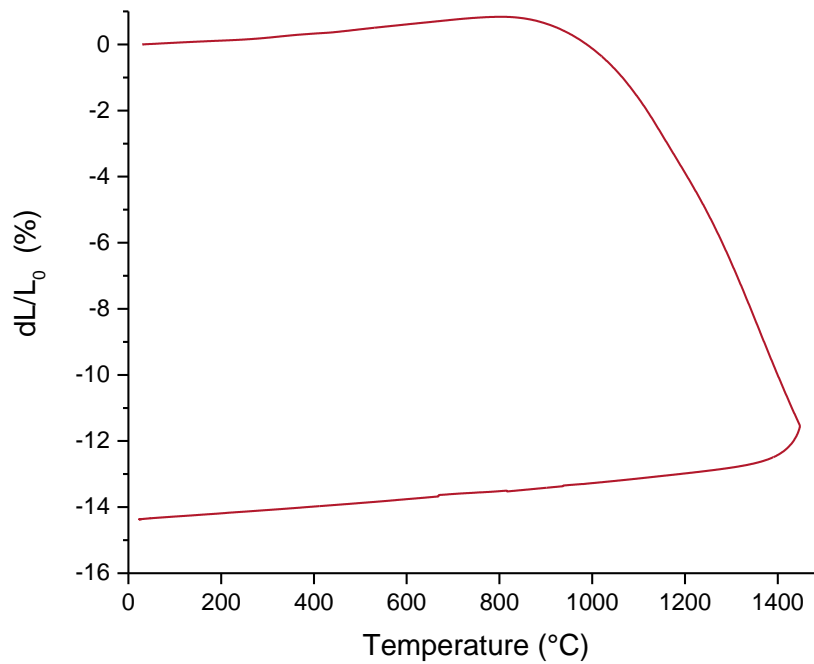


Figure 5: Dilatometer curves of CTF-SG.

For the following experiments, CTF-SG was fired at 1400 °C for 5 h because it was the best firing conditions found in previous studies. The density, determined by Archimedes method after firing, was around 3.98 g/cm³ while the theoretical density of the powder, measured with XRD is around 4.04 g/cm³ which correspond to 98.5% of densification.

3. Membrane preparation

CTF pellets were prepared by slip casting. The slurry was prepared by mixing CTF powder with water and a commercially available dispersant (ProxB03, Synthron). Green bodies were sintered at 1400 °C for 5 h, resulting in a relative density of 96% as measured with Archimedes' immersion method. The sintered pieces were cut into 1.5 mm thick pellets and rectified to a diameter of 19 mm and a thickness of 1.3 mm for semi-permeation on the setup A.



Figure 6: a) Slip casting process. b) Green bodies obtained after slip casting. c) Pellets cuts from the sintered pieces.

Occasionally, green CTF pellet were pressed (first uniaxially and then with an isostatic pressure of 1500 bar) instead of slip casted for a question of pellets size and amount of powder.

4. Porous layer

Experiments were performed on membranes with a porous layer. Porous layers were deposited by screen printing of CTF slurries, with and without cellulose pore formers (Sygmacell, type 20, provided by Sigma-Aldrich), on the lean side of the sintered membranes. The porous layers were fired at 1200 °C for one hour. Microstructure of the membranes and the porous layers were observed in a SEM (Hitachi TM-3030).

SEM images of the microstructure of the different CTF membranes showed a homogeneous grain size (2-3 μm) with little to no porosity visible (Figure 7). The heat treatment of the porous layers resulted in a good contact with the membrane, with no visible gaps along the cross section, while maintaining porosity within the layer. The porous layer without pore formers (b) is highly homogeneous with a thickness of $\approx 15 \mu\text{m}$ and pore size $< 2 \mu\text{m}$. The layer with pore formers (c) is more irregular with thickness ranging between 15 and 25 μm , and larger pores ranging between 2 and 15 μm . The large pore size obtained with the pore formers ensures that the layer will not be limiting for gas diffusion, despite being thicker.

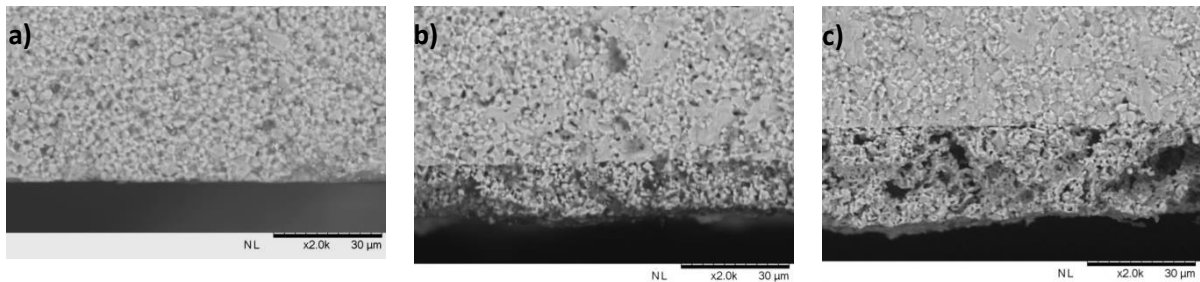


Figure 7: Cross-section SEM images the bare CTF membrane (a), CTF + layer (b) and CTF + layer + pore formers (c).

More detailed pictures of the CTF membrane with the porous layer without pore formers is shown in Figure 8.

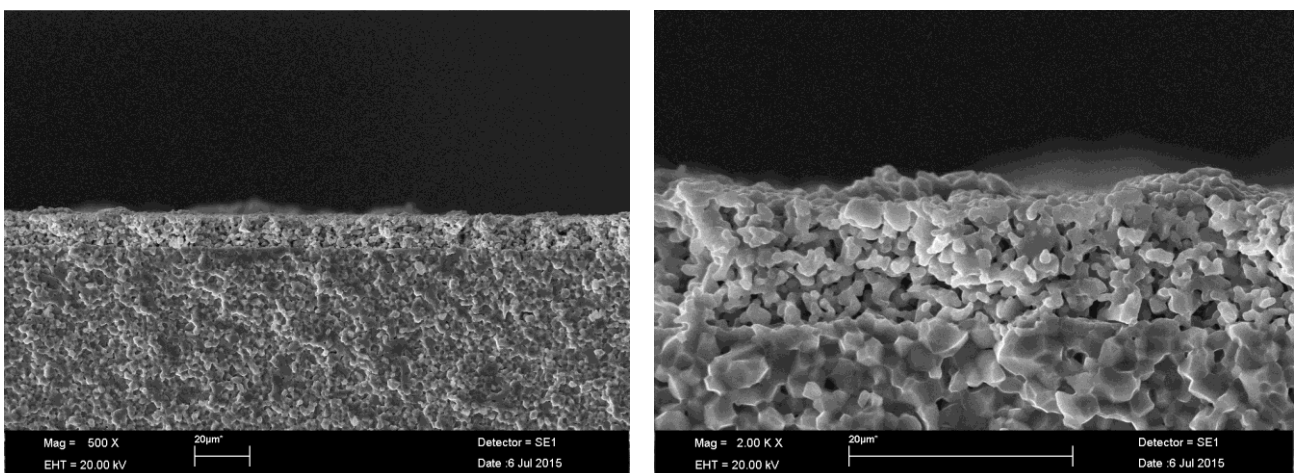


Figure 8: Cross section SEM images of the CTF+ layer membrane

5. Modified Pechini synthesis

CTF powder was also synthesized via a modified Pechini synthesis (referred as CTFsc) to be able to modify the amount of iron. Nitrate salts were used as starting agents, citric acid as a complexing agent and ethylene glycol for polymerization. Calcium and iron salts were dissolved in water and the solution was acidified with citric acid. Then, titanium isopropoxide was added. The nitrate salts and the titanium were mixed in stoichiometric ratios. Citric acid was added in a molar ratio (citric acid/titanium ion ≈ 1.3) in order to decrease the pH lower than 1 to have Fe^{3+} ions and to prevent TiO_2 formation.

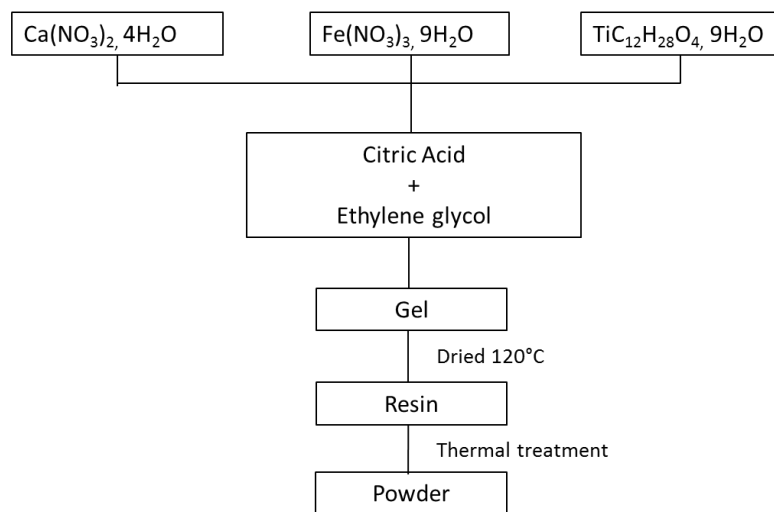


Figure 9: Schematic representation of the Pechini modified synthesis.

The solution was let under stirring overnight. The solution was then heated at 120°C for 1 h and ethylene glycol was added. The gel was heated at 120°C under stirring for 2 h and then put into an oven at 120°C overnight. It results into a polymeric resin which is crushed with a mortar and further calcined at 800°C for 2 h.

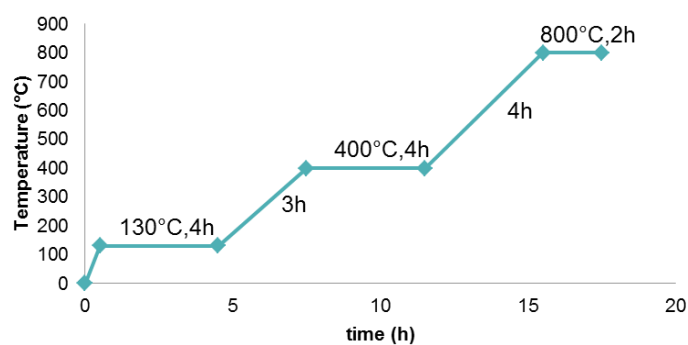


Figure 10: Temperature profile of the calcination of the synthesized powders.

Characterization

The synthesized powder (CTFsc) was compared to the one obtained via electrofusion by Saint-Gobain (CTF-SG). First, the chemical composition was determined by X-Ray fluorescence (XRF) with the PANalytical PW2540 VRC. It shows that the initial powders have roughly the same stoichiometry (Table 3). We obtain $\text{CaTi}_{0.87}\text{Fe}_{0.10}\text{O}_{3.6}$ for CTF-SG and $\text{CaTi}_{0.91}\text{Fe}_{0.10}\text{O}_{3.6}$ for CTFsc which is close to the $\text{CaTi}_{0.90}\text{Fe}_{0.10}\text{O}_{3.6}$ theoretical stoichiometry.

Table 3: Chemical composition of CTF powders in wt.%.

| | TiO ₂ | CaO | Fe ₂ O ₃ | SiO ₂ | MgO | Al ₂ O ₃ |
|--------|------------------|------|--------------------------------|------------------|-----|--------------------------------|
| CTF-SG | 52.2 | 41.8 | 5.71 | < 0.05 | 0.1 | / |
| CTFsc | 52.4 | 40.5 | 5.8 | 0.2 | / | 0.4 |

The crystallite structure and phase composition was determined using XRD. XRD results were indexed using the CaTiO_3 crystal phase (Figure 11). The experimental reflections match with the pure perovskite, in agreement with incorporation of iron into the lattice. The lattice parameters correspond to the orthorhombic symmetry of the *Pnma* group (Table 4). A second set of reflections corresponding to a minority phase were indexed with $\text{Ca}_3\text{Fe}_2\text{TiO}_4(\text{OH})_8$ for CTF-SG (Figure 12) and with calcite (CaCO_3) and rutile (TiO_2) for CTFsc, but they all disappear after firing (Figure 12).

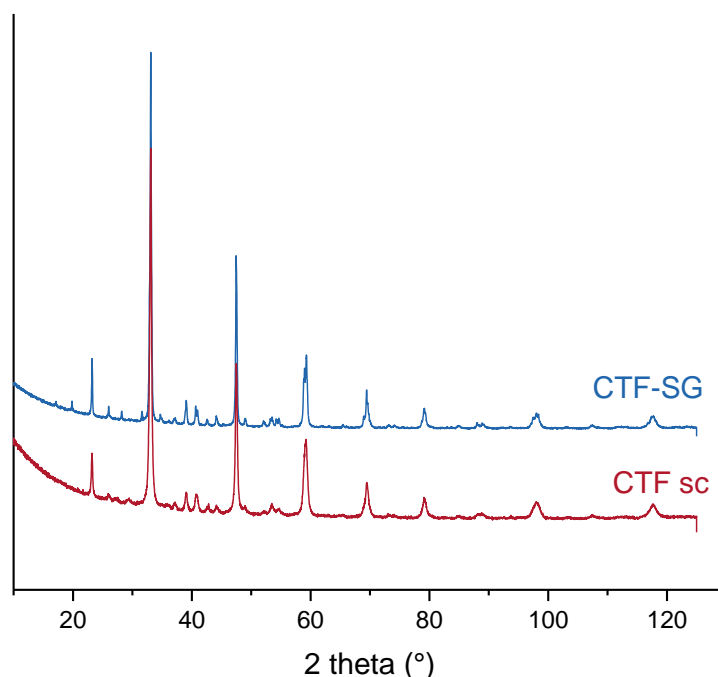


Figure 11: Normalized XRD patterns of the two CTF, collected with the X'Pert de PANalytical diffractometer using procedure Q-PRO-STR-08-30 with a 0.017 ° step and 100 s/step rate.

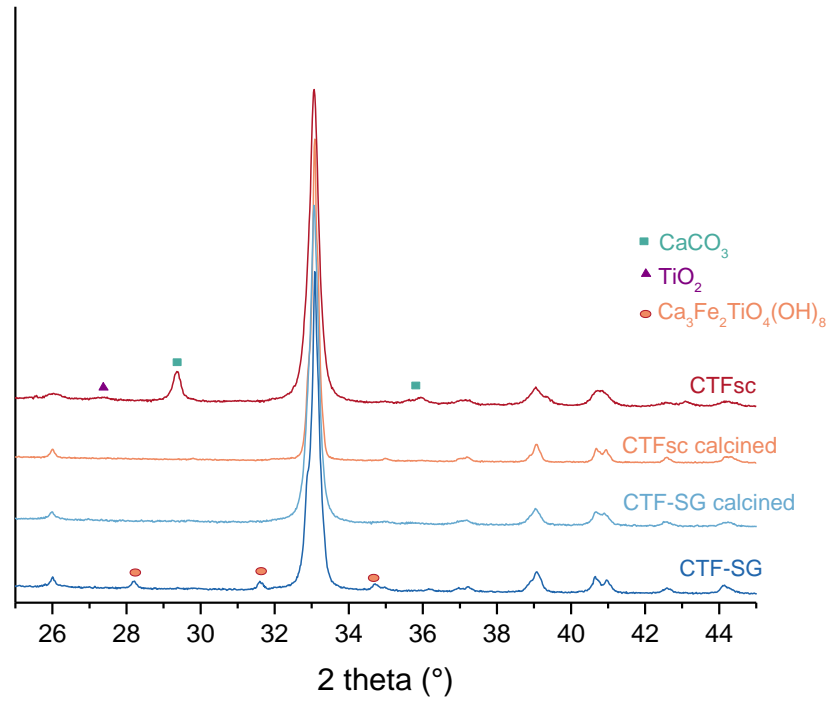


Figure 12: Details of the normalized XRD patterns of the CTF-SG and CTFsc before and after calcination at 1400 and 1300 °C respectively.

The calculated theoretical density is, as expected, the same for both powders (Table 4).

Table 4: Lattice parameters of CTF powders, calculated via Rietveld refinement.

| Sample | a (Å) | b (Å) | c (Å) | v (Å ³) | Theoretical density (g.cm ⁻³) |
|--------|--------|--------|--------|---------------------|---|
| CTF-SG | 5.4403 | 7.6413 | 5.3820 | 223.73 | 4.04 |
| CTFsc | 5.4343 | 7.6328 | 5.3832 | 223.29 | 4.05 |

Dilatometric measurements performed on the two powders between 20 and 1450 °C are plotted in Figure 5.

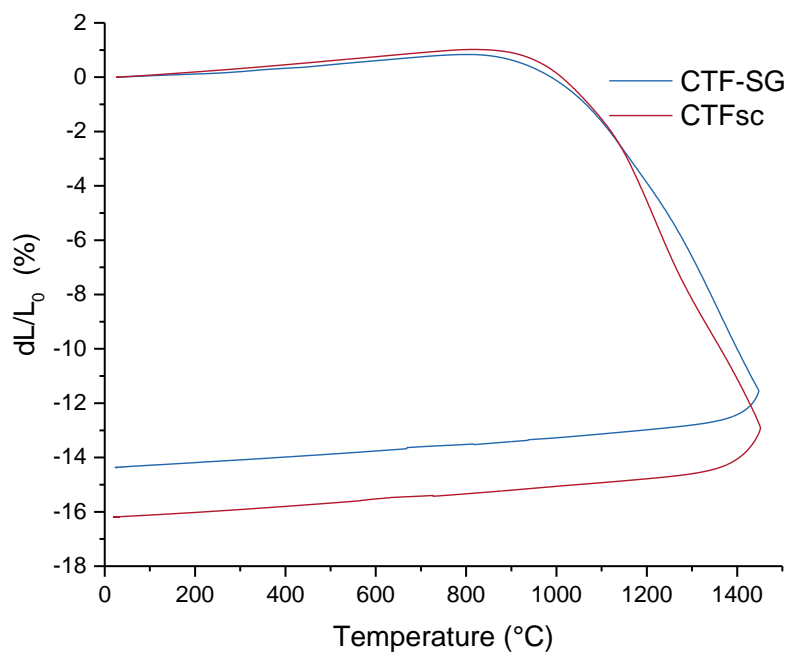


Figure 13: Dilatometer curves of CTFs.

CTFsc shows a shrinkage of about 16% while CTF-SG about 14%. For both powders, the shrinkage starts after 900 °C. However, the green density is considerably lower for CTFsc than for CTF-SG (47% vs 62%). Consequently, the density, determined by Archimedes method after firing, was around 2.72 g/cm³ for CTFsc and 3.98 g/cm³ for CTF-SG. The densification of the CTFsc is thus very low (67%) (cf. Table 4 for the theoretical density).

SEM analyses (Figure 14) and particle size measurements (Figure 15) were carried out to understand the difference in density.

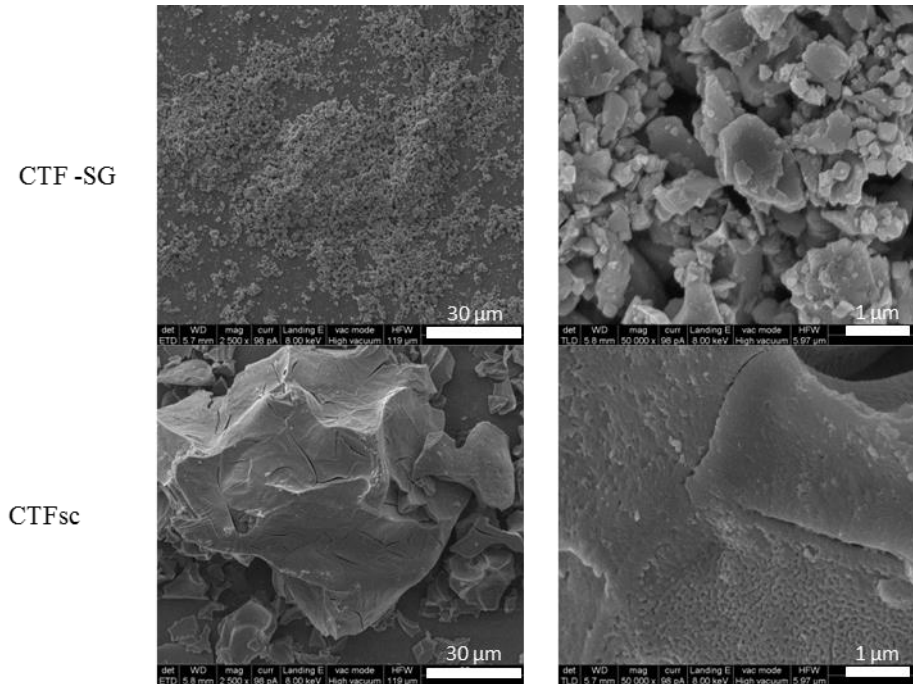


Figure 14: SEM pictures of CTF-SG and CTFsc.

SEM pictures show that both powders have a different size order. CTF-SG shows particles around 1 μm diameter while CTFsc has 30 μm large particles. This was confirmed by laser particle size measurements (Figure 15) where the D₅₀ of CTF-SG is 1.2 μm while D₅₀ of CTFsc is 17.2 μm.

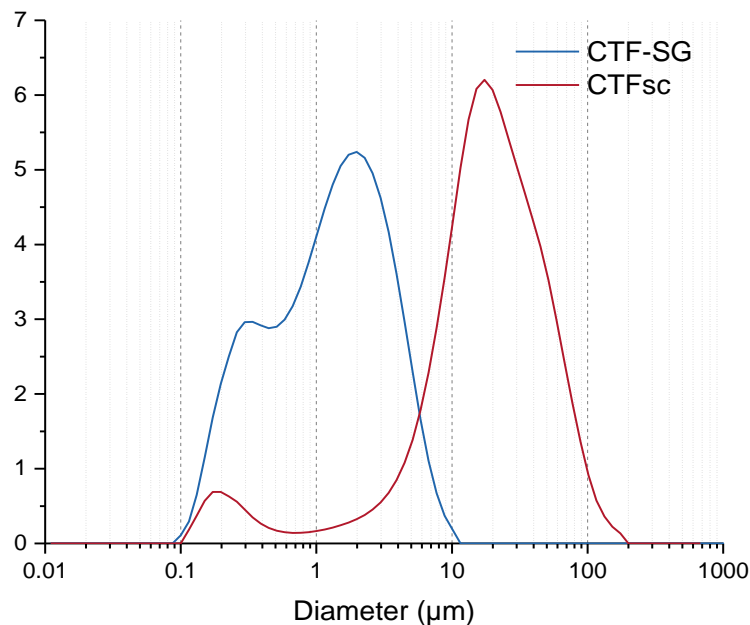


Figure 15: Particle size measurement of CTF-SG powder and CTFsc powder.

We can see that the synthesized powder has a higher particle size and very large agglomerate compared to CTF-SG. This could be responsible for the low green density of the CTFsc powder and the difficulty to sinter it. Wet milling was then carried out.

Milling was performed on the CTFsc powder. The powder was dissolved in ethanol to obtain a slurry of 70 volume percent fraction of ethanol. The slurry was wet milled 24 h with big and medium balls (9.7 mm and 5.7 mm diameter, 50 wt.% of the slurry for each of them) and 48 h with small balls (2.3 mm in diameter and same weight as the slurry) (powder is denoted as CTFsc mil). Particle size measurements were carried out on the powder after the milling to ensure its efficiency. Results are plotted in Figure 16.

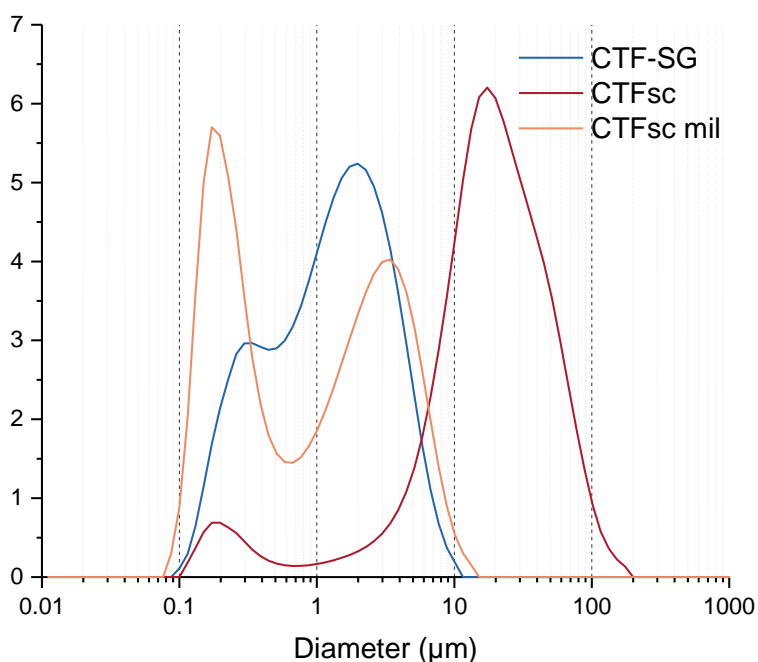


Figure 16: Particle size measurement of CTF powders.

Milling enables to decrease very much the particle size of the synthesized powder. Indeed, for CTFsc mil, the distribution is bimodal, with peaks around 0.3 and 3 µm. The D_{50} before milling was above 15 µm and it is lower than 1 µm (0.84 µm) after milling. We also succeed to have even smaller particle than CTF-SG ($D_{50} = 1.2$ µm).

The crystallite structure and phase composition remain the same after milling and this enables to obtain dense pellets, after firing the powder at 1300 °C for 5 h (densification higher than 95%).

Synthesis of 20% iron doped calcium titanate was also done successfully.

6. Conclusion

CTF powder was analyzed and it results that the stoichiometry was really close to the one expected. The crystallographic information was concordant with literature and the symmetry of the crystal increases with temperature which is expected to facilitate oxygen diffusion.

The powder was stable in temperature and we succeed to make dense membranes.

Porous layers were successfully deposited by screen printing and two different inks were used to modify the pore size distribution.

Finally, powder was synthetized by Pechini modified method. The powder was characterized and after milling steps, we succeed to obtain dense membranes of 10 and 20% iron doped calcium titanate.

- [1] M. Mogensen, D. Lybye, N. Bonanos, P.V. Hendriksen, F.W. Poulsen, Factors controlling the oxide ion conductivity of fluorite and perovskite structured oxides, *Solid State Ionics*. 174 (2004) 279–286.
- [2] V.V. Kharton, F.M. Figueiredo, A.V. Kovalevsky, A.P. Viskup, E.N. Naumovich, J.R. Jurado, J.R. Frade, Oxygen Diffusion in, and Thermal Expansion of, SrTiO_{3-δ}-and CaTiO_{3-δ}-Based Materials, *Defect Diffus. Forum*. 186–187 (2000) 119–136.
- [3] L.W. Tai, M.M. Nasrallah, H.U. Anderson, D.M. Sparlin, S.R. Sehlin, Structure and electrical properties of La_{1-x}Sr_xCo_{1-y}Fe_yO₃. Part 1. The system La_{0.8}Sr_{0.2}Co_{1-y}Fe_yO₃, *Solid State Ionics*. 76 (1995) 259–271.
- [4] H. Tuller, S. Bishop, Point defects in oxides: tailoring materials through defect engineering, *Annu. Rev. Mater. Res.* 41 (2011) 369–398.
- [5] A.A. Murashkina, A.N. Demina, A.K. Demin, V.I. Maragou, P.E. Tsiakaras, The influence of Fe, Cu, Al - doping on the crystal structure, thermal and electrical properties of calcium titanate, *Solid State Ionics*. 179 (2008) 1615–1619.
- [6] F.M. Figueiredo, M.R. Soares, V.V. Kharton, E.N. Naumovich, J.C. Waerenborgh, J.R. Frade, Properties of CaTi_{1-x}Fe_xO_{3-δ} Ceramic Membranes, *J. Electroceramics*. 13 (2004) 627–636.
- [7] C. Chatzichristodoulou, C. Schönbeck, A. Hagen, P.V. Hendriksen, Defect chemistry, thermomechanical and transport properties of (RE_{2-x}Sr_x)_{0.98}(Fe_{0.8}Co_{0.2})_{1-y}Mg_yO_{4-δ} (RE=La, Pr), *Solid State Ionics*. 232 (2013) 68–79.
- [8] H. Ullmann, N. Trofimenko, F. Tietz, D. Stöver, A. Ahmad-Khanlou, Correlation between thermal expansion and oxide ion transport in mixed conducting perovskite-type oxides for SOFC cathodes, *Solid State Ionics*. 138 (2000) 79–90.
- [9] G. Pfaff, Synthesis of Calcium Titanate Powders by the Sol-Gel Process, *System*. (1994) 58–62.

CHAPTER 4

CTF

SEMI-PERMEATION

Notre seule vraie famille est celle des livres. On y éprouve un sentiment de perméabilité avec celui qui raconte : il donne tant de force, tant de frissons.

J.M.G. Le Clézio (extrait de *Télérama*, décembre 2000)

Table of content

| | | |
|-----|--|----|
| 1. | Introduction..... | 73 |
| 2. | Oxygen permeation measurements..... | 74 |
| 3. | Identifying the limiting step | 76 |
| 3.1 | Critical thickness obtained by isotopic exchange..... | 76 |
| 3.2 | B_c number obtained with electrochemical probes..... | 77 |
| 3.3 | Effect of a porous layers on the limiting steps | 79 |
| 4. | Oxygen transport mechanisms within the bulk..... | 83 |
| 5. | Surface polarization study | 85 |
| 6. | Conclusion | 87 |

1. Introduction

This chapter will focus on the characterization of the O₂ semi-permeation of CTF membranes under different oxygen partial pressure gradients and temperatures. To determine whether the oxygen transport process is limited by the surface exchange or by bulk diffusion different experiments were performed. The results obtained with the specific setup presented in chapter 2 will be compared with isotopic exchange measurements. Moreover, experiments on a surface modified pellet will also be presented and the critical thickness will be discussed.

The role of the surface polarization will be studied in more detail, including transient measurements.

Oxygen diffusion was also analyzed, independently of the surface reaction and the bulk diffusion limitation were studied. This will lead to question on the defect chemistry of the CTF.

2. Oxygen permeation measurements

The oxygen semi-permeability through a CTF membrane was measured as a function of temperature by using air on the oxygen-rich side and argon as sweep gas (Figure 1).

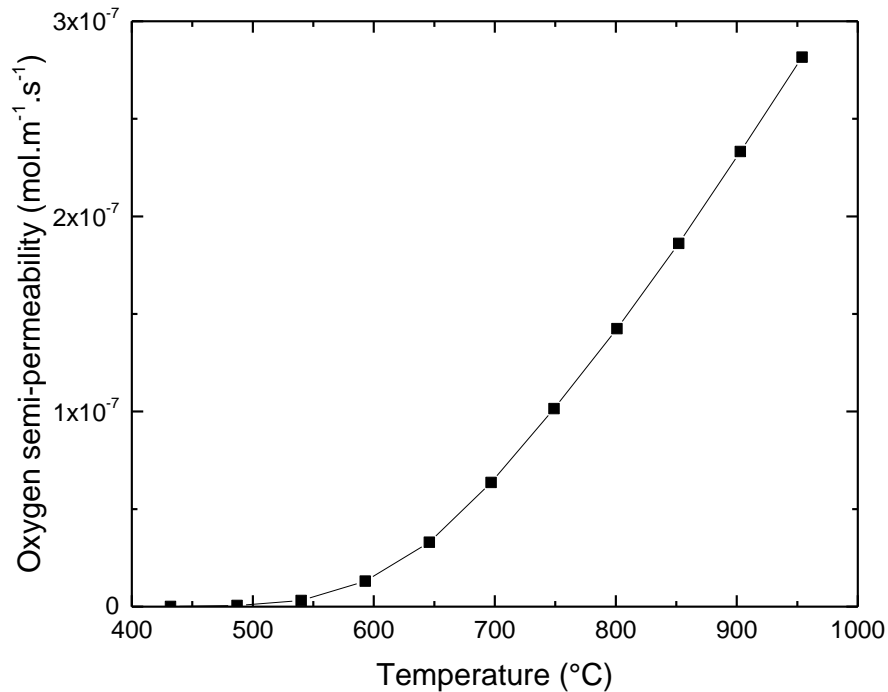


Figure 1: Oxygen semi-permeability as a function of temperature, using air and argon as feed and sweeping gases, respectively. CTF membrane was 1.3 mm thick.

Oxygen permeation can be measured at $T \geq 550$ °C and increases exponentially with temperature, as expected.

The difference of oxygen partial pressure between the two sides of the membrane is a key parameter for the oxygen diffusion (cf. chapter 1 §2). Consequently, different oxygen partial pressures were used on the oxygen-rich side to investigate the whole range of the membrane performances. For this purpose, different mixtures of oxygen, air, and nitrogen were used as oxygen-rich gas.

Figure 2 shows the oxygen semi-permeability as a function of the oxygen partial pressure of the oxygen-rich side at different temperatures. Literature values for CTF doped with 15% Fe were also added for comparison [1].

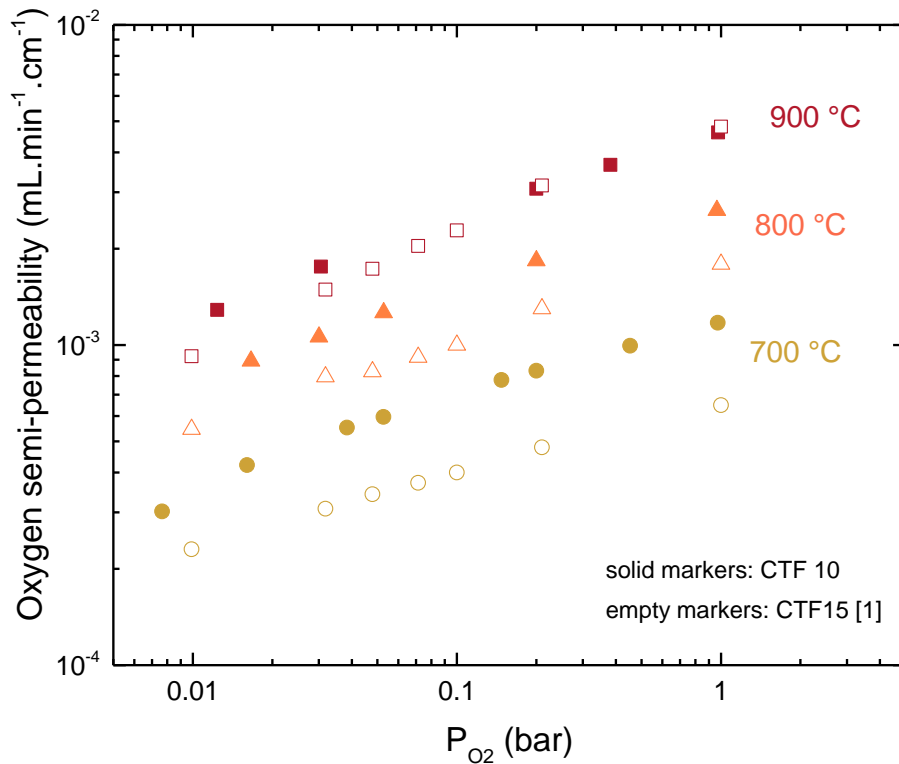


Figure 2: Oxygen semi-permeability as a function of P_{O_2} on the oxygen-rich side (P_3) at 700 °C, 800 °C, and 900 °C, for CTF10 used in this study and CTF15 from literature [1].

CTF10 used in this study has a higher oxygen semi-permeability than the literature values, although this difference decreases with increasing temperature.

One would expect CTF with 15% Fe [1] to have a higher flux than CTF with 10% Fe, due to higher ambipolar conductivity (Chapter 1, § 3.3) [2–4]. It is possible that the lower performance of the CTF15 is related with degradation observed after 18 h of testing [1], which was not the case in this study.

The highest value, obtained at 900 °C, was around 5×10^{-3} mL.min⁻¹.cm⁻¹ which is low regarding the flux defines to be economically viable for this thickness: 0.65-1.3 mL.min⁻¹.cm⁻¹. To improve performance, it is important to determine whether the oxygen transport process is limited by the surface exchange or by bulk diffusion.

3. Identifying the limiting step

3.1 Critical thickness obtained by isotopic exchange

Isotopic exchange was performed, in Bordeaux by Jean-Marc BASSAT, on CTF pellets (Figure 3 and Figure 4) to determine the surface exchange coefficient k and the oxygen diffusion coefficient D^* (Table 1). ^{18}O diffusion profile was recorded on both sides and an average value of k and D^* was calculated using Crank relation (cf. chapter 2 §3). The critical thickness (cf. chapter 1, § 2.1.3) was also estimated.

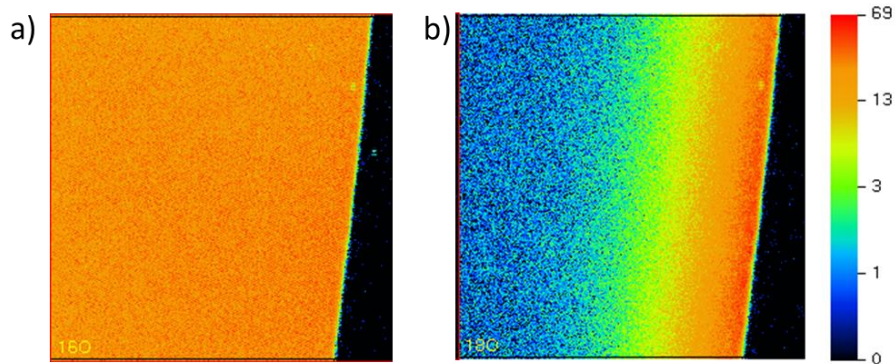


Figure 3: a) ^{16}O and b) ^{18}O diffusion profiles within a CTF pellet observed via SIMS.

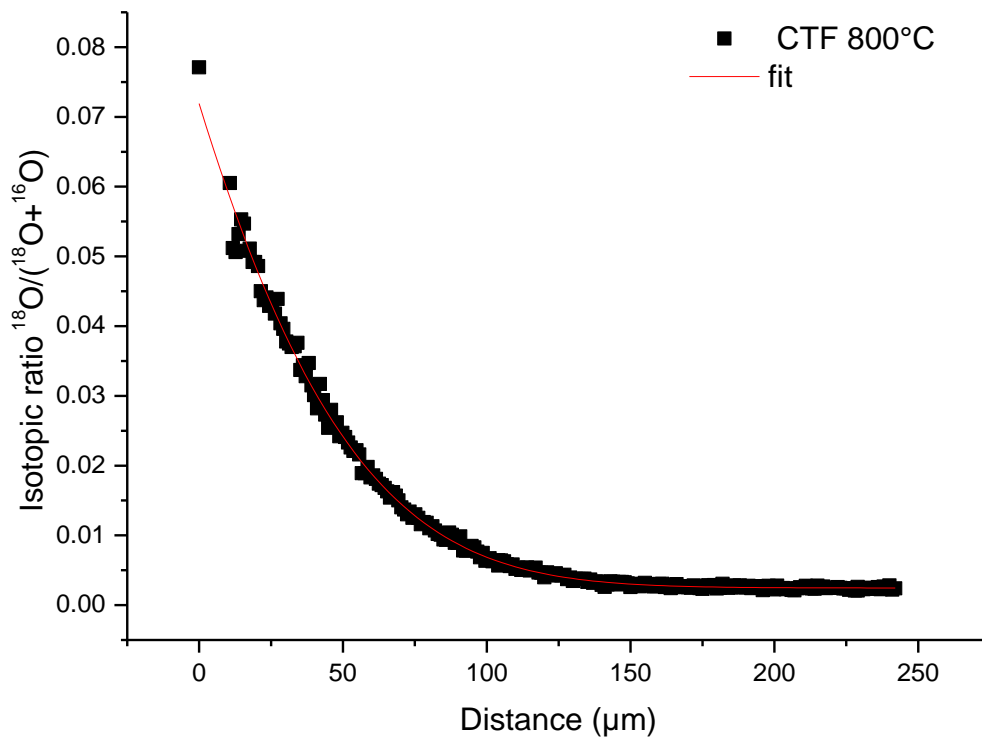


Figure 4: ^{18}O penetration profile (obtained via SIMS) at 800 °C on one side of a CTF pellet.

Table 1: Oxygen diffusion and surface exchange coefficients obtained via isotopic exchange.

| T (°C) | D^* (cm ² .s ⁻¹) | | k^* (cm.s ⁻¹) | | L_c (mm) |
|--------|---|------------------------|-----------------------------|------------------------|------------|
| | Average | Error | Average | Error | |
| 700 | 6.7×10^{-9} | $\pm 1 \times 10^{-9}$ | 1.2×10^{-8} | $\pm 1 \times 10^{-9}$ | 5.6 |
| 800 | 1.7×10^{-8} | $\pm 1 \times 10^{-9}$ | 2.1×10^{-7} | $\pm 4 \times 10^{-8}$ | 0.81 |
| 900 | 3.8×10^{-8} | $\pm 5 \times 10^{-9}$ | 7.9×10^{-7} | $\pm 2 \times 10^{-7}$ | 0.48 |

Critical thickness L_c decreases with increasing temperature, indicating that the surface exchange reaction prevails at lower temperatures. For a pellet with a thickness, $L = 1.3$ mm such as used in this study, $L_c > L$ at 700 °C (Figure 5) so the membrane is expected to be limited by the surface exchange reactions. Conversely, at 800 °C and 900 °C, $L_c < L$, (Figure 5) bulk diffusion is expected to be rate-limiting. However, the thickness of the membrane is in the range $0.1 L_c - 10 L_c$ for all the temperatures, indicating a mixed limitation [5,6].

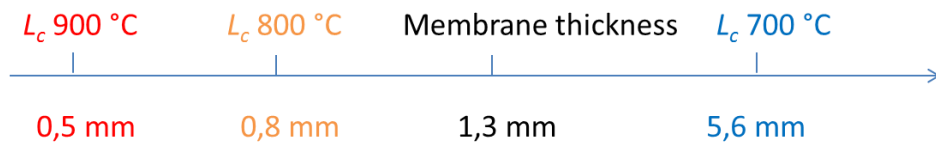


Figure 5: Schematic representation of the thicknesses.

3.2 B_c number obtained with electrochemical probes

Through the specific set-up A, it is possible to separate the influence of the bulk diffusion (a driving force proportional to the oxygen partial pressure gradient across the bulk between P_3 , the oxygen partial pressure on the oxygen-rich side, and P_2^* , the oxygen partial pressure on the surface on the lean side) from the influence of surface exchange reactions (a driving force proportional to the oxygen pressure gradient between P_2^* and P_2 , the oxygen partial pressure on the lean side) (Figure 6).

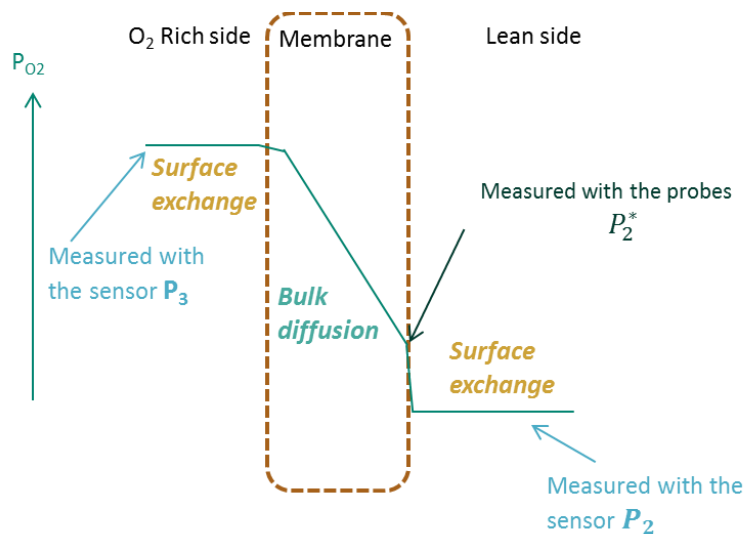


Figure 6: Schematic representation of the oxygen partial pressures measured with the setup with the electrochemical probes.

The limiting step on the lean side can be inferred from the ratio between the chemical potential drop of oxygen near the surface and across the bulk, referred to as B_c^{lean} [7,8]:

$$B_c^{lean} = \frac{(\Delta\mu_{O_2}^{surface})_{lean}}{\Delta\mu_{O_2}^{bulk}} \quad \text{Equation 1}$$

where $(\Delta\mu_{O_2}^{surface})_{lean} = RT \ln \frac{P_2^*}{P_2}$ and $\Delta\mu_{O_2}^{bulk} = RT \ln \frac{P_3}{P_2^*}$ [9]

The value of B_c can be used to identify the rate-limiting step for the oxygen transport across the membrane (Table 2). It is thus possible to differentiate the oxygen surface exchange reaction from the oxygen bulk diffusion.

Table 2: Correspondence between B_c values and rate-limiting step.

| B_c | Rate-limiting step |
|-------------------|---|
| < 0.5 | Oxygen bulk diffusion |
| $0.5 < B_c < 1.5$ | Oxygen bulk diffusion and surface exchange reactions (mixed regime) |
| > 1.5 | Surface exchange reactions |

Oxygen bulk diffusion is the rate-limiting step for the specific oxygen permeability with $B_c < 0.5$, whereas if $B_c > 1.5$, it is controlled by the surface exchange reactions. If $0.5 < B_c < 1.5$, the regime is considered mixed-limited, i.e. limited by both the surface exchange reaction and the oxygen bulk diffusion.

The values presented in this work are measured in the lean side then B_c corresponds to B_c^{lean} but will be written B_c for a question of legibility. B_c decreases from 600 °C to 800 °C and seems to stabilize to a minimum value around 0.25 (Figure 7). Below 750 °C, B_c remains between 1.5 and 0.5 meaning that the oxygen semi-permeability is limited by both surface exchange reactions and by oxygen bulk diffusion. At high temperature, the surface limitation becomes less important and the semi-permeation process is mainly limited by the oxygen bulk diffusion.

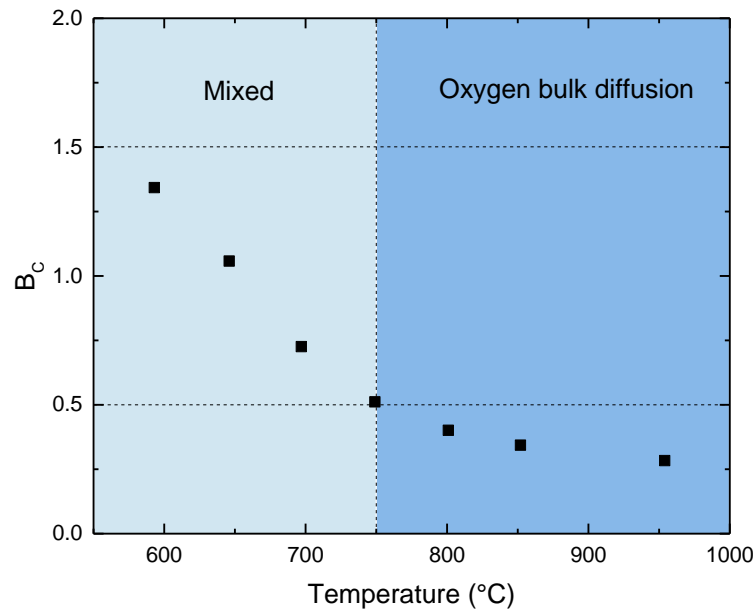


Figure 7: B_c as a function of temperature for a 1.3 mm thick membrane.

Results are then slightly different from those obtained via isotopic exchange. Even if for both methods, the process is limited by oxygen bulk diffusion when temperature increases, the material appears mainly limited by oxygen bulk diffusion at temperature higher than 800 °C while it was considered mixed limited with isotopic exchange measurements.

It is interesting to note that, if the gradient of oxygen partial pressure is low, the limitation in both surfaces is roughly the same and then we can assume that L_C is the same on both sides. In this case, the L_C value can be expressed as followed:

$$L_C = \frac{t_{el} t_{ion} \sigma_{tot} \times RT}{4F^2 k C_O} \quad \text{Equation 2}$$

Then assuming that there is no charge accumulation, the flux can be expressed as followed [10]:

$$j_{O_2} = \frac{t_{el} t_{ion} \sigma_{tot}}{4^2 F^2 L} \Delta \mu_{O_2}^{bulk} = \frac{k s C_O}{RT} \Delta \mu_{O_2}^{surface} \quad \text{Equation 3}$$

Using Equation 2 and Equation 3, it appears that

$$B_C = \frac{L_C}{L} \quad \text{Equation 4}$$

Table 3 compares the ratio L_C/L with the B_C value.

Table 3: Comparison between the ratio L_C/L obtained by isotopic exchange and the B_C number obtained with the electrochemical probes used in oxygen semi-permeation experiment.

| Temperature (°C) | L_C/L (from isotopic exchange) | B_C (from permeation) |
|------------------|----------------------------------|-------------------------|
| 700 | 4.3 | 0.73 |
| 800 | 0.61 | 0.40 |
| 900 | 0.38 | ≈0.30 (estimated) |

These differences can be explained by different experimental conditions. Indeed, in isotopic exchange, a global trend is given, without any oxygen chemical potential difference between the surfaces of the membrane while B_C is calculated on one side of the pellet. In isotopic exchange, the characteristic parameters are calculated under air while, to determine B_C^{lean} , the surface is under an oxygen partial pressure around 10^{-5} bar while the rich side is under air. It is thus not relevant to compare these values. At high temperature, the values are closer, because there is less impact of the surface exchange on the limitation of the whole process.

3.3 Effect of a porous layers on the limiting steps

A porous layer was added on a surface of a CTF membrane to study the effect of an increase of the surface area on the lean side. Two types of layer were used (cf. chapter 3 §4), one without and one with pore formers to obtain two different porosities. They will be referred to as “bare CTF” for the pellet without porous layer, “CTF + layer” for the pellet with a porous layer without pore formers and “CTF + layer + pore formers” for the pellet with a porous layer with pore formers.

Oxygen semi-permeability results are plotted as a function of temperature for all samples (Figure 8).

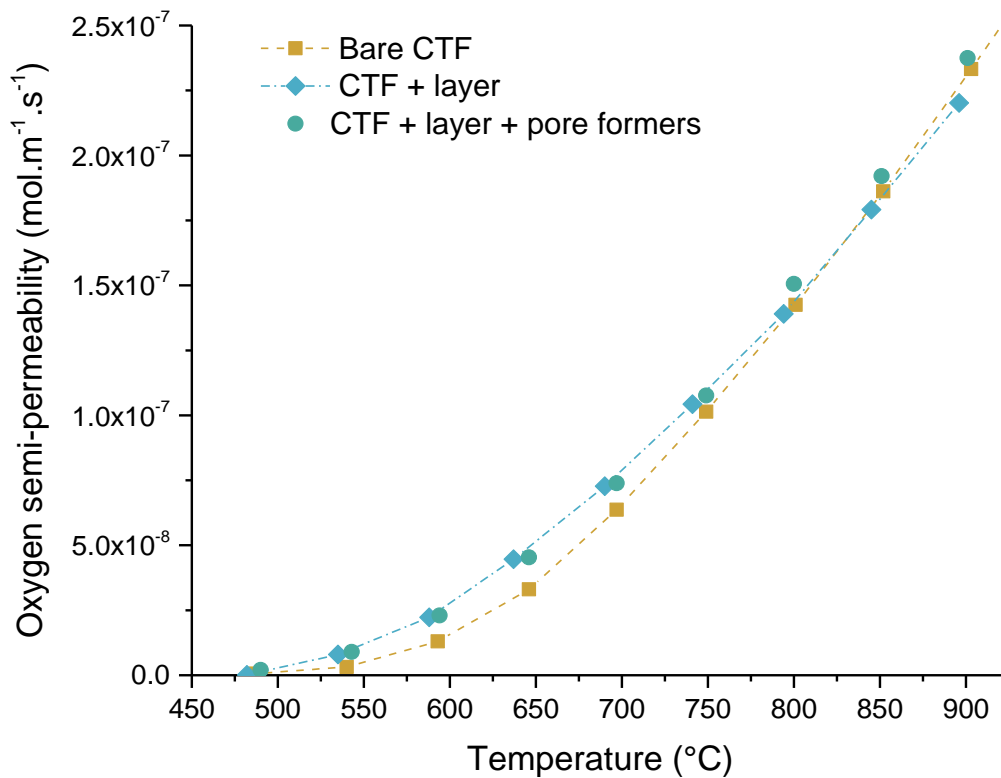


Figure 8: Oxygen semi-permeability as a function of temperature for a bare CTF ($e = 1.28$ mm), a pellet with a CTF porous layer ($e = 1.35$ mm) and another one with a CTF layer with pore formers ($e = 1.30$ mm).

As shown in Figure 8, membranes with porous layers exhibit higher permeation below 750 °C. The ratio of the oxygen flux with versus without porous layer, was 1.71 at 600 °C and 1.13 at 700 °C. This difference is attenuated with increasing temperature and above 800 °C, it becomes insignificant. This confirms the previous results, showing that the performances of the bare CTF membrane was limited both by surface exchange reaction and oxygen bulk diffusion at temperature below 750 °C but mainly limited by bulk diffusion at temperature higher than 800 °C. However, the increased porosity in the layer using pore formers does not further increase the oxygen flux, compared to the layer without pore formers.

The B_c values are also plotted as a function of temperature (Figure 9) to assess the limiting step for oxygen transport.

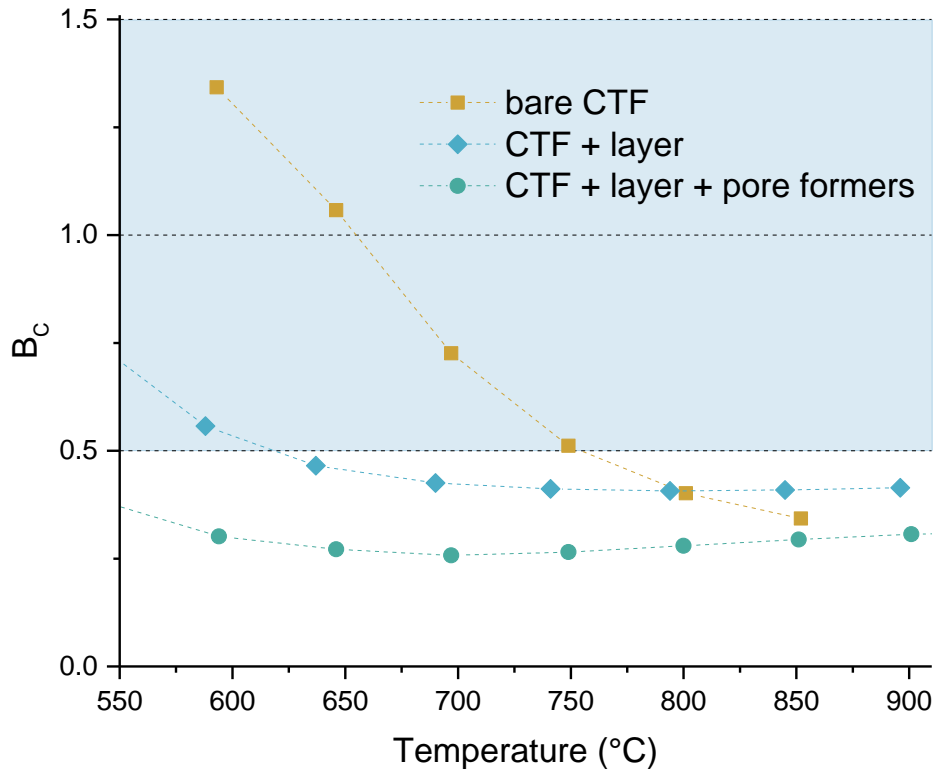


Figure 9: B_c as a function of temperature for a bare CTF (squares), a pellet with a CTF layer (diamonds) and one with a CTF layer with pore formers (circles).

For the bare membrane, B_c values vary from 1.06 to 0.35 over the investigated temperature range, while it is practically constant for both pellets with additional layer. These results show that the oxygen transport in bare CTF membrane is co-limited by surface exchange reactions and oxygen bulk diffusion below 700 °C, transitioning to a diffusion limitation above 750 °C (Table 2). However, for the membranes with a porous layer, the oxygen fluxes are mainly limited by bulk diffusion at each temperature. These results confirm that the layers prevent the limitation due to surface exchange at low temperature. The addition of pore formers slightly decreases B_c , indicating an improvement of the surface exchange, but with no significant changes on the oxygen flux because the permeation is mostly limited by the oxygen diffusion.

Isotopic exchange was performed on the CTF pellet with a porous layer. Measurements were recorded on both sides to observe the impact of the porous layer (Table 4).

Table 4: Oxygen diffusion and surface exchange coefficients obtained via isotopic exchange.

| T (°C) | D^* ($\text{cm}^2.\text{s}^{-1}$) | | k^* ($\text{cm}.\text{s}^{-1}$) | | L_c (mm) | |
|--------|---------------------------------------|----------------------|-------------------------------------|----------------------|---------------|------------|
| | Without layer | With layer | Without layer | With layer | Without layer | With layer |
| 600 | - | 2.6×10^{-9} | - | 1.5×10^{-7} | - | 0.17 |
| 800 | 1.1×10^{-8} | 2.4×10^{-8} | 2.0×10^{-7} | 2.8×10^{-6} | 0.55 | 0.086 |

At 600 °C, the measurement on the side without layer is not exploitable because there is not enough oxygen which diffuses within the material to fit the diffusion profile with the Crank relation. However, with the porous layer, the amount of oxygen which diffuses is more important and it is possible to determine the oxygen diffusion and surface exchange coefficients. This can be explained by the fact that at 600 °C, CTF is limited by the surface exchange reaction and that the porous layer improves the surface exchange. At 800 °C, as expected, the surface exchange reactions coefficient is higher with the porous layer and the oxygen

diffusion coefficient is equal to the one without layer. ^{18}O penetration profile are plotted in Figure 10. With the porous layer, the pellet is then no more limited by the surface exchange.

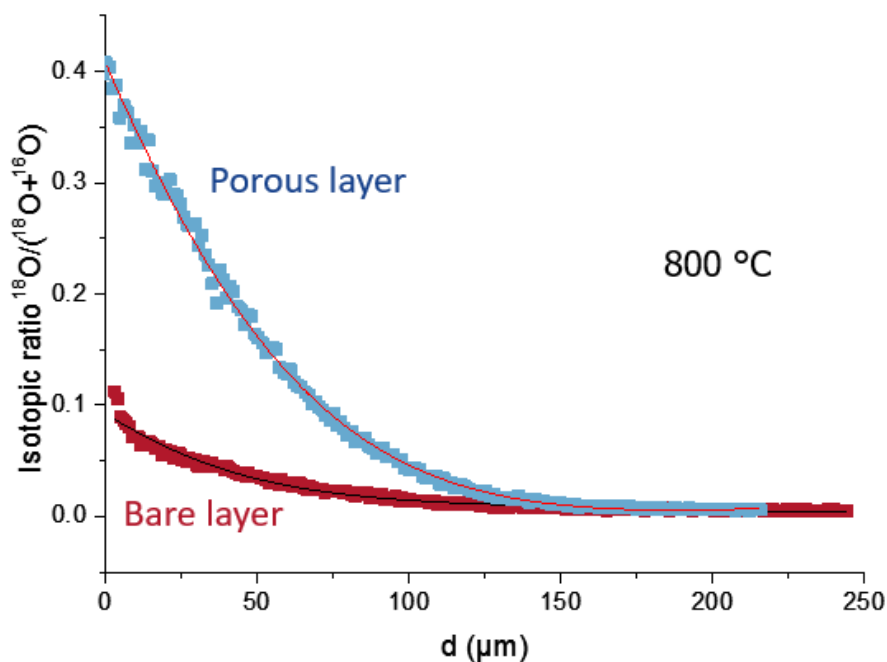


Figure 10: ^{18}O penetration profile (obtained via SIMS) at 800 °C on a side with a porous layer (in blue) and on the side without the porous layer (bar membrane in red) of a CTF pellet.

The values obtained for the side without the porous layer are consistent with the one on the bare membrane presented previously (Table 1). The L_c value obtained at 800 °C is lower than without the porous layer and L_c values decrease with temperature increases as expected.

For the membrane tested in semi-permeation, its thickness is higher than the L_c (more than 10 times higher at 800 °C and 8 times higher at 600 °C) so the membrane is mainly limited by bulk diffusion, confirming results obtained with the set-up A.

Addition of a porous layer on the lean side on the membrane seems then to be sufficient to prevent the surface reactions limitation of a pellets with a 1.3 mm thickness. To optimize the performance of the membrane it is then interesting to study the bulk properties of the CTF membrane.

4. Oxygen transport mechanisms within the bulk

To investigate the bulk limitations resulting from partial conductivities, the surface impact must be excluded by using the oxygen activity on the membrane surface, referred to as P_2^* (cf. Chapter 2).

By using P_2^* , Wagner's theory (Chapter 1) can be applied, taking into account only bulk diffusion limitation. However, depending on the predominant charge carrier, several equations can be applied (Equation 5 if limited by the ionic conductivity and Equation 6 if limited by the electronic conductivity). Equation 5 is obtained, assuming that ionic conductivity is generally constant over a large range of P_{O_2} .

$$J_{O_2} = \frac{RT\sigma_i}{4^2F^2} \ln\left(\frac{P_3}{P_2^*}\right) \quad \text{Equation 5}$$

$$J_{O_2} = \frac{RT\sigma_h^0}{4F^2} (P_3^{1/4} - P_2^{*1/4}) \quad \text{Equation 6}$$

To characterize the limitation that results from either ionic or electron hole conductivity, Figure 11 plots J_{O_2} as a function of $\ln(P_3 / P_2^*)$ and Figure 12 plots J_{O_2} as a function of $(P_3^{1/4} - P_2^{*1/4})$.

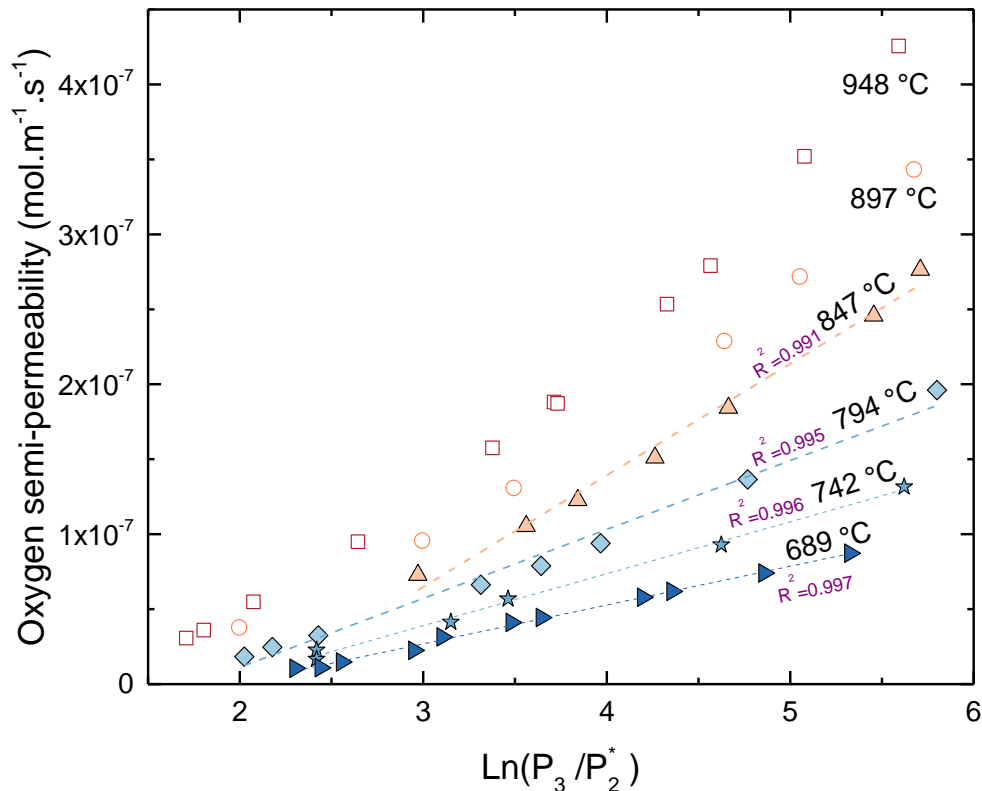


Figure 11: J_{O_2} as a function of $\ln(P_3 / P_2^*)$ for different temperatures. Dash lines represent linear regression characteristic of a sample limited by the ionic conductivity.

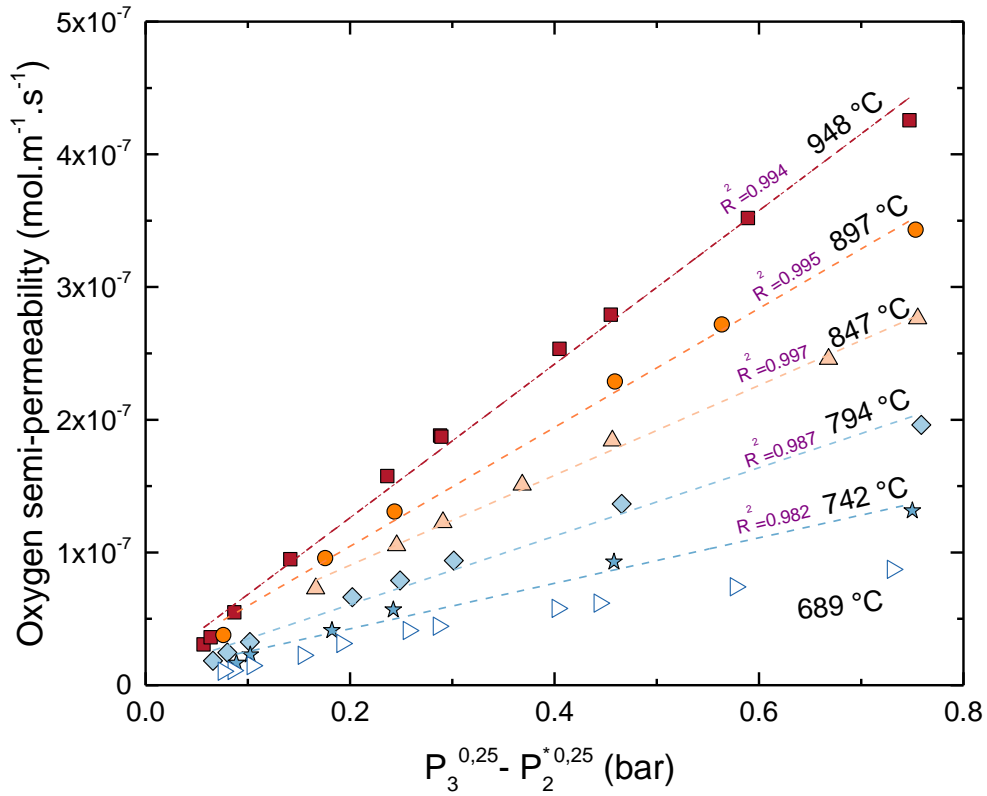


Figure 12: J_{O_2} as a function of $(P_3^{1/4} - P_2^{*1/4})$ for different temperatures. Dash lines represent linear regression characteristic of a sample limited by the electronic conductivity.

Figure 11 and Figure 12 show that, at low temperatures (690 to 800 °C), the flux is governed by $\ln\left(\frac{P_3}{P_2^*}\right)$, whereas between 800 and 950 °C, the best model is $J_{O_2} \propto (P_3^{1/4} - P_2^{*1/4})$. This means that at high temperatures, the flux is limited by electron hole conductivity (and ionic conductivity then dominates), whereas at low temperatures, ionic conductivity is the limiting factor. This interpretation is consistent with previously published results for the same material [1,11,12]. However, there is a difference in the temperature range where the electronic conductivity is limiting in literature [11] which can be attributed to Mn doping in the samples and to the fact that these authors did not take the surface effect into account. A study on the conductivity of CTF and more generally on the bulk and defect structure of CTF will be conducted on the next chapter to provide finer details into these results.

5. Surface polarization study

The electromotive force, E_s , between the metallic and the ceramic probes (Chapter 2 §1.2) is a consequence of the surface exchange on the lean side of the membrane which happens during the oxygen semi-permeation and is referred to as surface polarization. It was measured as a function of temperature using different surface probes: Au, Pt, and Ag metallic probes and Gadolinia-doped Ceria (GDC) and Ytria-stabilized Zirconia (YSZ) cone shaped ceramic probe, with different gas vectors on the lean side (Ar/He). For ease of legibility, the graph (Figure 13) only shows results for the Au and Pt metallic-wire and the GDC ceramic probes for helium but all types of probes yielded comparable results.

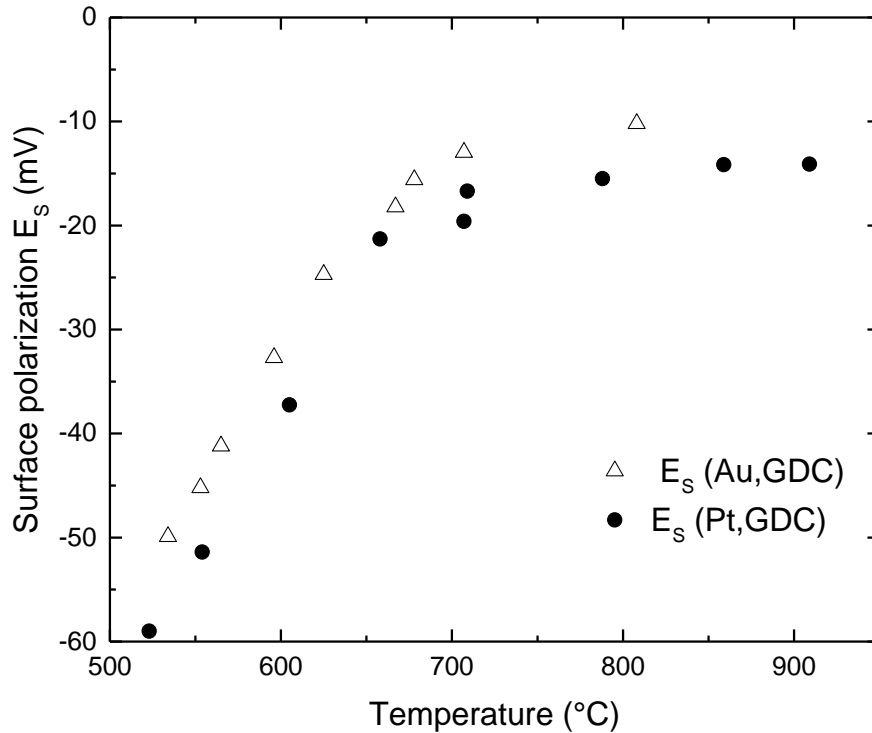


Figure 13: Surface polarization (lean side of the membrane) as a function of temperature for various surface probes.

Note that the surface polarization was independent of the nature of the probes, proving that the nature of the probe does not influence the surface reactions.

Two temperature ranges can be identified: polarization decreased with temperatures for $T < 750$ °C, whereas a plateau was observed for $T > 750$ °C. This behavior confirms that the surface exchange reactions had an increasingly limiting effect on the permeation process with decreasing temperatures. At high temperatures, the surface polarization is practically independent of temperature. This can be explained by, on one hand, the increase in oxygen flux with temperature, which increased surface polarization. However, on the other hand, as the oxygen pressure increased on the lean side, the speed of the surface reactions also increased. Moreover, the rate constants of the surface reactions also increased with temperature. Consequently, at high temperatures, these phenomena compensated and polarization remained constant.

However, polarization evidently occurred at high temperatures regardless ($E_s \neq 0$), indicating that the surface continued to have an impact on the permeation process. Although this effect had a minor impact on the permeation flux (cf. B_c values), further investigation is necessary to gain a better understanding of the effect and to take it into account for modeling (Figure 14).

We further demonstrated the role of surface polarization in the permeation process by recording surface polarization variations on the lean side at 900 °C.

After a rapid increase in oxygen pressure on the oxygen-rich side from argon (10^{-4} bar) to air (0.2 bar), a surface polarization (i.e. $E_s(\text{Au, GDC})$) peak was visible for 100 s (Figure 14a). This peak can be partly ascribed to surface exchanges limiting the permeation process. Indeed, polarization initially increased due to sudden increase of the oxygen partial pressure on the rich-side, which increased the O^{2-} flux within the bulk. This flux then decreased because the difference between the oxygen partial pressures of both sides balances, whereas both the adsorption flux (which is proportional to $\sqrt{P_{\text{O}_2}}$) and the desorption flux (which is proportional to the surface oxygen activity) increased. This resulted in a decrease in polarization until the steady state was reached.

As shown in Figure 14b, which illustrates oxygen pressure variations in the permeate chamber, this phenomenon was local because a monotonous variation in oxygen partial pressures was observed up to the stationary state. Nonetheless, our experiment established that the surface reactions continued to have an effect, even at high temperatures.

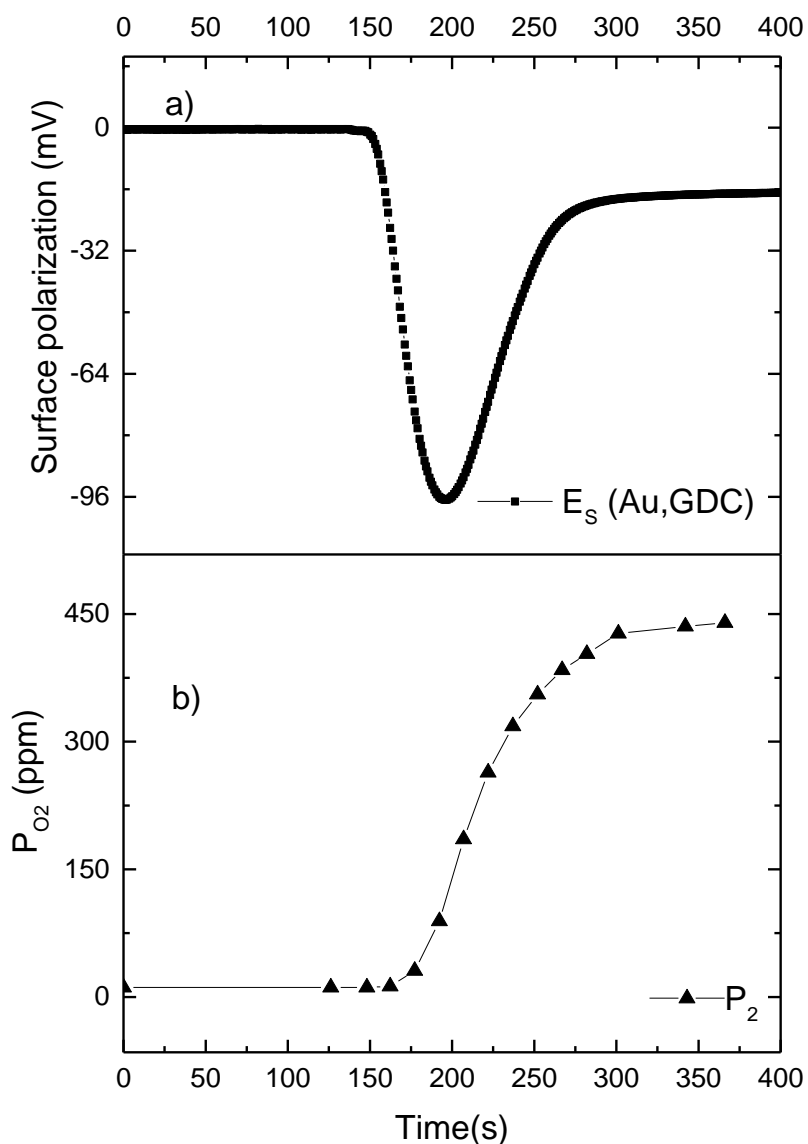


Figure 14: Simultaneous recording of surface polarization variations and of oxygen partial pressure variations on the lean side of the membrane after a rapid change in oxygen pressure on the oxygen-rich side at 900 °C.

6. Conclusion

The setup was used to identify the limiting steps of semi-permeation through a CTF membrane. The experiments revealed that the semi-permeation flux is limited both by surface exchange reactions and by oxygen bulk diffusion below 750 °C, changing to a bulk-limited process at temperatures of above 750 °C. These results were confirmed both with isotopic exchange measurement and with semi permeation experiments on membranes with porous layer.

The critical thickness, L_c , was determined by isotopic exchange measurements at several temperatures. This thickness decreases with temperature increase, meaning that the semi-permeation process becomes mainly limited by bulk diffusion when temperature increases. However, results revealed that the semi-permeation of the 1.3 mm pellet was mixed limited from 700 °C to 900 °C.

Increasing the surface exchange using porous CTF coatings on the oxygen-lean surface led to a significantly increase of oxygen flux below 750 °C as it was expected. The B_c parameter of these membranes confirms that the porous coating changes the limitation from a mixed process (for a bare membrane) to a process limited by oxygen diffusion below 750 °C. This confirm the result obtained with the setup.

Nevertheless, it was demonstrated that the surface continues to have a limiting effect at high temperatures. This indicates that oxygen activity should be used to characterize oxygen permeation instead of relying on oxygen partial pressure in the gas, unless a complex model is used that takes into account the exchange reactions of oxygen on the membrane.

Considering oxygen activity measurements obtained on the membrane surfaces, oxygen bulk diffusion was analyzed independently. The results indicate that the flux was limited by electron hole conductivity at high temperatures, whereas ionic conductivity was the limiting factor at low temperatures.

- [1] J.M. Polfus, W. Xing, M.F. Sunding, S.M. Hanetho, P.I. Dahl, Y. Larring, M.-L. Fontaine, R. Bredesen, Doping strategies for increased oxygen permeability of CaTiO₃ based membranes, *J. Memb. Sci.* 482 (2015) 137–143.
- [2] F.M. Figueiredo, M.R. Soares, V. V. Kharton, E.N. Naumovich, J.C. Waerenborgh, J.R. Frade, Properties of CaTi_{1-x}Fe_xO_{3-δ} Ceramic Membranes, *J. Electroceramics.* 13 (2004) 627–636.
- [3] L.A. Dunyushkina, A.K. Demin, B. V Zhuravlev, Electrical conductivity of iron-doped calcium titanate, *Solid State Ionics.* 116 (1999) 85–88.
- [4] S. Marion, A.I. Becerro, T. Norby, Ionic and electronic conductivity in CaTi_{1-x}Fe_xO_{3-δ} (x=0.1–0.3), *Ionics (Kiel).* 5 (1999) 385–392.
- [5] H.J.M. Bouwmeester, Dense ceramic membranes for oxygen separation, in: *Membr. Sci. Technol.*, Elsevier, 1996: pp. 435–528.
- [6] P.-M. Geffroy, E. Blond, N. Richet, T. Chartier, Understanding and identifying the oxygen transport mechanisms through a mixed-conductor membrane, *Chem. Eng. Sci.* (2017).
- [7] P.M. Geffroy, A. Vivet, J. Fouletier, C. Steil, E. Blond, N. Richet, P. Del Gallo, T. Chartier, The Impact of Experimental Factors on Oxygen Semi-Permeation Measurements, *J. Electrochem. Soc.* 160 (2013) F60–F68.
- [8] O. Valentin, E. Blond, N. Richet, Thermo-Chemo-Mechanical Modelling of Mixed Conductors in Transient Stages, *Adv. Sci. Technol.* 65 (2010) 232–237.
- [9] P.M. Geffroy, A. Vivet, J. Fouletier, N. Richet, P. Del Gallo, T. Chartier, Influence of Oxygen Surface Exchanges on Oxygen Semi-Permeation through La_(1-x)Sr_xFe_(1-y)GayO_{3-δ} Dense Membrane, *J. Electrochem. Soc.* 158 (2011) B971.
- [10] H.J.M. Bouwmeester, H. Kruidhof, A.J. Burggraaf, Importance of the surface exchange kinetics as rate limiting step in oxygen permeation through mixed-conducting oxides, *Solid State Ionics.* 72 (1994) 185–194.
- [11] J.M. Polfus, W. Xing, G. Pećanac, A. Fossdal, S.M. Hanetho, Y. Larring, J. Malzbender, M.-L. Fontaine, R. Bredesen, Oxygen permeation and creep behavior of Ca_{1-x}Sr_xTi_{0.6}Fe_{0.15}Mn_{0.25}O_{3-δ} (x=0, 0.5) membrane materials, *J. Memb. Sci.* 499 (2016) 172–178.
- [12] J.M. Polfus, W. Xing, M. Riktor, M.F. Sunding, P.I. Dahl, S.M. Hanetho, T. Mokkelbost, Y. Larring, M.-L. Fontaine, R. Bredesen, Enhanced O₂ Flux of CaTi_{0.85}Fe_{0.15}O_{3-δ} Based Membranes by Mn Doping, *J. Am. Ceram. Soc.* 99 (2016) 1071–1078.

CHAPTER 5

CTF DEFECTS

Pour agir, il faut une forte dose de défauts. Un homme sans défauts n'est bon à rien.

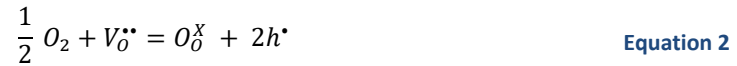
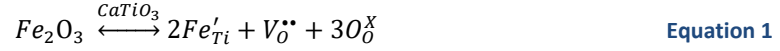
Jacques Chardonne (Propos comme ça, 1966)

Table of content

| | |
|---|-----|
| 1. Introduction..... | 91 |
| 2. Conduction properties..... | 92 |
| 2.1 Comparison with theory..... | 93 |
| 3. Determination of the oxygen non-stoichiometry | 97 |
| 3.1 Under standard conditions / atmosphere..... | 97 |
| 3.1.1 Effect of temperature..... | 97 |
| 3.2 Effect of reducing atmosphere..... | 100 |
| 3.2.1 XRD study..... | 100 |
| 3.2.2 TGA study..... | 100 |
| 3.2.3 TPR study | 101 |
| 3.2.4 Interpretation | 102 |
| 4. Ionic conductivity | 106 |
| 4.1 Ionic conductivity obtained by isotopic exchange | 106 |
| 4.2 Comparison between ionic conductivity calculated from different techniques at different P_{O_2} | 106 |
| 5. Conclusion | 110 |

1. Introduction

CTF is formed when doping pure perovskite with iron. This creates oxygen vacancies and also electron and electron holes responsible for the mixed conductivity of the CTF.

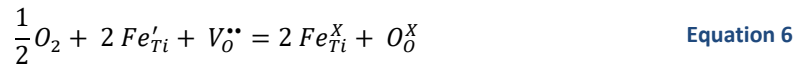


Consequently, the electroneutrality is

$$2[V_O^{\bullet\bullet}] + [h^{\bullet}] = [e'] + [Fe'_{Ti}] \quad \text{Equation 4}$$

In theory, if all iron substitute titanium as in Equation 1, one mole of iron atoms introduced in the material is able to generate half a mole of oxygen vacancies. When 10% iron is added, the oxygen non-stoichiometry, δ , is equal to 0.05 leading to $CaTi_{0.9}Fe_{0.1}O_{2.95}$.

However, it seems possible to have Fe^{IV} in the material and the equilibrium Fe^{IV}/Fe^{III} influences the electronic conductivity and the value of δ [1–3].



It is thus important to be able to determine the amount of Fe^{IV} to know the oxygen non-stoichiometry. Moreover, some iron could be present under the valence Fe^{II} .

One might thus include reaction at low oxygen partial pressure:



Thus the electroneutrality condition becomes

$$2[V_O^{\bullet\bullet}] + [h^{\bullet}] = [e'] + [Fe'_{Ti}] + 2[Fe''_{Ti}] \quad \text{Equation 8}$$

Moreover, the non-stoichiometry evolves with temperature and oxygen partial pressure and needs to be monitored. The variation of δ may have an impact on the conductivity and on the semi-permeation of the CTF.

Different experiments were performed to try to assess the oxygen non-stoichiometry of the CTF under different P_{O_2} and temperatures. Moreover, the study of the conductivity under different partial pressures by different ways is important and may be useful to understand the defect chemistry of the CTF.

2. Conduction properties

In the previous chapter, I observed, via semi-permeation experiments, that at high temperatures, the flux was limited by electron hole conductivity (and ionic conductivity then dominates), whereas at low temperatures, ionic conductivity was the limiting factor. Previous studies on the conductivity of CTF have demonstrated this singular behavior [4,5]. In particular, these studies substantiate the increase in ionic transport numbers with temperature (t_i of about 0.6 at 900 °C under atmospheric pressure). This behavior was verified by conductivity measurements.

The total conductivity was recorded by impedance spectroscopy and results are plotted as a function of P_{O_2} for different temperatures in Figure 1.

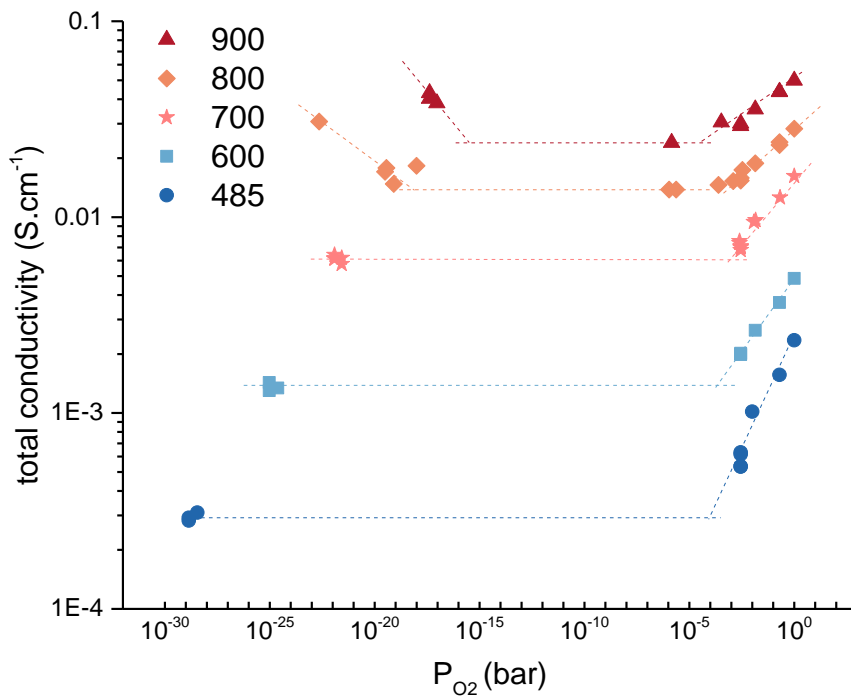


Figure 1: CTF total conductivity as a function of P_{O_2} for different temperatures. Dash lines are just eye guides.

CTF exhibits a mixed behaviour with an n-conductivity, an ionic one and p-conductivity at temperatures higher than 800 °C and an ionic and p-conductivity for temperatures lower than 800 °C. The ionic conductivity is assumed to be constant over a wide range of P_{O_2} [4,6,7]. It can be seen that the ionic transport number ($t_i = \frac{\sigma_i}{\sigma_{tot}}$ with σ_i the conductivity of ionic plateau) (Table 1) increases with temperature. It correlates with conclusion of the previous chapter based on permeation measurements which demonstrated that the CTF semi-permeation flux becomes limited by the electronic conductivity at high temperature while it is limited by the ionic one at low temperature. It also corresponds with literature results [4,6,8,9].

Table 1: Ionic transport numbers for different P_{O_2} .

| Temperature (°C) | t_i at different P_{O_2} (bar) | | |
|------------------|------------------------------------|-----------|-----------------|
| | 1 (bar) | 0.2 (bar) | 10^{-5} (bar) |
| 900 | 0.57 | 0.65 | 0.95 |
| 800 | 0.51 | 0.59 | 0.91 |
| 700 | 0.38 | 0.49 | 0.88 |
| 600 | 0.17 | 0.26 | 0.67 |
| 500 | 0.12 | 0.19 | 0.46 |

2.1 Comparison with theory

Total conductivity as a function of oxygen partial pressure was fitted, based on theory described in literature [4]. Ionic conductivity is supposed to be constant over oxygen partial pressure.

$$\sigma_{tot} = \sigma_{ionic} + \sigma_h + \sigma_e \quad \text{Equation 9}$$

Expression of electron holes (h^*) conductivity and electrons (e^-) conductivity came from Equation 2 and Equation 3. The concentration of these species are proportional to $P_{O_2}^{1/4}$ and $P_{O_2}^{-1/4}$, respectively.

Consequently, conductivity as a function of oxygen partial pressure can be expressed as follow:

$$\sigma_{tot} = \sigma_{ionic} + \sigma_h^0 \times P_{O_2}^{1/4} + \sigma_e^0 \times P_{O_2}^{-1/4} \quad \text{Equation 10}$$

σ_h^0 and σ_e^0 are the electron hole conductivity and electron conductivity at an oxygen partial pressure of 1 bar, respectively.

Fits were calculated in Origin®. Results are plotted below in Figure 2 and values are given in Table 2. The fit at 485 °C was obtained fixing the ionic conductivity at $2.8 \times 10^{-4} \text{ S.cm}^{-1}$ (conductivity of the plateau) because otherwise, the ionic conductivity was too low and an important n type conductivity was found.

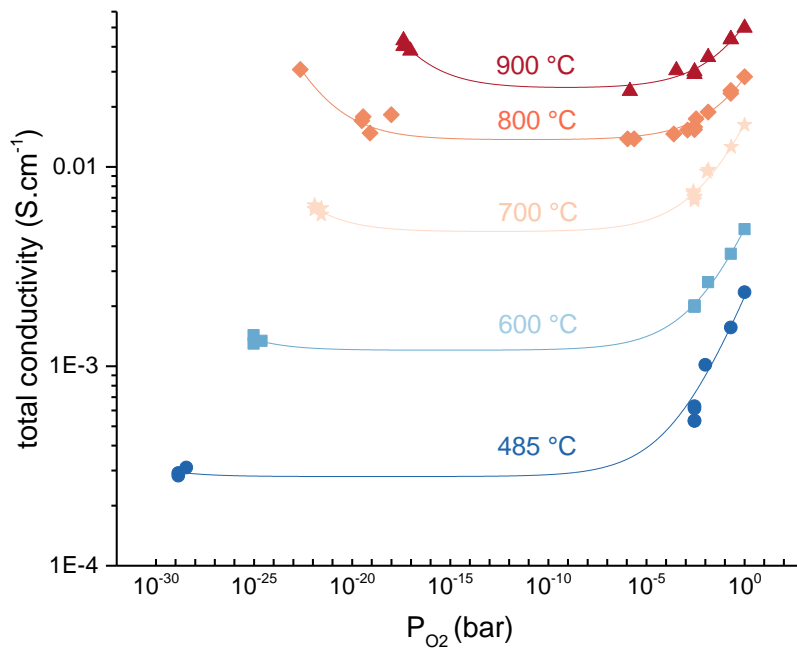


Figure 2: Fits on the CTF total conductivity as a function of P_{O_2} for different temperatures.

Table 2: Ionic, electron hole and electron conductivities obtained with modelling at different temperatures.

| Temperature (°C) | σ_i (S.cm ⁻¹) | σ_h (S.cm ⁻¹) | σ_e (S.cm ⁻¹) |
|------------------|----------------------------------|----------------------------------|----------------------------------|
| 900 | 0.0247 | 0.0267 | 7.58×10 ⁻⁷ |
| 800 | 0.0137 | 0.0144 | 3.82×10 ⁻⁸ |
| 700 | 0.00473 | 0.0117 | 5.00×10 ⁻⁹ |
| 600 | 0.00120 | 0.00368 | 9.13×10 ⁻¹¹ |
| 485 | 2.8×10 ⁻⁴ | 0.00195 | 8.90×10 ⁻¹³ |

Ionic conductivity σ_i , electron hole and electron conductivities (σ_h and σ_e) are plotted at 1 bar as a function of temperature to determine the activation energy of both conductivities (Figure 3) (Table 3).

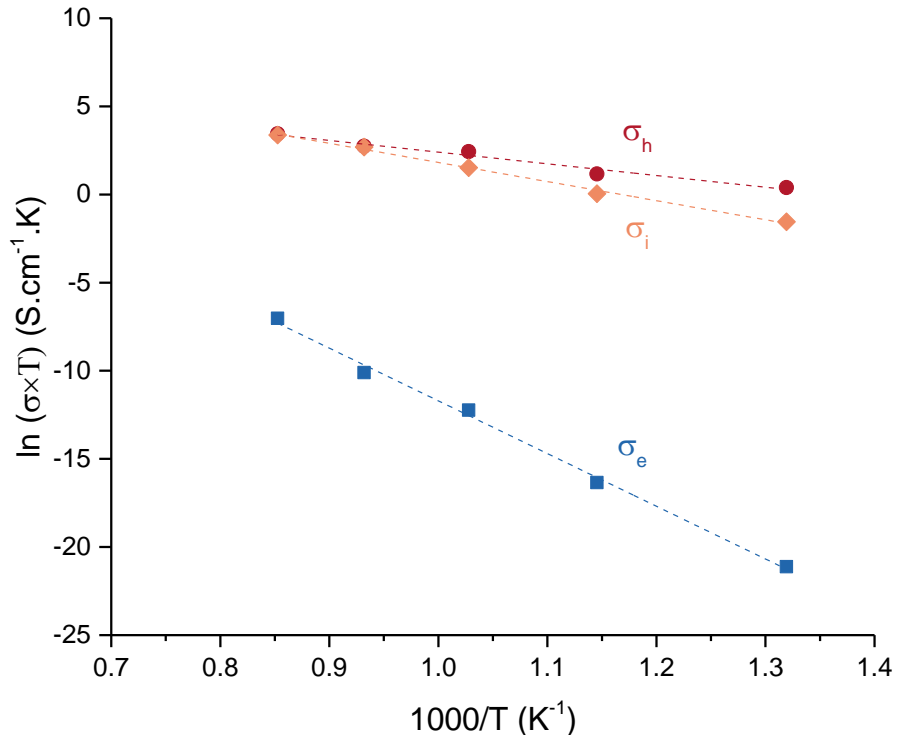


Figure 3: Ionic conductivity, electron hole and electron conductivities as a function of temperature at $P_{O_2} = 1$ bar.

Table 3: Activation energies of ionic conductivity, electron hole and electron conductivities.

| Activation energy | σ_i | σ_h | σ_e |
|-------------------|-------------|------------|------------|
| from this work | 0.94 eV | 0.57 eV | 2.6 eV |
| from literature | 0.87 eV [4] | 0.1 eV [4] | 2.7 eV [4] |
| | 1.0 eV [6] | 0.4 eV [6] | 2.2 eV [6] |

It was assumed that, as usually in MIEC, the electron hole conductivity follows the adiabatic small polaron mechanism [7]. Then,

$$\sigma_h = \frac{A}{T} \exp\left(\frac{-E_A}{k \times T}\right) \quad \text{Equation 11}$$

with A, a constant independent of temperature.

The activation obtained in this work is higher than literature results [4,6] but in literature, it seems to be calculated according to the relation $\sigma_h = A \exp\left(\frac{-E_A}{k \times T}\right)$ while it is indicated that the holes migrates by hopping mechanisms...

In literature [4], it has been assumed that the defect electron follows the free electron band-type conduction. However, electron conductivity increases with temperature, with an activation energy as high as 2.7 eV. Consequently, it was assumed, in this work, that the electron conductivity also follows the small polaron mechanism.

Each conductivity (ionic, electron hole and electron ones) are plotted as a function of P_{O_2} for different temperatures in Figure 4.

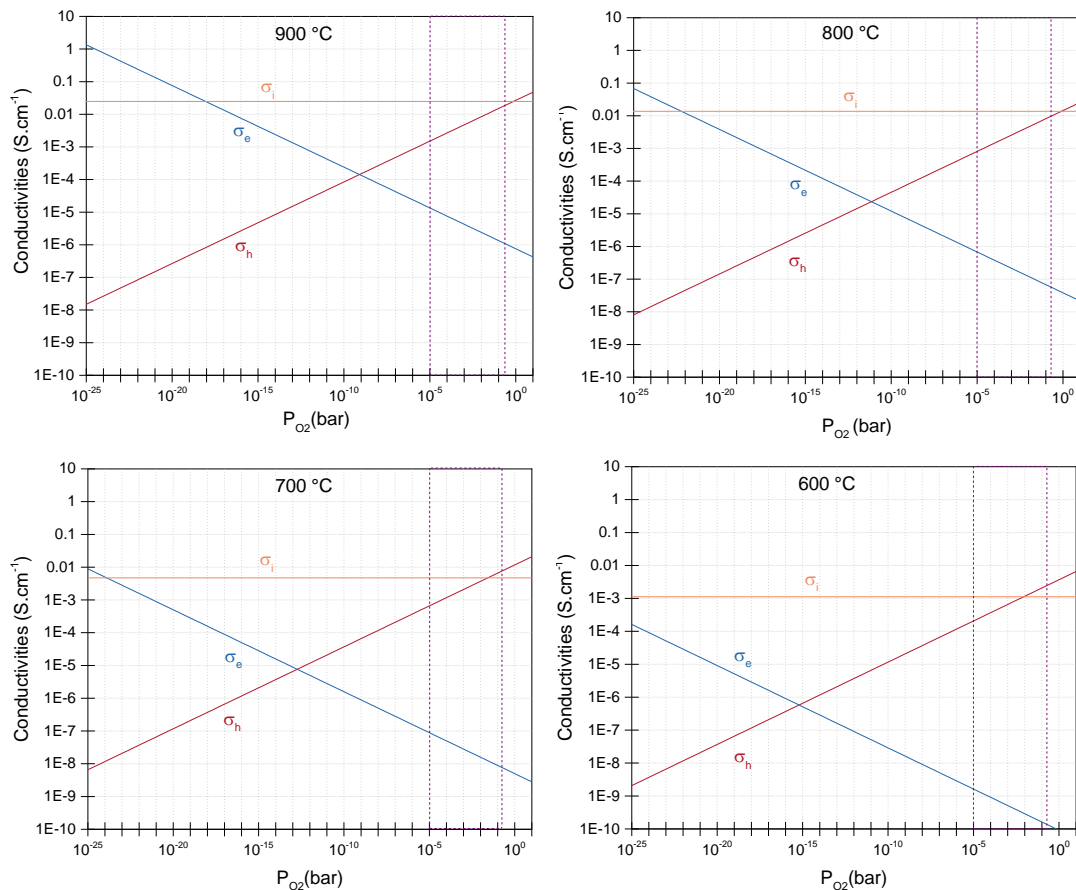


Figure 4: Patterson diagrams (conductivities as a function of oxygen partial pressure) at 900, 800, 700 and 600 °C. Dash line represent the oxygen partial pressure range were semi permeation occurs.

These diagrams (Figure 4) show that, in the range of P_{O_2} used in semi-permeation measurements (usually between 10⁻⁵ to 1 bar), the ionic conductivity becomes lower than the electron hole conductivity at 600 and 700 °C, while at higher temperatures, ionic conductivity is higher than the electron hole conductivity. This confirms results obtained in semi permeation.

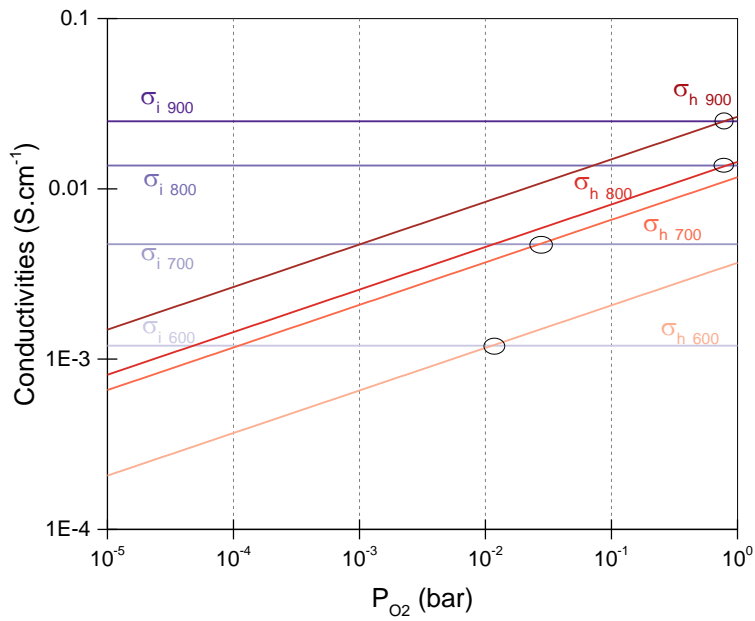


Figure 5: Zoom on the Patterson diagrams to evidence the oxygen partial pressure where electron hole conductivity crosses the ionic conductivity.

Figure 5 evidences the oxygen partial pressure of the intersection of the electron hole conductivity and the ionic conductivity. This value increases with temperature but is almost the same at 800 and 900 °C.

However, this study is based on the fact that ionic conductivity is constant over a wide range of P_{O_2} . Nevertheless, as it was exposed in the introduction, the valence of the iron can change as a function of the P_{O_2} and this could influence the electrical properties and especially the ionic conductivity even if the amount of oxygen vacancies is very low (5% if all the iron is in Fe^{III}). A study on the oxygen non-stoichiometry and its evolution as a function of P_{O_2} was then performed.

3. Determination of the oxygen non-stoichiometry

Different methods were used to try to determine the oxygen non-stoichiometry, δ , of the CTF. This value can be calculated with the concentration of Fe^{III} . Indeed, two Fe^{III} generate one oxygen vacancy whereas it is not the case with Fe^{IV} .

3.1 Under standard conditions / atmosphere

Mössbauer study can be performed to determine the oxygen non stoichiometry at atmospheric pressure. It was performed in Bordeaux by Alain WATTIAUX and Mathieu DUTTINE. Spectra of the starting fired powder were recorded at room temperature (Figure 6).

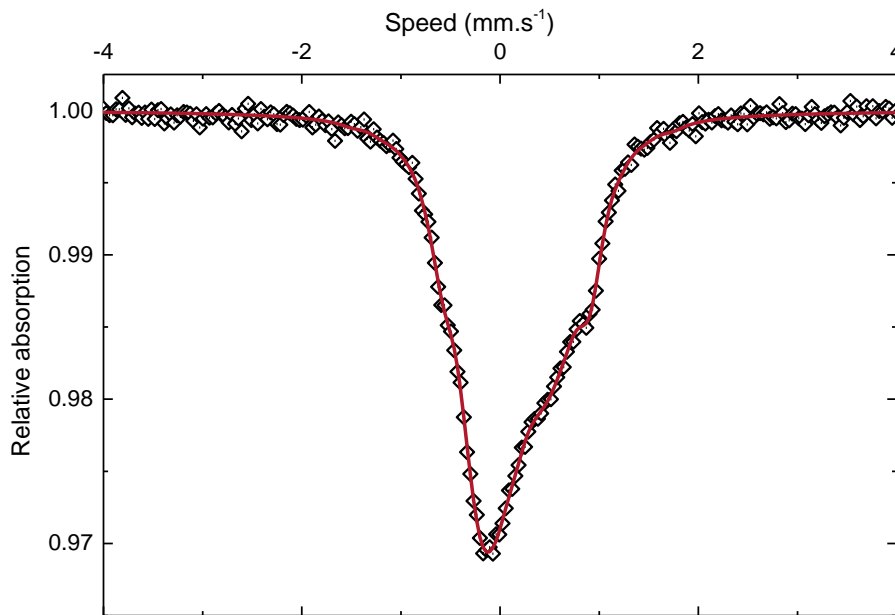


Figure 6: Mössbauer spectrum of CTF at room temperature.

Fe^{IV} and Fe^{III} are present on the material, with different coordinations (from tetrahedral to octahedral coordination). However, with all these possibilities (2 oxidation degrees and 3 different coordinations possible), it is almost impossible to determine the exact ratio between the iron Fe^{III} and Fe^{IV} with this experience alone.

3.1.1 Effect of temperature

Expansion as a function of temperature has been studied to evidence if chemical expansion occurs (Figure 7). Chemical expansion is the results of the repulsion of the cations surrounding the oxygen vacancy [10,11].

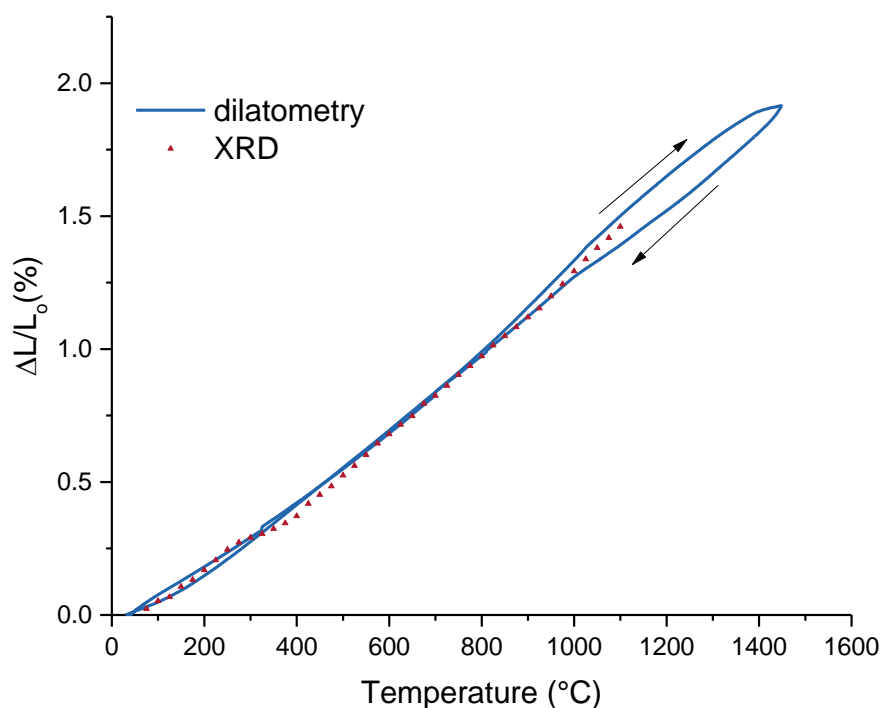


Figure 7: Expansion curve of CTF as a function of temperature in air by dilatometer and HT-XRD.

The thermal expansion coefficient (TEC) can be estimated during heating over a quasi-linear zone between 150 °C and 800 °C. The CTE value was estimated at $13.9 \times 10^{-6} \text{ } ^\circ\text{C}^{-1}$ in air. The slope of the linear shrinkage curve increased slightly above 800 °C, with an estimated TEC between 800 and 1200 °C of $16.8 \times 10^{-6} \text{ } ^\circ\text{C}^{-1}$ under air. The increase in the slope from 800 °C can be associated with lattice expansion caused by oxygen loss (chemical expansion) [11–13].

This characterization was completed with the analysis of the lattice volume variation by in situ high temperature powder XRD. The thermal expansion of the volume cell as a function of temperature showed a linear positive correlation between the lattice volume and temperature. It is then possible to determine the volume thermal expansion coefficient (VTEC) which can be approximated to the TEC via $\text{TEC} = \text{VTEC}/3$ (Figure 7). With this technique a TEC equal to $14.8 \times 10^{-6} \text{ } ^\circ\text{C}^{-1}$ between 25 °C and 800 °C and of $16.4 \times 10^{-6} \text{ } ^\circ\text{C}^{-1}$ between 800 and 1100 °C were found which is consistent with results obtained with dilatometer measurements.

Similar values were obtained under argon ($13.1 \times 10^{-6} \text{ } ^\circ\text{C}^{-1}$ between 25-800 °C and an estimated TEC between 800 and 1200 °C of $17.0 \times 10^{-6} \text{ } ^\circ\text{C}^{-1}$) (Figure 8). No additional chemical expansion was visible.

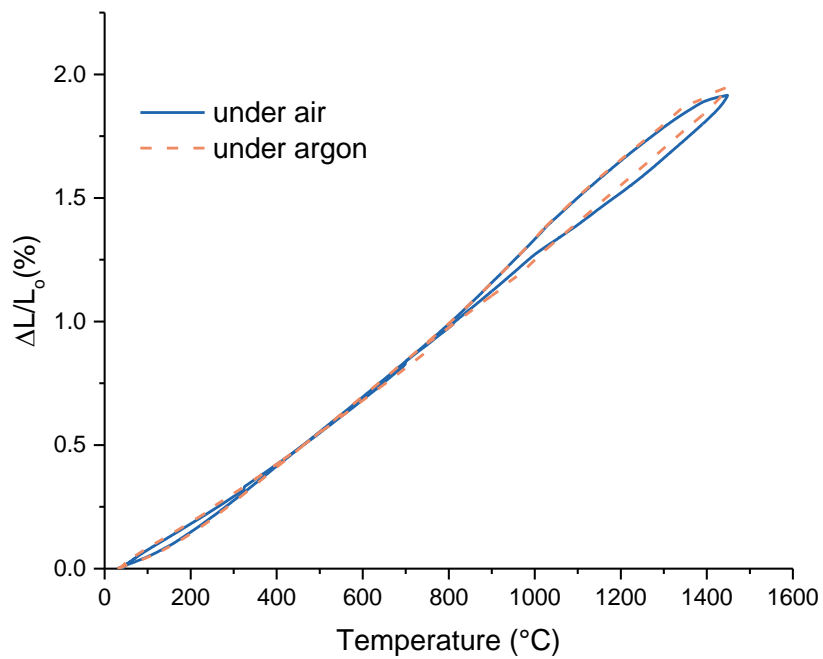


Figure 8: Thermal expansion curve of CTF under air and argon obtained by dilatometer.

As exposed before, a chemical expansion can appear in the material while increasing the temperature, due to oxygen vacancies formation. This could be visible in dilatometer measurement but also in TGA measurements as it corresponds to a loss of oxygen. TGA experiments were performed under air and argon. Results are plotted in Figure 9.

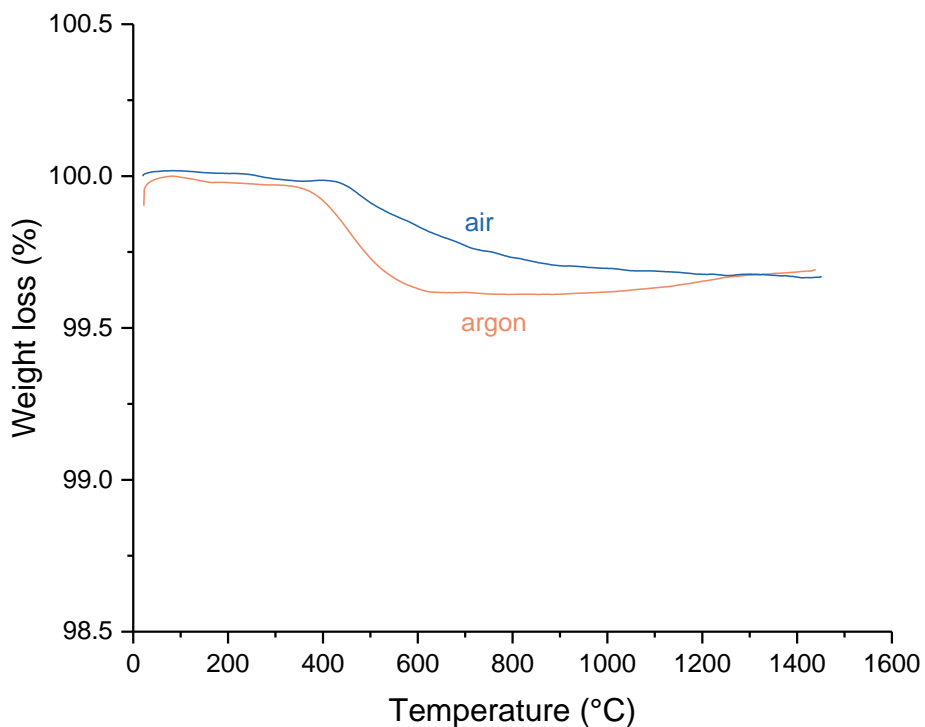


Figure 9: Thermogravimetry measurement under air and argon of CTF.

A small loss of weight (0.4%) appeared around 400-500 °C as well as a small weight recovery after 1000 °C under argon which is not explained. There was no weight change from 800 °C in air, as one could expect with

dilatometer results, within the resolution of the method. No definitive conclusions can be done with these two experiments.

3.2 Effect of reducing atmosphere

3.2.1 XRD study

The behavior of the CTF under hydrogen was investigated. First, XRD analyses were done under 3% H₂ in nitrogen from 25 to 800 °C and the lattice parameters were calculated via Rietveld refinement. These results were compared with lattice parameters calculated from an XRD analyze on the same diffractometer under air (Figure 10).

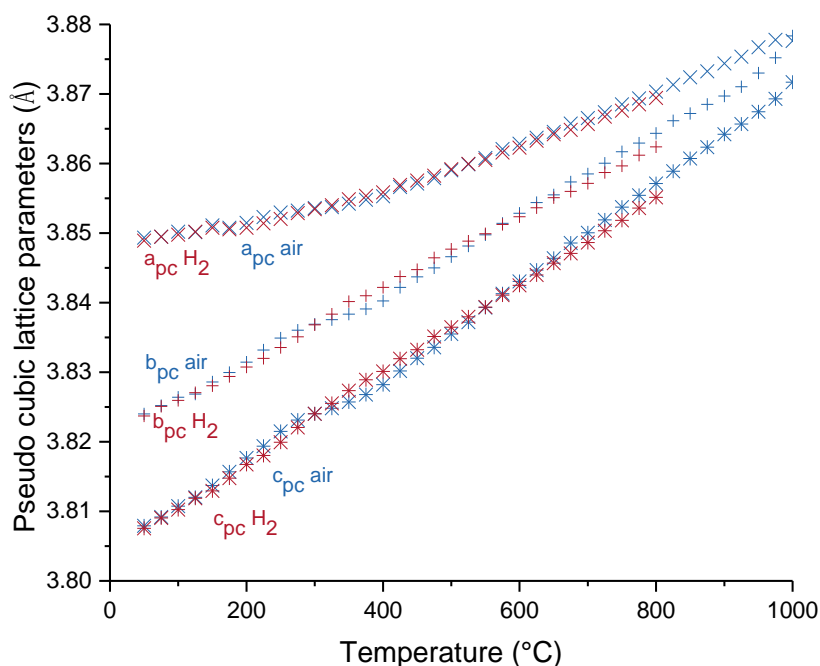


Figure 10: Pseudo cubic lattice parameters calculated via Rietveld refinement during heating up to 800 °C under 3% H₂ and during heating up to 1100°C under air.

No visible difference was found between air and 3% H₂. The perovskite structure was still present up to 800 °C and there were no additional phases. Almost the same TEC value than under air was calculated ($12.7 \times 10^{-6} \text{ °C}^{-1}$ under 3% H₂ instead of $13.1 \times 10^{-6} \text{ °C}^{-1}$ under air) between 25 to 800 °C. However, a reduction under hydrogen is expected. Nevertheless, such reduction cannot be invisible in XRD because the different iron loading on the CTF (i.e. 20% iron doped CTF, 10% iron doped CTF and pure perovskite) have almost the same XRD pattern (in the detection limit of the diffractometers used). As XRD was not successful studying the evolution of CTF under hydrogen, other methods were used.

3.2.2 TGA study

Thermogravimetric analysis was performed on CTF powder under hydrogen (Figure 11). After a cleaning under argon for 1 h at 200 °C, the CTF powder was heated at 2 °C/min under 3% H₂/N₂ to 1000 °C. There was a step of 160 minutes before cooling down to room temperature at 20° C/min.

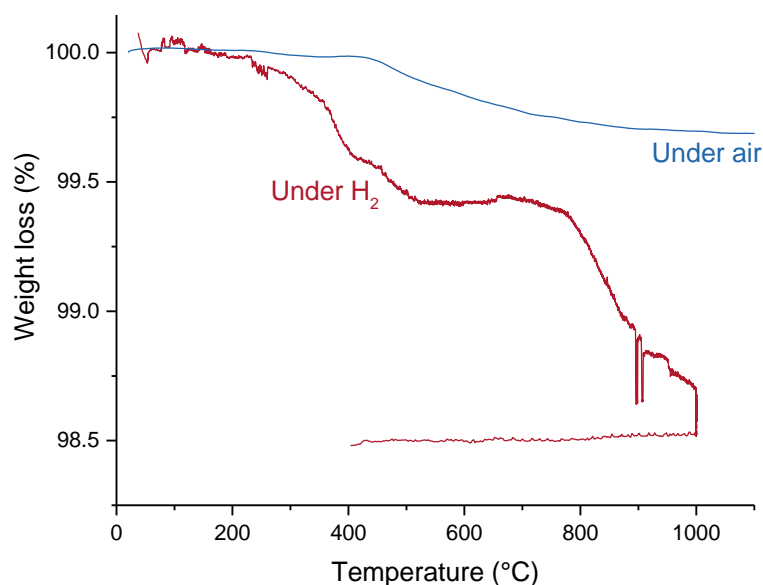


Figure 11: Thermogravimetry curve of CTF under air (bleu) and under 3% hydrogen (red).

The thermogravimetry measurement showed a first loss of above 0.6 wt.% from 100 °C to 500 °C, followed by a loss of 0.9 wt.% up from 700 °C to 1000 °C.

3.2.3 TPR study

Temperature programmed reduction (TPR) measurement was performed on 0.206 g of CTF powder (Figure 12). After an oxidation step under pure O₂ during 2 h at 800 °C (heating rate 10 °C/min), the CTF was cooled down under helium and powder was heated at 10 °C/min under 3% H₂/Ar (30 ml/min) to 1000 °C. There was a step of 1 hours before cooling down to room temperature. Experiments with longer step (10 h) showed similar results indicating that the reduction at 1000 °C was over.

The equipment was calibrated to be able to quantify the amount of hydrogen which reacted during the peaks visible on Figure 12.

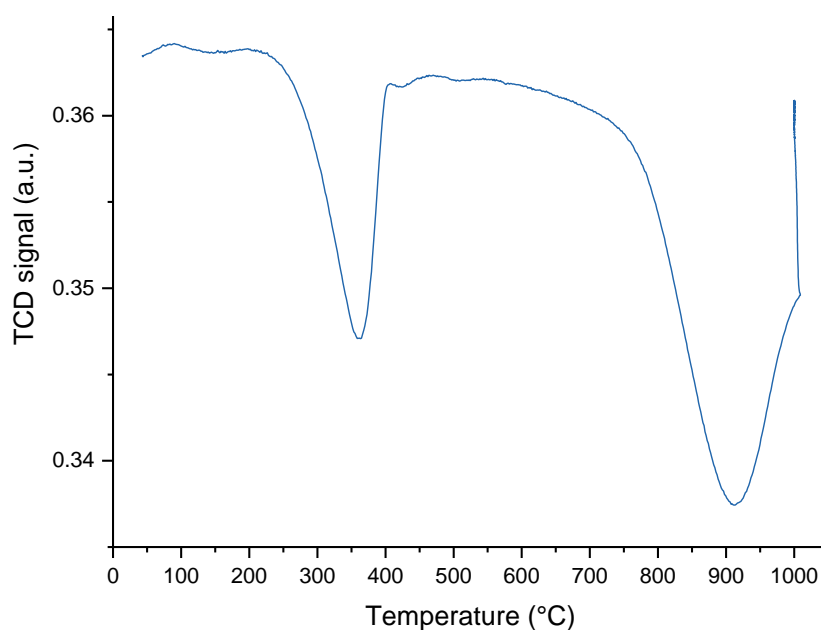


Figure 12: Temperature Programmed Reduction curve of CTF.

From 200 °C to 400 °C the first peak represents 69 $\mu\text{mol/g}$ of H_2 and from 700 °C to 1000 °C, the second peak represents 281 $\mu\text{mol/g}$ of H_2 .

3.2.4 Interpretation

To interpret the TGA and TPR data, it is important to know the oxidation degree of iron after each reduction steps. XRD and Mössbauer study were performed after the TPR measurement at 600 °C, after TPR at 1000 °C and after TGA at 1000 °C (only XRD).

XRD measurements are plotted in Figure 13 and Figure 14.

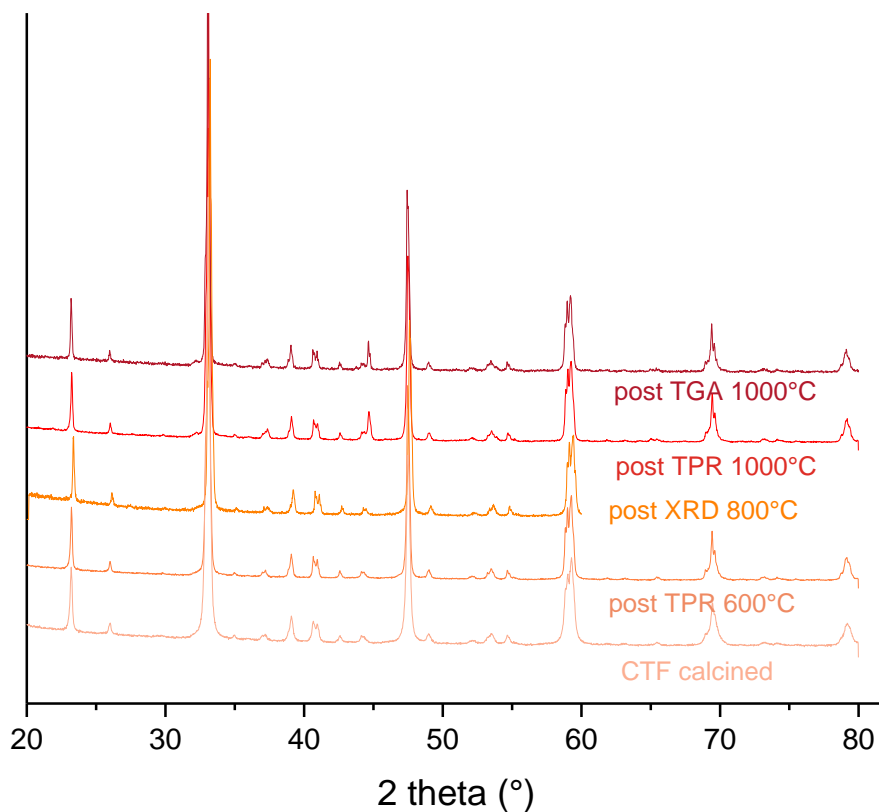


Figure 13: Normalized XRD patterns of the CTF powder after calcination under air, after TPR measurement at 600 °C, after XRD under hydrogen at 800 °C, after TPR at 1000 °C and after TGA at 1000 °C.

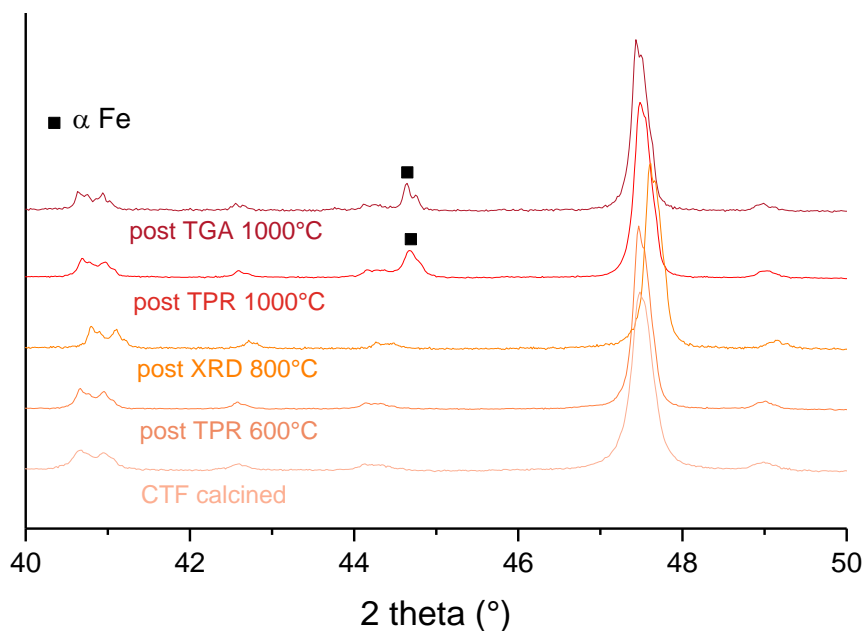


Figure 14: Zoom on a normalized XRD patterns of the CTF powder after calcination under air, after TPR measurement at 600 °C, after XRD under hydrogen at 800 °C, after TPR at 1000 °C and after TGA at 1000 °C to assess the presence of metallic iron.

Both XRD post TPR at 600 °C and post XRD at 800 °C show no sign of metallic iron (Figure 14). No visible difference with CTF calcined is observed (Figure 13). However, it is impossible to determine the valence of the iron in the perovskite structure (it can be Fe^{IV}, Fe^{III} or even Fe^{II}) with XRD.

The XRD post TGA and post TPR at 1000 °C evidence the presence of metallic iron. Rietveld refinement were performed on these spectra and quantification reveal that there is around 40% of the iron which is in the metallic state (then no more in the perovskite structure) (1.6wt% of Fe).

The residual powder after TPR measurement at 600 °C was analyzed in Mössbauer spectroscopy (Figure 15).

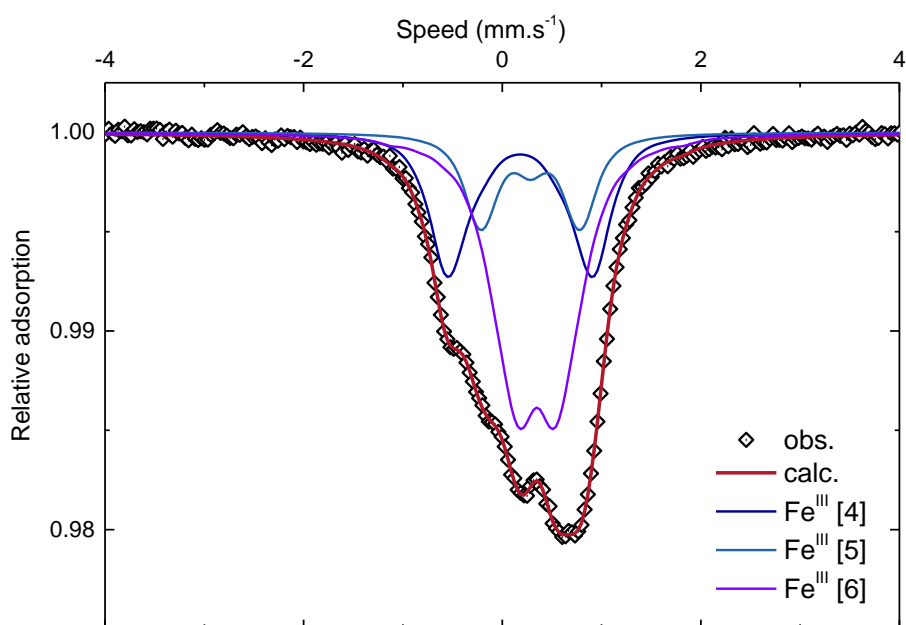


Figure 15: Mössbauer data of CTF powder after treatment in TPR at 600 °C.

Only Fe^{III} was evidenced with different coordinations but no Fe^{IV} anymore and neither Fe^{II}. Consequently, one can assume that the first reduction which occurred in TPR from 200 °C to 400 °C corresponds to the reduction of Fe^{IV} in Fe^{III}. The quantification of the first peak represents 69 μmol/g of H₂ while 1 mole of H₂ can reduce 2 moles of Fe^{IV} in Fe^{III}. 0.206 g of powder were tested, therefore 14.19 μmol of H₂ were consumed which corresponds to the reduction of around 20% of Fe^{IV} in Fe^{III}.

One can then assume that the initial powder tested in TPR has the following composition: CaTi_{0.9}Fe^{III}_{0.08}Fe^{IV}_{0.02}O_{2.96}. Consequently, the oxygen non stoichiometry becomes 3-(0.08/2) = 2.96. This is consistent with literature study which showed that for CTF doped with 5 or 20% iron, for a sample annealed in air and slowly cooled down, the amount of Fe^{IV} was equal to ≈ 20% for both samples [14].

In TPR, it can also be assumed that the second reduction peak corresponds to the reduction of Fe^{III} in metallic iron. Indeed, the Mossbauer study of the compound after TPR only shows the presence of metallic iron and Fe^{III} (Figure 16).

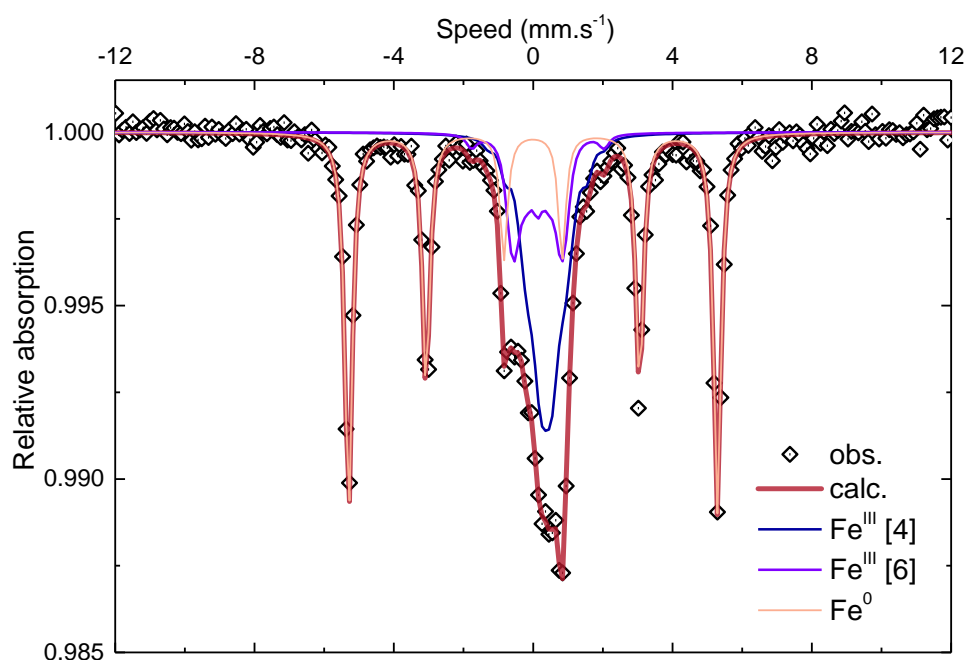


Figure 16: Mössbauer data of CTF powder after treatment in TPR at 1000 °C.

The quantification of the second peak represents 281 μmol/g of H₂ while 1.5 moles of H₂ can reduce 1 mole of Fe^{III} in metallic iron. 0.206 g of powder were tested, therefore 57.80 μmol of H₂ were consumed which corresponds to the reduction 27% of Fe^{III} in metallic iron.

In TGA, a first loss of above 0.6 wt.% from 100 °C to 500 °C was found, followed by a loss of 0.9 wt.% from 700 °C to 1000 °C. If we assume that the two weight losses correspond to the same reduction steps than in TPR, we can also quantify each loss. The first 0.6 wt.% loss corresponds to the reduction 50% of Fe^{IV} in Fe^{III} and the second 0.9 wt.% loss corresponds to the reduction 25.5% of Fe^{III} in metallic iron.

Results of TPR and TGA are very similar. It is important to note that, as the experiment conditions are different, one cannot be sure that after the first weight loss at 500 °C in TGA, only Fe^{III} is present (no Mössbauer study was performed).

A collaboration with the Mikhail Patrakev enables to have a coulometric titration of the CTF.

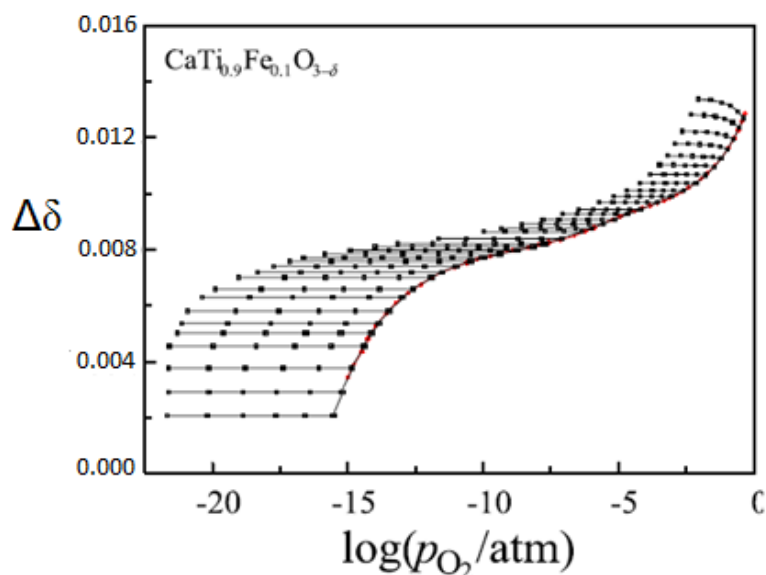


Figure 17: Evolution of δ as a function of P_{O_2} for the CTF at different temperatures (each curve represent a temperature from 700 to 950 °C each 50 °C).

The evolution of δ as a function of P_{O_2} for different temperatures was measured (Figure 17). There is an increase of around 0.012 in δ from the lowest P_{O_2} to air. But to determine the oxygen non stoichiometry, model of defect chemistry of the CTF should be applied however, the simple models describe in the introduction are not sufficient to find a good correlation between the experimental values and the theory, especially at intermediate P_{O_2} . Nevertheless, this result is coherent with the variation of δ obtained at 600 °C after TPR experiment where it was found that δ varies from 0.04 at room temperature to 0.05 at 600 °C under 3% H_2/Ar . But after 800 °C, we evidenced a reduction in metallic iron which should decrease the δ value, which seems not to happen in the coulometric experiment.

Consequently, from know, it was assumed that, at atmospheric pressure, 20% of the iron was on the Fe^{IV} state and then the δ was equal to 0.04.

4. Ionic conductivity

4.1 Ionic conductivity obtained by isotopic exchange

Isotopic exchange was carried out on CTF pellets (cf. chapter 4) under air (Table 4). It is possible to determine the ionic conductivity via the oxygen diffusion coefficient (D^*) (Equation 12, Equation 13).

$$D^* = D_o \times 0.69 \text{ and } D_o = \frac{\sigma_i RT}{C_o 4F^2} \quad \text{Equation 12}$$

$$\sigma_i = \frac{D^* C_o 4F^2}{0.69 \times RT} \quad \text{Equation 13}$$

F : Faraday constant = 96 485 C.mol⁻¹;

C_o : Concentration of oxygen expressed as follow:

$$C_o = \frac{4 * (3 - \delta)}{V_m * N_A} \quad \text{Equation 14}$$

V_m : Molar volume equal to 224×10⁻²⁴ cm³

N_A : Avogadro number 6.022×10²³ mol⁻¹

δ : Oxygen over-stoichiometry = 0.04, meaning that 80% of the iron are Fe'_{Ti} and 20% Fe^x_{Ti}

Table 4: Oxygen diffusion obtained via isotopic exchange and calculation of ionic conductivity.

| T (°C) | D^* (cm ² .s ⁻¹) | σ_i (S.cm ⁻¹) |
|-----------|--|-------------------------------------|
| 700 | 6.7×10 ⁻⁹ | 3.9×10 ⁻³ |
| 800 | 1.7×10 ⁻⁸ | 8.8×10 ⁻³ |
| 900 | 3.8×10 ⁻⁸ | 1.8×10 ⁻² |

4.2 Comparison between ionic conductivity calculated from different techniques at different P_{O_2}

Figure 18 plots the ionic conductivity as a function of temperature obtained with different techniques and also found in literature.

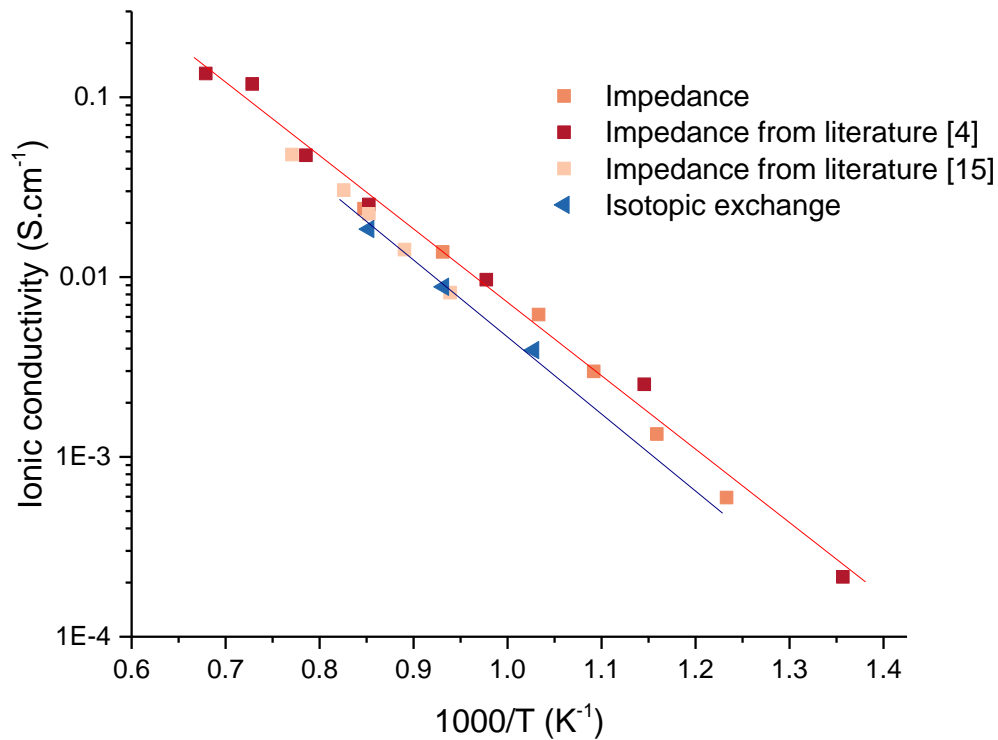


Figure 18: Ionic conductivity obtained with different methods as a function of temperature.

Results obtained with impedance spectroscopy are around 1.6 times higher than results obtained via isotopic exchange or permeation measurements. However, all the results seem to have a similar slope. The activation energies (obtained when plotting $\ln(\sigma \times T)$ as a function of $1/T$) are comprised between 0.8 and 1 eV for isotopic exchange and impedance spectroscopy which is coherent with the ones obtained in literature with impedance spectroscopy (0.9 eV [4,15]) and the 4 probe method (0.9 eV [16]).

However, the ionic conductivity values obtained with impedance are higher. This can be explained because the ionic conductivity measurements in impedance spectroscopy are realized under a low P_{O_2} (a P_{O_2} between 10^{-15} – 10^{-5} bar). Under these more reduced conditions, the number of Fe^{IV} is then lower than under air thus the concentration of oxygen vacancy is higher. This was confirmed by Mössbauer spectroscopy (Figure 19).

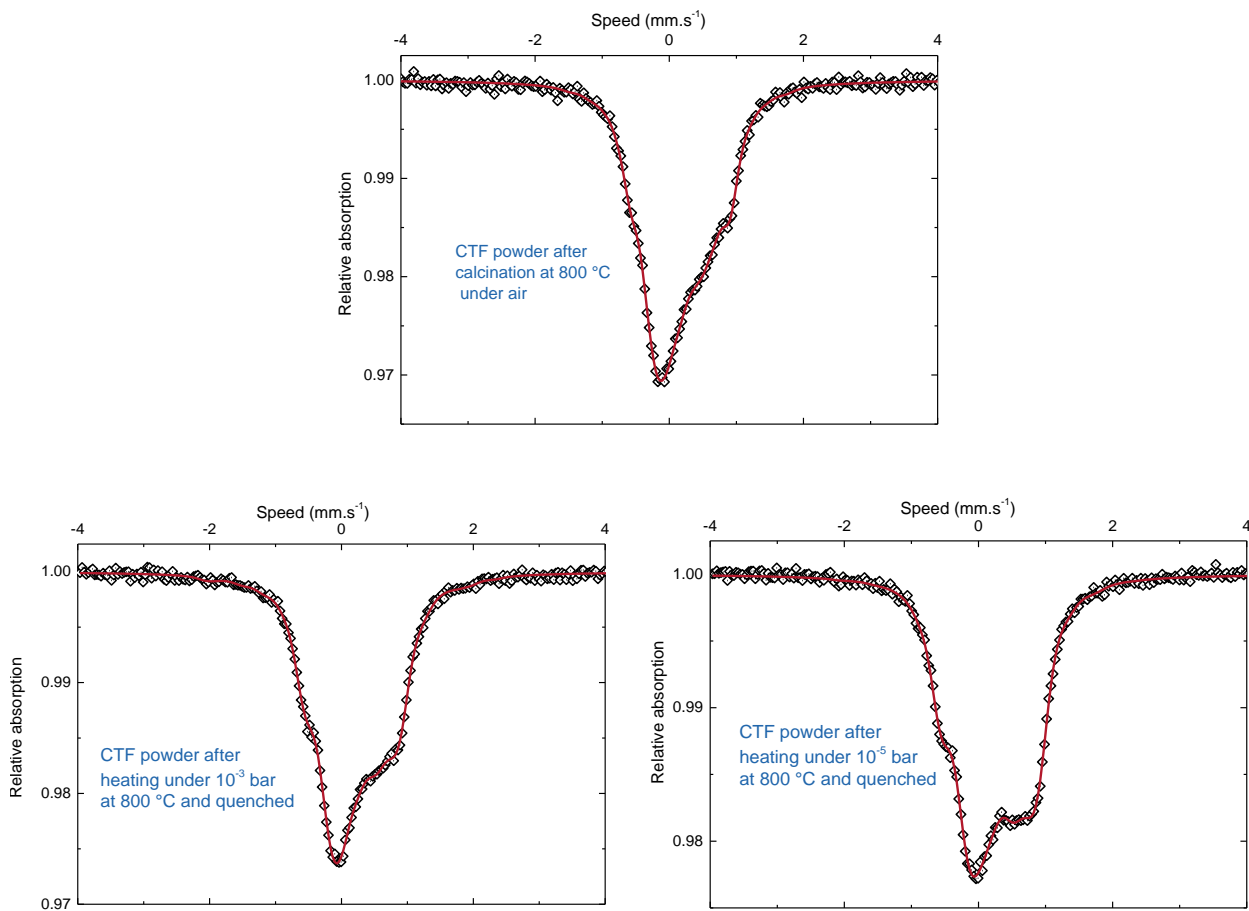


Figure 19: Mössbauer spectra on the starting fired powder, after heating under 10^{-3} bar at 800 °C and quenched and after heating under 10^{-5} bar at 800 °C and quenched.

Figure 19 showed the evolution of the Mössbauer spectra performed on the starting fired powder, on a powder after heating under 10^{-3} bar at 800 °C and quenched, and heating under 10^{-5} bar at 800 °C and quenched. It is difficult to quantify precisely but it can be seen that the general shape of the spectrum evolves and the estimated $\text{Fe}^{\text{IV}}/\text{Fe}^{\text{III}}$ ratio decreases with decreasing the oxygen partial pressure at which the thermal treatment was performed.

There were still few percent of Fe^{IV} in the powder after treatment at 10^{-5} bar and no Fe^{II} , meaning that, at least, δ will change from 0.04 under air to slightly less than 0.05. So the number of oxygen vacancy changed from 4% under air to 5% under 10^{-5} bar (partial pressure close to the one where the ionic conductivity was measured by impedance spectroscopy). This change of oxygen vacancy concentration alone cannot explain the factor 1.6 between the ionic conductivity values.

However, the Mössbauer spectra gave also information on the disorder around the iron (an important disorder is found for the 3 samples) and on the coordination of the iron. The evolution of the shape of the spectra is also linked to the evolution of the coordination around the iron. This change of coordination could induce a change in the mobility and then explain the difference in ionic conductivity.

Consequently, it can be concluded that the ionic conductivity is not constant as a function of P_{O_2} , and the measurement from impedance spectroscopy can be used to estimate the evolution of the ionic conductivity as a function of P_{O_2} . Indeed, it was assumed that the ionic conductivity under air was equal to the one obtained via isotopic exchange. Using the total conductivity measured by impedance spectroscopy, it was then possible to calculate the electronic conductivity under air. It was assumed that the electronic

conductivity for P_{O_2} higher than 10^{-6} bar was only due to electron hole conductivity and then, using the fact that the electron hole conductivity is proportional to $P_{O_2}^{1/4}$, it was possible to calculate the electron holes conductivity for all P_{O_2} . Finally, using the total conductivity measured by impedance spectroscopy and the electron hole conductivity calculated, it was possible to assume the ionic conductivity as a function of P_{O_2} (Figure 20).

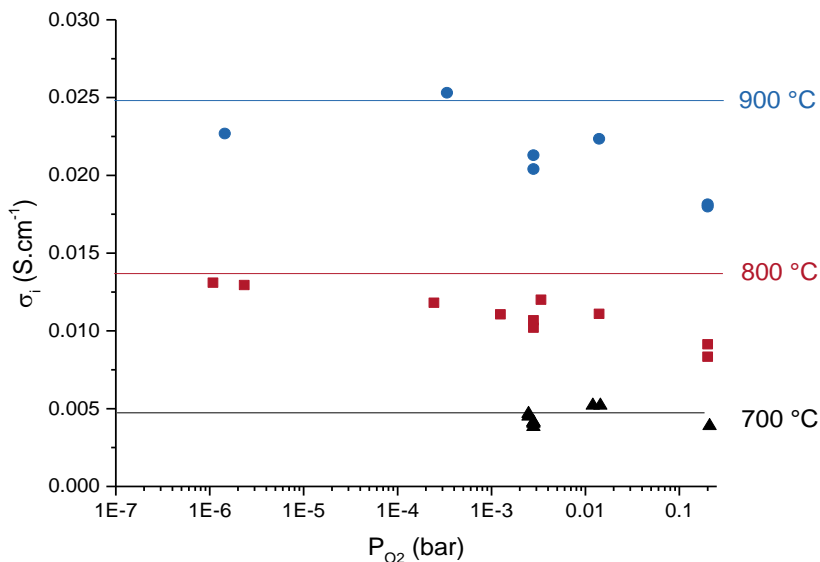


Figure 20: Ionic conductivity as a function of P_{O_2} , calculated from ionic conductivity under air calculated by isotopic exchange and total conductivity from impedance spectroscopy. Horizontal lines represent the ionic conductivity obtained by impedance spectroscopy under a P_{O_2} between 10^{-15} and 10^{-5} bar.

From Figure 20, a general trend can be concluded. The ionic conductivity under air is lower than under lower P_{O_2} , and increases with decreasing P_{O_2} . It seems to have a plateau at low P_{O_2} , close to the value of the ionic conductivity found by impedance spectroscopy under a P_{O_2} between 10^{-15} and 10^{-5} bar .

5. Conclusion

The total conductivity of CTF was studied as a function of P_{O_2} by impedance spectroscopy. It was found that the CTF was a mixed conductor with an ionic transport number, t_i , which increased with temperature. A simple defect model was applied to the CTF and the activation energies of ionic, electron and electron hole conductivities were calculated. The electronic conductivities were assumed to follow the small polaron mechanism with an activation energy equal to 0.57 eV for the electron hole conductivity and 2.6 eV for the electron conductivity. An activation energy of 0.94 eV was calculated for ionic conductivity. But these calculations were made assuming that the ionic conductivity was constant over a wide range of P_{O_2} .

However, it is known that the valence of the iron of CTF may change as a function of P_{O_2} . The oxygen non-stoichiometry was then investigated and it was found that, under atmospheric partial pressure, around 20% of the iron were Fe^{IV} , meaning that $\delta = 0.04$. After reduction with 3% H_2/Ar at 600 °C, no more Fe^{IV} were present ($\delta = 0.05$). The presence of metallic iron was found after reduction at a temperature higher than 800 °C. After 1 h of reduction with 3% H_2/Ar at 1000 °C, around 27% of metallic iron were found (quantification performed on TGA and TPR measurements).

Considering that $\delta = 0.04$ under air, ionic conductivity was calculated with the results of isotopic exchange. These results were compared to the one obtained by impedance spectroscopy. The same activation energy was found (≈ 0.9 eV) but results obtained by impedance spectroscopy were up to 1.6 times higher than thus obtained by isotopic exchange. This can be explained by the fact that the ionic conductivity obtained by impedance spectroscopy was calculated between 10^{-15} - 10^{-5} bar, while it was obtained under air for the other methods. The concentration of oxygen vacancy is then higher (5% instead of 4%) but these small difference alone cannot explain the factor 1.6. The change of iron coordination observed by Mössbauer spectroscopy while decreasing the P_{O_2} may induce a change of oxygen vacancy mobility which lead to this change in ionic conductivity.

Finally, it was then concluded that the ionic conductivity was not constant between 10^{-15} and 1 bar. The ionic conductivity as a function of P_{O_2} was assumed between 10^{-6} and 0.2 bar (via the results of total conductivity obtained by impedance spectroscopy and ionic conductivity under air obtained by isotopic exchange). The ionic conductivity was the lowest under air and increased while P_{O_2} decreased to stabilize in a plateau close to the value calculated with impedance spectroscopy between 10^{-15} - 10^{-5} bar.

- [1] M. van den Bossche, Oxygen vacancy ordering in iron-doped calcium titanate, *Utwente.nl*. (2005).
- [2] T. Bieger, J. Maier, R. Waser, Optical investigation of oxygen incorporation in SrTiO_3 , *Solid State Ionics*. 53–56 (1992) 578–582.
- [3] A.A.L. Ferreira, J.C.C. Abrantes, J.R. Jurado, J.R. Frade, Oxygen stoichiometry of $\text{Sr}_{0.97}(\text{Ti,Fe})\text{O}_{3-\delta}$ materials, *Solid State Ionics*. 135 (2000) 761–764.
- [4] S. Marion, A.I. Becerro, T. Norby, Ionic and electronic conductivity in $\text{CaTi}_{1-x}\text{Fe}_x\text{O}_{3-\delta}$ ($x=0.1-0.3$), *Ionics (Kiel)*. 5 (1999) 385–392.
- [5] L.A. Dunyushkina, A.V. Kuz'min, V.B. Balakireva, V.P. Gorelov, Electrical conduction nature and phase transition in $\text{CaTi}_{1-x}\text{Fe}_x\text{O}_{3-\delta}$ ($x = 0.1-0.5$), *Russ. J. Electrochem.* 42 (2006) 375–380.
- [6] L.A. Dunyushkina, V.P. Gorelov, High temperature electrical behavior of $\text{CaTi}_{1-x}\text{Fe}_x\text{O}_{3-\delta}$ ($x=0-0.5$). Oxygen-ion, electronic and proton conductivity, *Solid State Ionics*. 253 (2013) 169–174.
- [7] S. Xie, W. Liu, K. Wu, P.H. Yang, G.Y. Meng, C.S. Chen, Mixed oxygen ionic and electronic conduction in $\text{CaFe}_{0.2}\text{Ti}_{0.8}\text{O}_{3-\delta}$: a combined oxygen permeation and electrical conductivity study, *Solid State Ionics*. 118 (1999) 23–28.
- [8] M. Balaguer, S. Escolástico, J.M. Serra, Oxygen permeation and stability of $\text{CaTi}_{0.73}\text{Fe}_{0.18}\text{Mg}_{0.09}\text{O}_{3-\delta}$ oxygen-transport membrane, *J. Memb. Sci.* 524 (2017) 56–63.
- [9] J.M. Polfus, W. Xing, M.F. Sunding, S.M. Hanetho, P.I. Dahl, Y. Larring, M.-L. Fontaine, R. Bredesen, Doping strategies for increased oxygen permeability of CaTiO_3 based membranes, *J. Memb. Sci.* 482 (2015) 137–143.
- [10] D. Marrocchelli, S.R. Bishop, H.L. Tuller, B. Yildiz, Understanding chemical expansion in non-stoichiometric oxides: Ceria and zirconia case studies, *Adv. Funct. Mater.* 22 (2012) 1958–1965.
- [11] H. Tuller, S. Bishop, Point defects in oxides: tailoring materials through defect engineering, *Annu. Rev. Mater. Res.* 41 (2011) 369–398.
- [12] V.V. Kharton, F.M. Figueiredo, A.V. Kovalevsky, A.P. Viskup, E.N. Naumovich, J.R. Jurado, J.R. Frade, Oxygen Diffusion in, and Thermal Expansion of, $\text{SrTiO}_{3-\delta}$ -and $\text{CaTiO}_{3-\delta}$ -Based Materials, *Defect Diffus. Forum.* 186–187 (2000) 119–136.
- [13] L.W. Tai, M.M. Nasrallah, H.U. Anderson, D.M. Sparlin, S.R. Sehlin, Structure and electrical properties of $\text{La}_{1-x}\text{Sr}_x\text{Co}_{1-y}\text{Fe}_y\text{O}_3$. Part 1. The system $\text{La}_{0.8}\text{Sr}_{0.2}\text{Co}_{1-y}\text{Fe}_y\text{O}_3$, *Solid State Ionics*. 76 (1995) 259–271.
- [14] F.M. Figueiredo, J. Waerenborgh, V.V. Kharton, H. Näfe, J.R. Frade, On the relationships between structure, oxygen stoichiometry and ionic conductivity of $\text{CaTi}_{1-x}\text{Fe}_x\text{O}_{3-\delta}$ ($x=0.05, 0.20, 0.40, 0.60$), *Solid State Ionics*. 156 (2003) 371–381.
- [15] L.A. Dunyushkina, V.A. Gorbunov, Effect of Crystal Structure on the Electrical Properties, 37 (2001) 1165–1169.
- [16] A.A. Murashkina, A.N. Demina, A.K. Demin, V.I. Maragou, P.E. Tsiakaras, The influence of Fe, Cu, Al - doping on the crystal structure, thermal and electrical properties of calcium titanate, *Solid State Ionics*. 179 (2008) 1615–1619.

CHAPTER 6

CTF

STABILITY

Papa dit que nous avons une fausse idée de la stabilité. Que la stabilité pour nous c'est rester sans bouger. Alors qu'être stable c'est être stable dans le mouvement.

Milena Agus (Quand le requin dort)

Table of content

| | |
|--|-----|
| 1. Introduction..... | 114 |
| 2. Aging and stability under non-reactive atmosphere..... | 115 |
| 3. Aging under reactive gases..... | 118 |
| 3.1 Under CO/CO ₂ | 118 |
| 3.2 Experiment under wet CO ₂ | 123 |
| 3.3 Hydrothermal treatment..... | 126 |
| 3.4 Effect of H ₂ | 128 |
| 3.5 Oxidation of methane..... | 128 |
| 4. Redox stability potential..... | 134 |
| 4.1 Basic principle..... | 134 |
| 4.2 Electrochemical reduction (Pt electrode)..... | 135 |
| 4.3 Chemical reduction by hydrogen (Pt electrode)..... | 135 |
| 4.4 Chemical and electrochemical reduction using iron electrode..... | 136 |
| 4.5 First synthesis of the results..... | 137 |
| 5. Conclusion | 138 |

1. Introduction

As explained in chapter 1, the long-term stability is critical for industrial application. Indeed, for integrated OTM in carbon capture and storage plant or for use as catalytic membrane reactor, the membrane is surrounding with reactive atmospheres. The presence of pollutant in the plant, or fluxes of CO₂ and CH₄ may damage the membrane. Long-term experiment on high flux OTM (for example BSCF) showed important degradation, i.e. presence of a carbonate layer on the surface of the membrane preventing any oxygen diffusion or segregation of some components from the OTM. The material can also be reduced, changing the flux performance of the membrane [1–8]. European programs such as MEM-Brain or Green-CC, finance studies on stable new ceramics [9–11]. Previous studies showed that CTF has a better chemical stability than most other materials [12–14] but long term experiments under reactive atmospheres such as CO₂ and CH₄ were not performed yet.

In this chapter, long-term semi-permeation experiments were performed under non-reactive atmospheres but also under CO₂, H₂ and CH₄. For all experiments (unless otherwise stated), the oxygen-rich side was flowed with air and the atmosphere was changed on the lean side.

2. Aging and stability under non-reactive atmosphere.

Semi-permeability measurements were performed on CTF10 pellets. It is worth noting that during the experiments, the membrane endured temperature cycles from 600 °C to 950 °C and various P_{O_2} on the sweep side (from 10^{-4} bar to 1 bar).

Oxygen semi-permeability versus time curves of different CTF pellets are plotted in Figure 1 for different temperatures (700 to 900 °C) under non-reactive atmosphere (air on the oxygen-rich side and argon on the lean side).

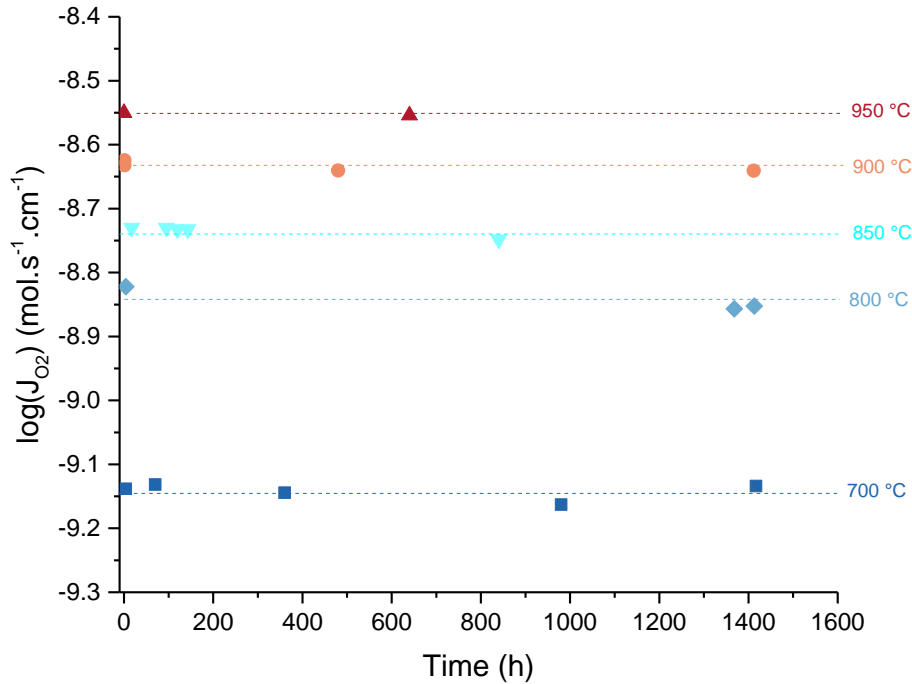


Figure 1: Oxygen semi-permeability as a function of time for different temperatures of different CTF pellets tested under air on the oxygen-rich side and argon on the lean side.

Results show a good stability under air: after more than 1000 hours, the semi-permeability flux remains almost the same (maximum difference: 6%). For BSCF at 800 °C, after 1000 hours, already a 64% decrease of the semi-permeability flux has been observed [1], and it is of 87% for CGO-LSM [15] (Figure 2). Interestingly, initial J_{O_2} of CGO-LSM is higher than that of CTF, but is actually lower by 50% after 800 h at 800 °C.

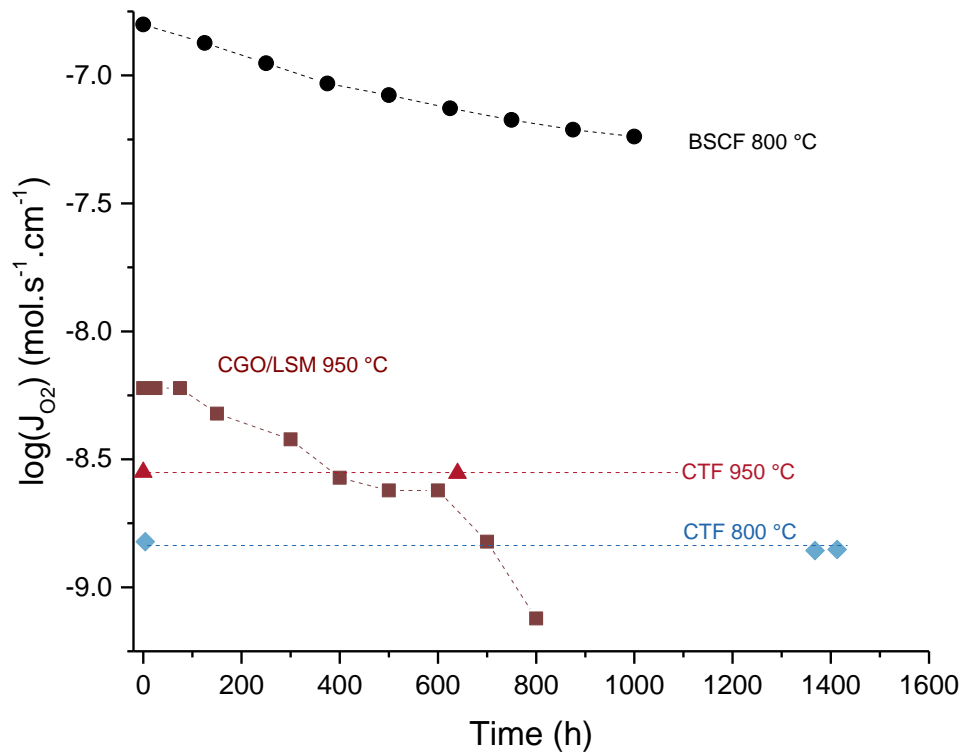
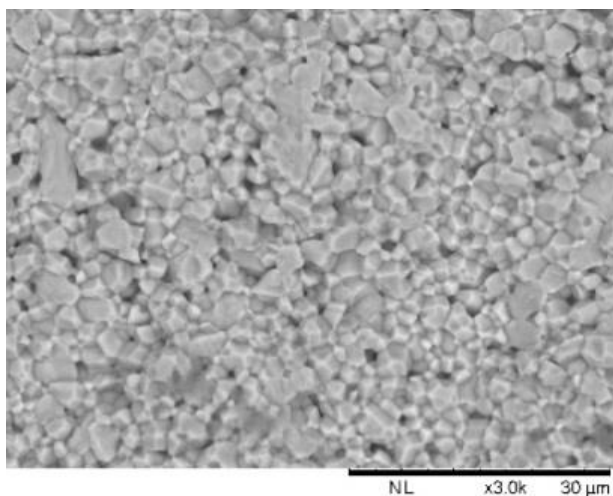


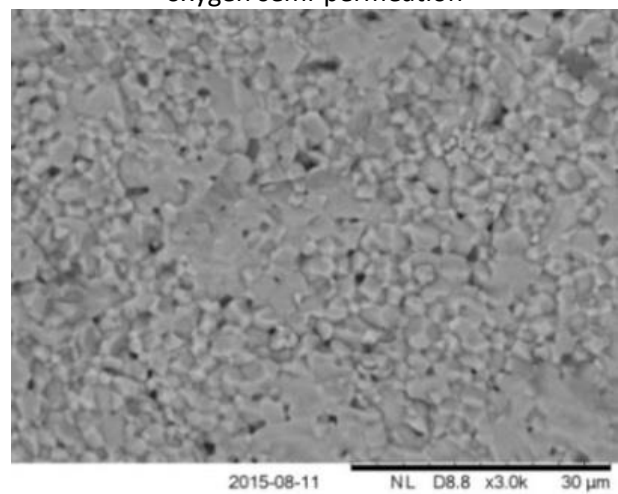
Figure 2: J_{O_2} (air as sweep gas) as a function of time for different membrane materials.

SEM was used to observe the fracture surface of membranes after several hundred hours of semi-permeation and to check if any change in grain size and/or chemical composition happen within the bulk. Indeed, for BSCF membrane for instance, secondary phases appear after thousand hours of oxygen semi-permeation. Phases enriched in cobalt, as well iron deficiency in some phases are observed [1]. In the CTF membrane post semi-permeation, no differences with a pristine membrane are found (no element segregation is visible, same average grain size) and the same morphology is found across the pellets, from the lean to the rich-side (Figure 3).

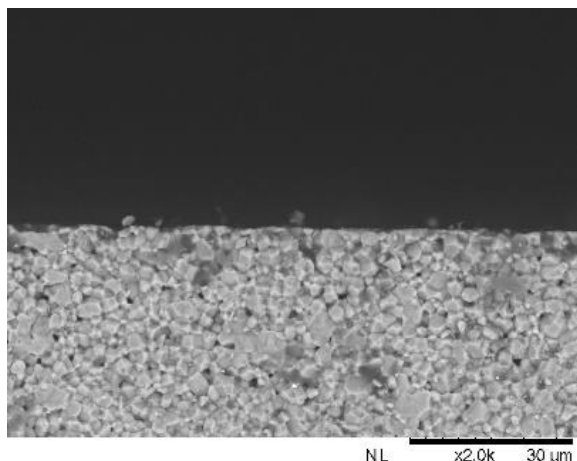
Pristine CTF membrane



CTF Membrane after several hundred hours of oxygen semi-permeation



Pristine membrane



Membrane after several hundred hours of oxygen semi-permeation

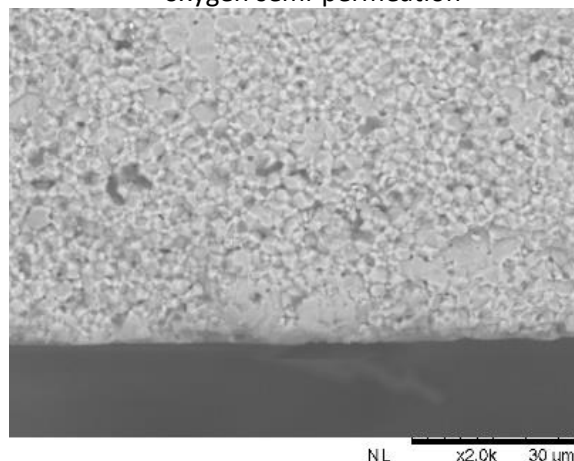


Figure 3: SEM images comparing a pristine CTF membrane (left) with a CTF membrane submitted to several hundred hours of semi-permeation (air/argon gradient).

No degradation is visible after thousands hours of oxygen semi-permeation under non-reactive atmosphere. However, for several applications, reactive atmospheres such as CO_2 or CH_4 in presence or not of water are used (cf. chapter 1 §2). Consequently, the long-term semi-permeability of the CTF membrane under these conditions was investigated.

3. Aging under reactive gases

3.1 Under CO/CO₂

It is well known that the presence of alkaline earth metals in a perovskite structure will induce a poor CO₂ resistance [16–19]. Indeed, the acidic character of CO₂ may react with the perovskite (and especially with the alkaline earth metals). It can induce formation of carbonates, either on the surface or even in the bulk phase. This will quickly decrease the oxygen semi-permeation performances but it can be reversible if the carbonates are only adsorbed on the membrane surface. Regarding the microstructure, it can induce structural decomposition and microstructure erosion. Moreover, CO₂ can be adsorbed on the membrane surface and competes with oxygen. This will also decrease the oxygen semi-permeation but it is totally reversible when no more CO₂ is present.

The presence of CO has a similar effect to that of CO₂ because it can be oxidized to form CO₂. Consequently, it is not possible to measure the oxygen partial pressure with the oxygen gauge on the lean side in the presence of CO. Moreover, some carbon can be formed, according to the Boudouard reaction.

The CTF membrane was exposed to CO/CO₂ for 170 hours at 850 °C. The oxygen semi-permeability was continuously measured and is plotted in Figure 4. The semi-permeation remains constant during this experiment, indicating no degradation on these conditions.

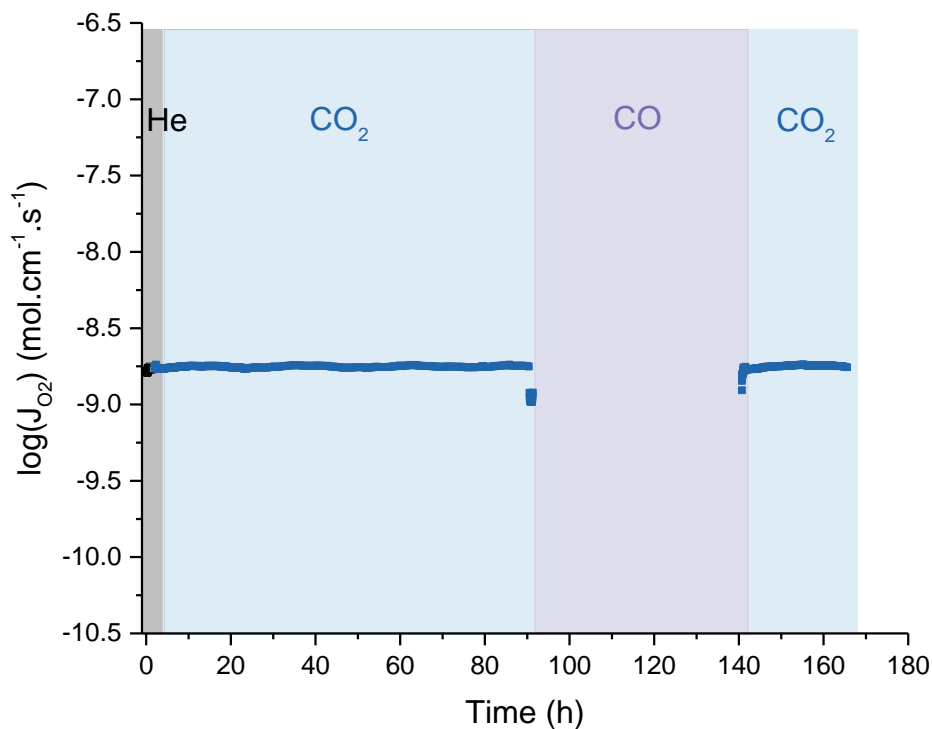


Figure 4: Oxygen semi-permeability of CTF as a function of time under CO₂ and CO on the lean side, at 850 °C.

Another experiment was performed with a measurement of the oxygen partial pressure closer to the membrane, using a commercial equipment, consisting of a tiny YSZ sensor with an internal reference system (MicroPoas, SETNAG), which was located in the inner chamber just below the pellet (Figure 5 and Figure 6).



Figure 5: Commercial O₂ sensor (MicroPoas, SETNAG).

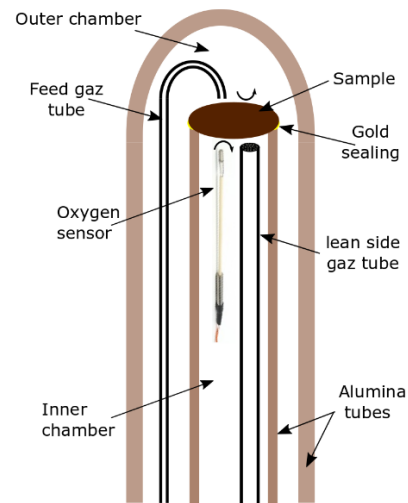


Figure 6: Semi-permeability setup.

Oxygen partial pressure calculated with O₂ sensor in proximity of the sample is presented in Figure 7. Only measurements at defined temperatures were reported here, but a wide range of temperature (from 550 to 900 °C) were screened during the experiment. Different atmospheres were tested on the lean side. After 170 hours under helium, the atmosphere was switched to CO₂ during 200 hours without modification of the oxygen partial pressure.

During the 100 following hours, some issues on the setup did not allow to flow gases to the membrane. When helium was again used, the oxygen partial pressures measured with the oxygen sensor were lower than the former one by - 19%. Then, atmosphere was changed to CO for 100 hours. After these 100 hours (that means more than 500 hours after the beginning), atmosphere was switched to CO₂ and the same oxygen partial pressure than before CO introduction was recovered. During 150 hours, the oxygen partial pressure slightly improves but still remains lower than before the “cut-off period”. Another maintenance period was necessary during around 200 hours; then, atmosphere was switched again to CO₂. The first measurements were very low but after a stabilization time, the oxygen partial pressure after 150 more hours (that means 1000 hours after the beginning) were almost the same than at the beginning. Finally, atmosphere was changed to helium and the same oxygen partial pressure was recovered (- 3% compared to the initial one).

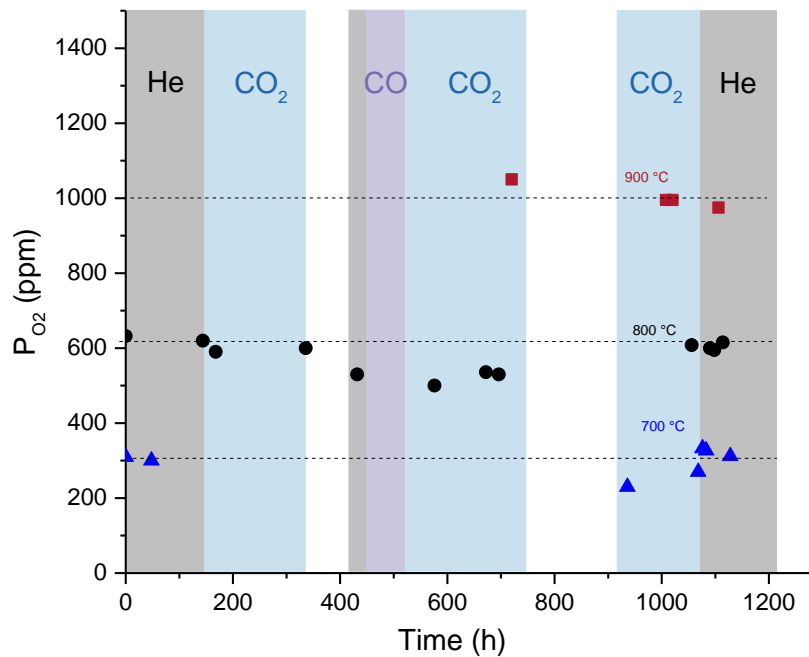


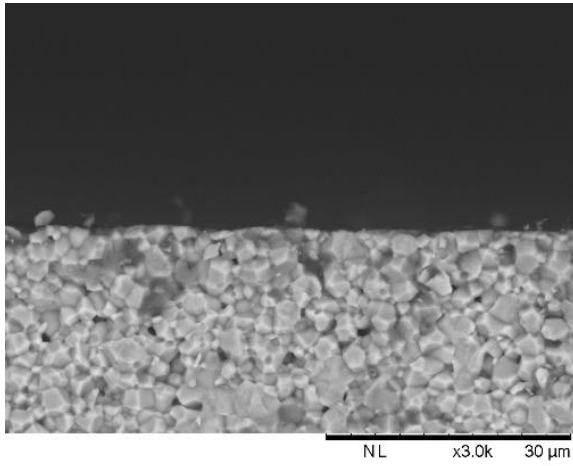
Figure 7: Oxygen partial pressure, measured using an oxygen sensor close to the surface of the CTF pellet, as a function of time under He, CO₂ and CO on the lean side.

The oxygen partial pressures measured with the commercial oxygen sensor are higher than the previous one measured with the oxygen gauge ($P_{O_2} \sim 630$ ppm vs 500 ppm at 800 °C i.e. a difference of 20%) but it is normal knowing that the measurement was made closer to the membrane with the commercial oxygen sensor. Indeed, there is a gradient of oxygen partial pressure near the surface, and with the MicroPoas it is possible to measure what is called $P_{O_{2,n,s}}$ [20] the oxygen partial pressure near the surface.

Post-mortem SEM and XRD analyses were done on the sample to study the effect of the reactive gases on the surface aspect and the microstructure of the membrane. When CO₂ atmosphere reacts with the membrane a tarnish layer can be observed on SEM due to accumulation of some elements and exhaustion of others [16]. A porous layer can also be present, constituted mainly of carbonates [21,22]. SEM pictures of a fracture surface of a CTF pristine membrane and a membrane after semi-permeation under CO/CO₂ are represented in Figure 8. The grain size and the porosity remain roughly the same than on the pristine membrane. EDS measurements did not show any significant differences between the oxygen rich side, the oxygen lean side and the middle of the membrane after semi-permeation ageing tests (Figure 9 and Figure 10).

There are no visible differences between the pristine membrane and the membrane after the semi-permeation.

Pristine CTF membrane



CTF membrane after thousand hours of oxygen semi-permeation under CO₂

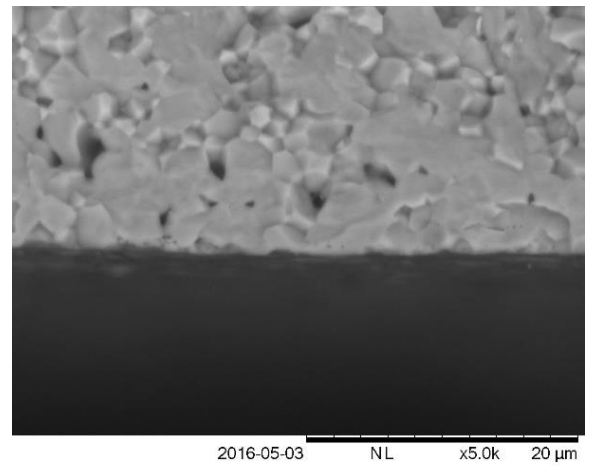
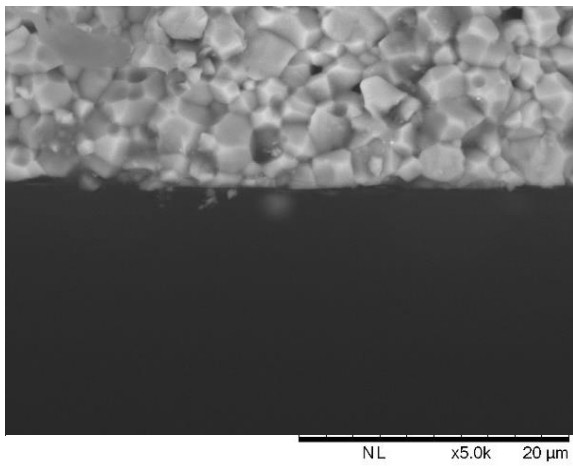
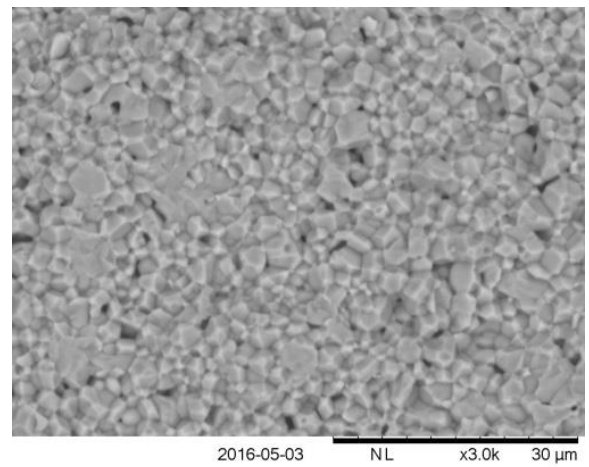
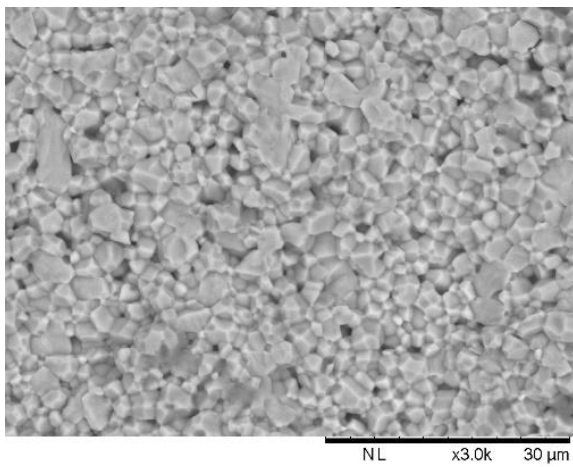
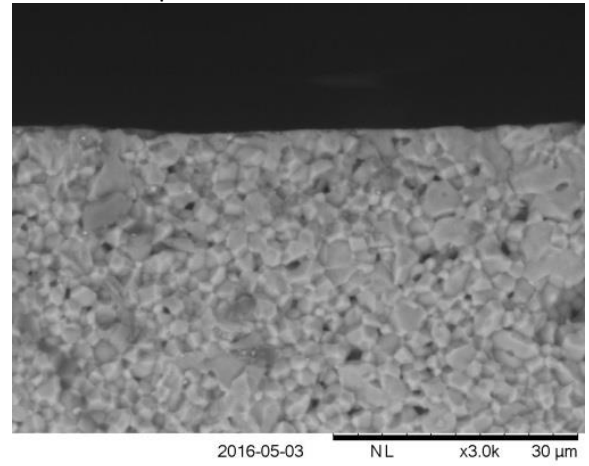


Figure 8: SEM images comparing a pristine membrane (left) with another membrane submitted to more than thousand hours under CO₂ and CO on the lean side (right).

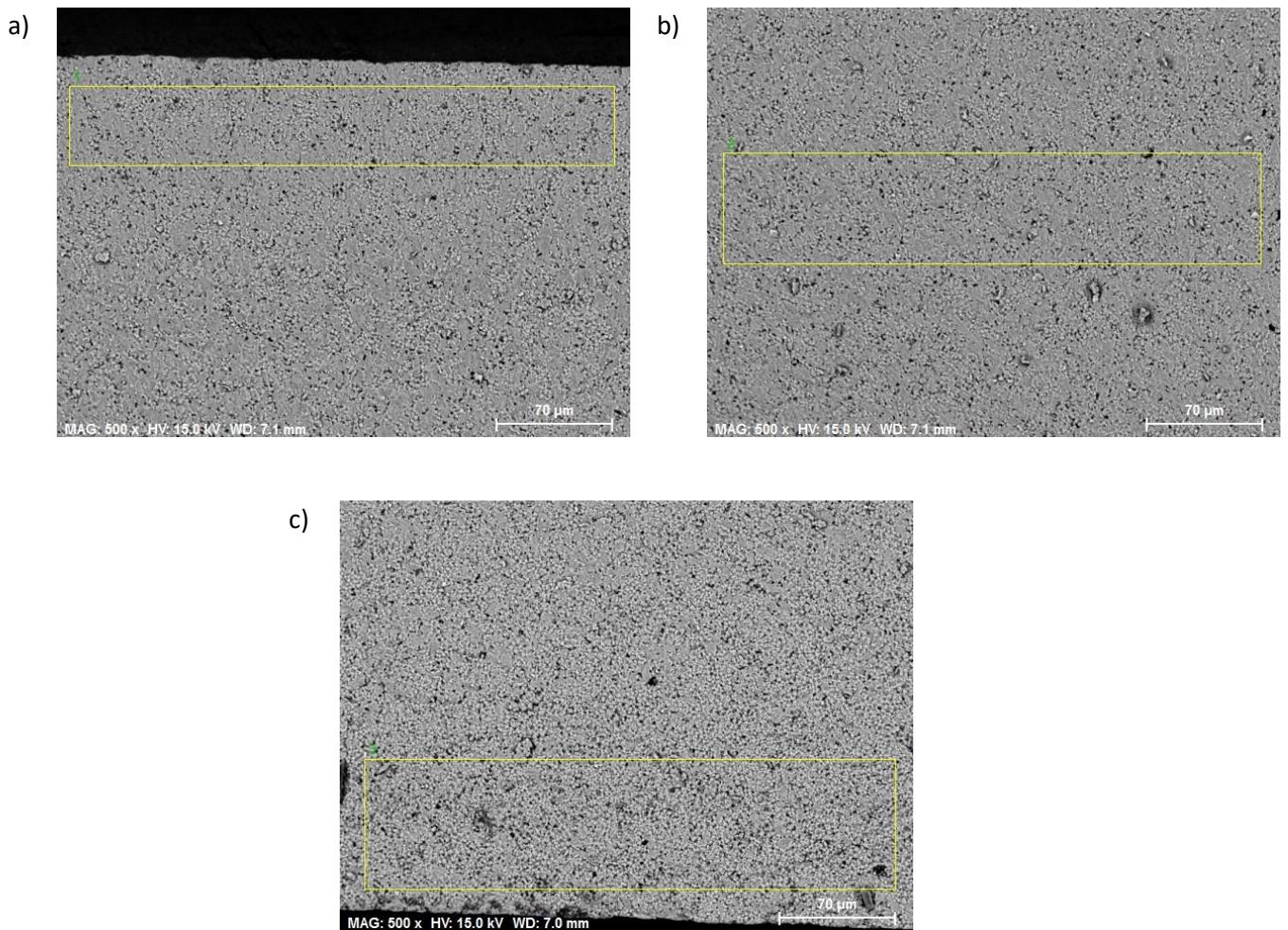


Figure 9: SEM images delimiting the area where EDS measurements were performed on the membrane submitted to more than thousand hours under CO₂ and CO on the lean side. a) Oxygen rich side of the pellet, b) middle of the pellet c) oxygen lean side.

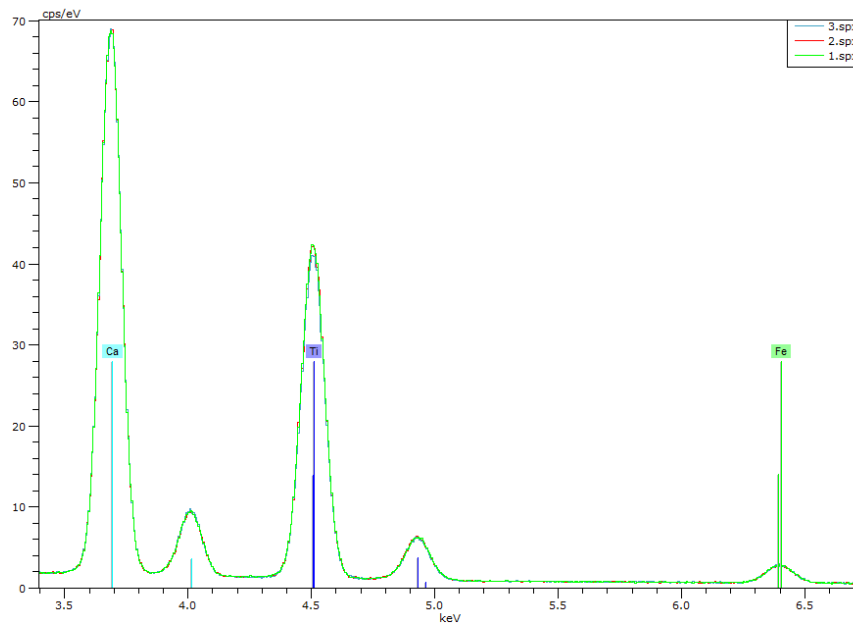


Figure 10: X-ray spectra of the pellet on the three areas: on the lean side, on the center and on the rich side of the membrane. The same calcium, titanium and iron peaks are visible.

The XRD patterns on the membrane after semi-permeation under CO and CO₂ are very similar to the one of a fired CTF pellet and no additional phases are indexed (Figure 11), confirming that the CO and CO₂ send during the semi-permeation did not affect the membrane crystal phase composition, within the XRD accuracy.

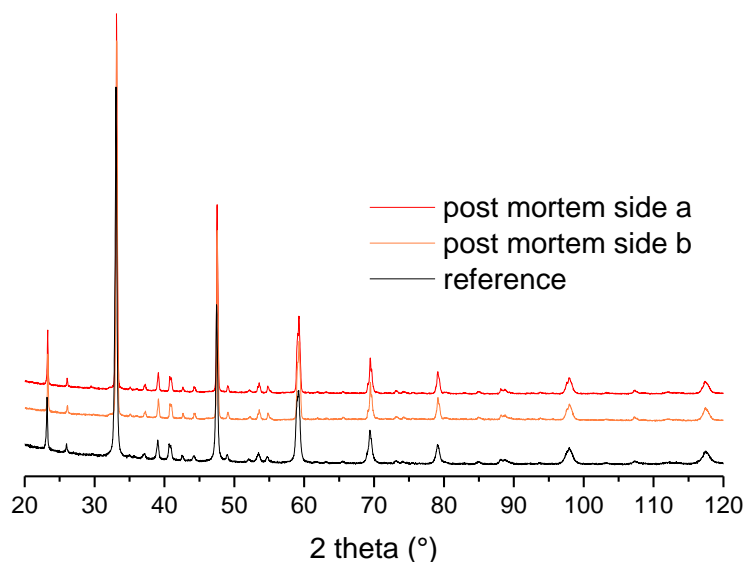


Figure 11: Normalized XRD patterns of reference sample and both sides of the pellet after the semi-permeation under CO/CO₂.

We can thus conclude that the CTF is not degraded under 1% CO₂ and 2% CO after 1200 hours.

3.2 Experiment under wet CO₂

It is known that the adsorption of CO₂ on the surface of a perovskite is promoted in presence of water vapor [23]. Moreover, if CO₂ and H₂O are in contact simultaneously with the membrane, bicarbonate (HCO₃⁻) may be formed [24].

The influence of CO₂ and water vapor on the semi-permeation was studied (Figure 12). After more than 600 hours under He or CO₂, or CO, with no degradation on the semi permeation flux, H₂O was added in the flowing gas simultaneously with the CO₂ flux, during 200 hours (there was a break during 30 h due to empty gas tank). Performances continuously decreased from 1.76×10^{-9} mol.cm⁻¹.s⁻¹ to 1.12×10^{-9} mol.cm⁻¹.s⁻¹ and seems to stabilize. There was thus a decrease of around 35% of semi-permeation flux during 200 hours.

However, when returning under dry helium, the semi-permeability flux increased and after \approx 100 hours of annealing, the semi-permeation flux was similar to initial values.

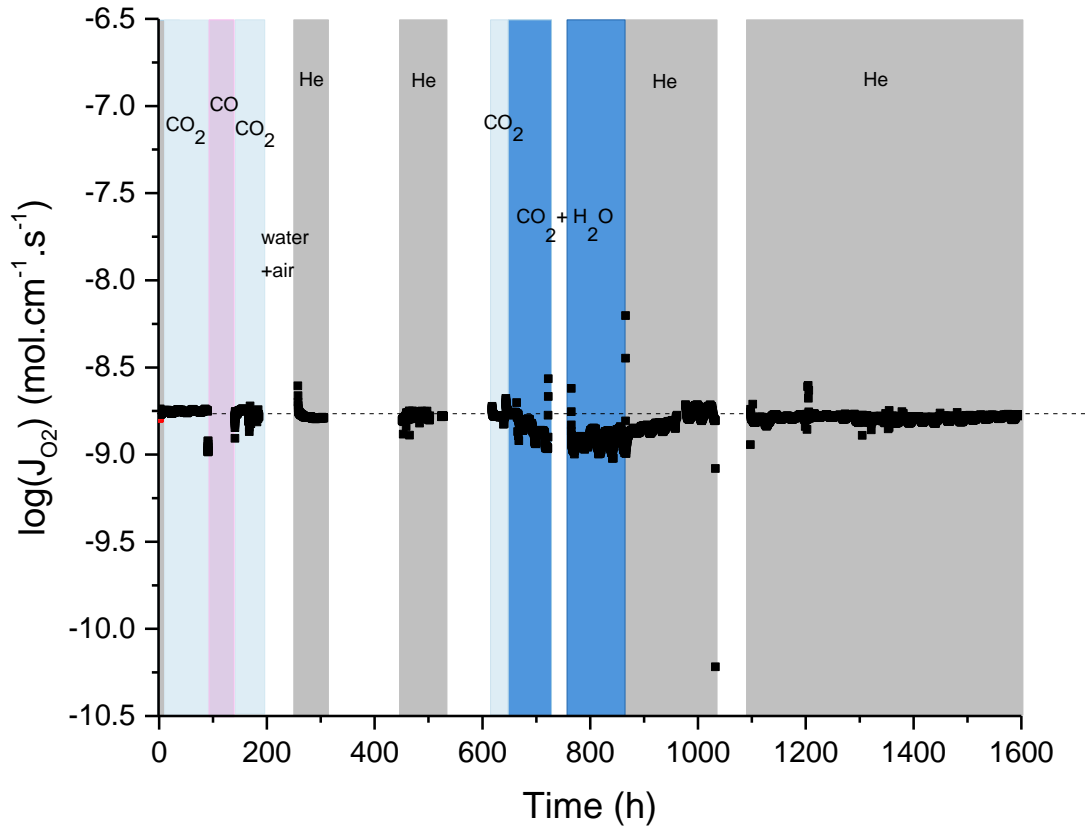
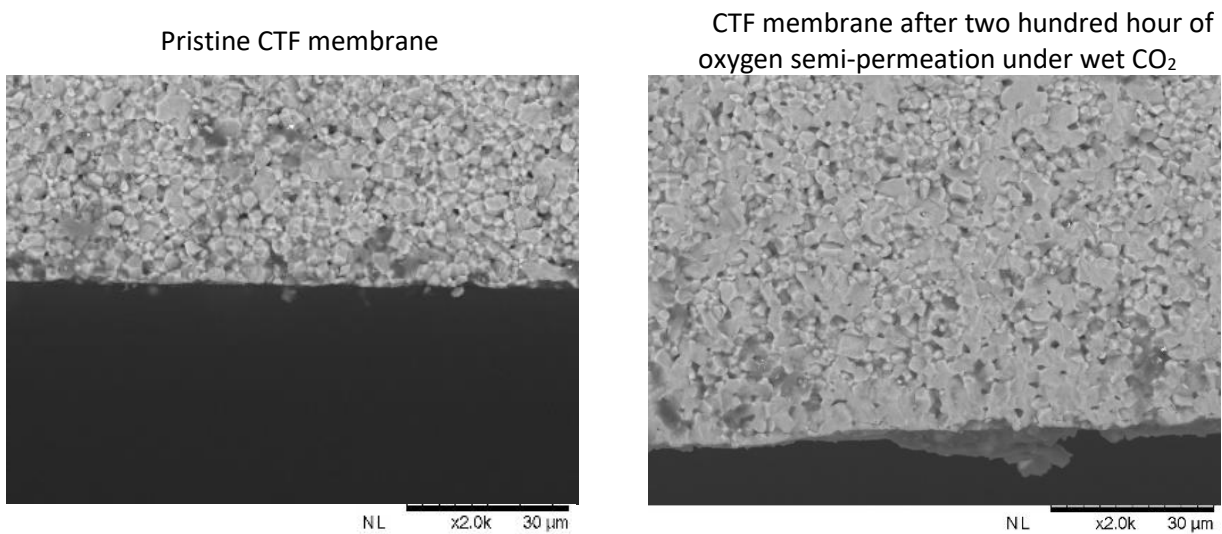


Figure 12: Oxygen semi-permeability flux as a function of time under dry and wet CO₂ on the lean side at 850 °C.

SEM images of a fracture surface of a CTF pellets after semi-permeation under dry and wet CO₂ are represented in Figure 13. The grain size and the porosity remain roughly the same than on the pristine membrane. There are no visible differences between the pristine membrane and the membrane after the semi-permeation, meaning that the degradation of the flux observed under wet CO₂ was not a bulk degradation.



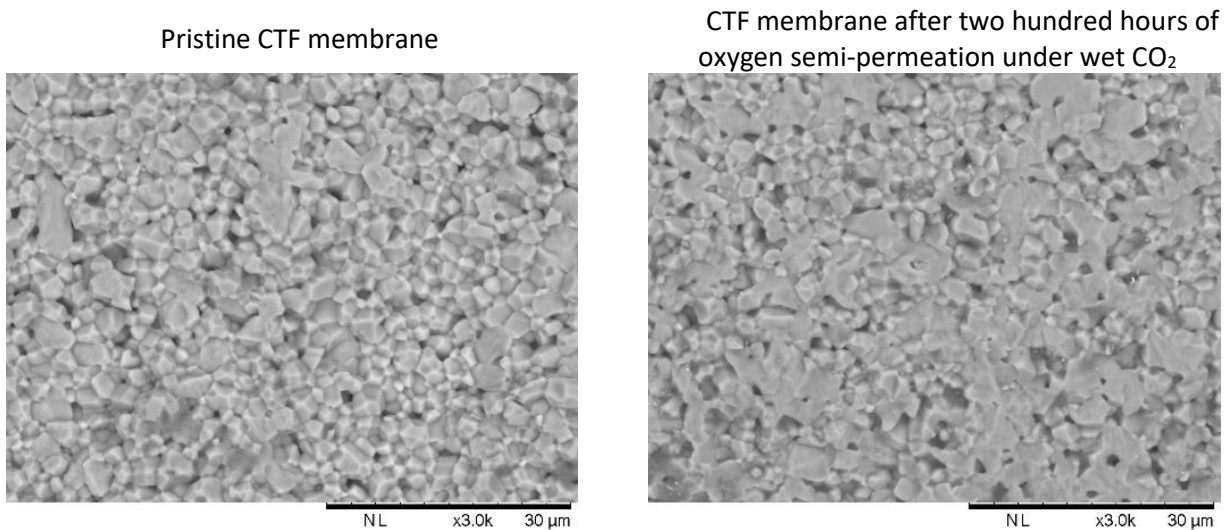


Figure 13: SEM images comparing a pristine membrane (left) with another membrane submitted two hundred hours under wet CO₂ on the lean side (right).

The XRD pattern on the membrane after semi-permeation under wet CO₂ is very similar to the one of a pristine CTF pellet and no additional phases are indexed (Figure 14). There is a slight shift of all the diffractogram toward the high angles (+ 0.15°) due to a change in the angle of the sample during the acquisition.

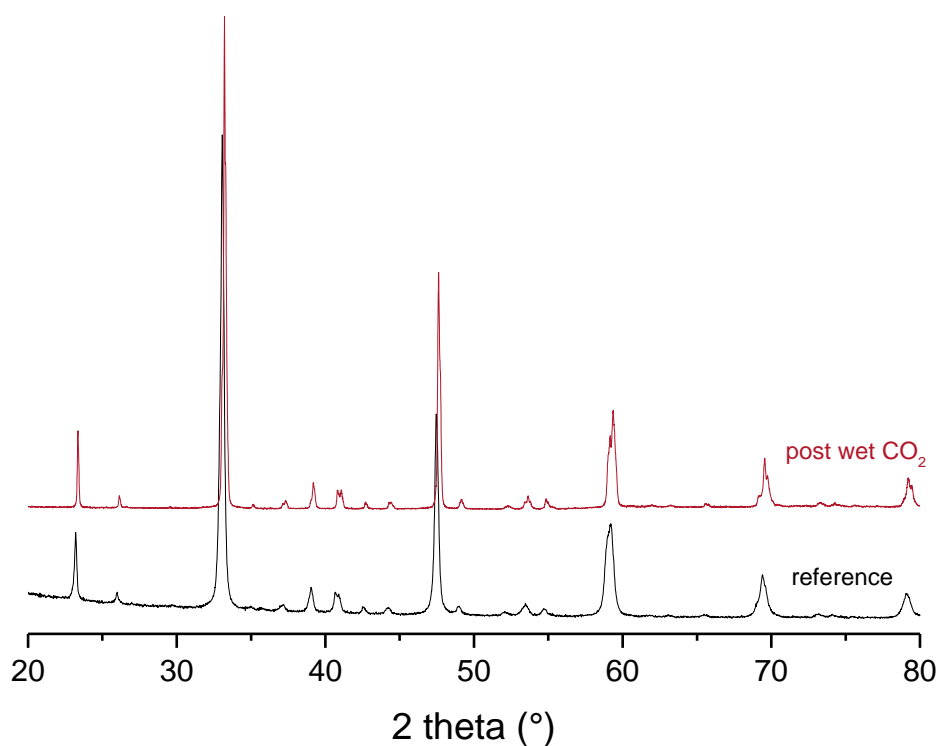


Figure 14: Normalized XRD patterns of a reference sample and the pellet after the semi-permeation under wet CO₂.

Consequently, the degradation (- 40% oxygen semi-permeability flux) observed when wet CO₂ was sent seemed totally reversible. Indeed, the XRD pattern and the SEM pictures did not show any degradation and the semi-permeation flux was totally recovered under helium sweeping. This degradation observed under wet CO₂ is then either a surface degradation which was removed when helium was sent or a competition between the oxygen activity and the adsorption of other compounds (carbonates for instance).

3.3 Hydrothermal treatment

It has been shown in Section 2.2 that the combination of vapor and CO₂ affects the flux through the CTF membrane, in a reversible way. It can be due to the combination of water vapor and CO₂ or it can be due to the effect of water vapor by itself. To test the effect of water vapor on the CTF pellet, a hydrothermal treatment was carried out on the sintered pellets at 800 °C during one week with 5 vol% of water in a reconstituted air flow.

SEM, XRD and impedance spectroscopy studies were performed after the hydrothermal treatment to investigate the effect of water vapor on a CTF pellet.

SEM pictures of a fracture surface are represented in Figure 15. The grain size and the porosity remain roughly the same than on the pristine membrane. There are no visible differences between pristine membrane and the membrane after the hydrothermal treatment.

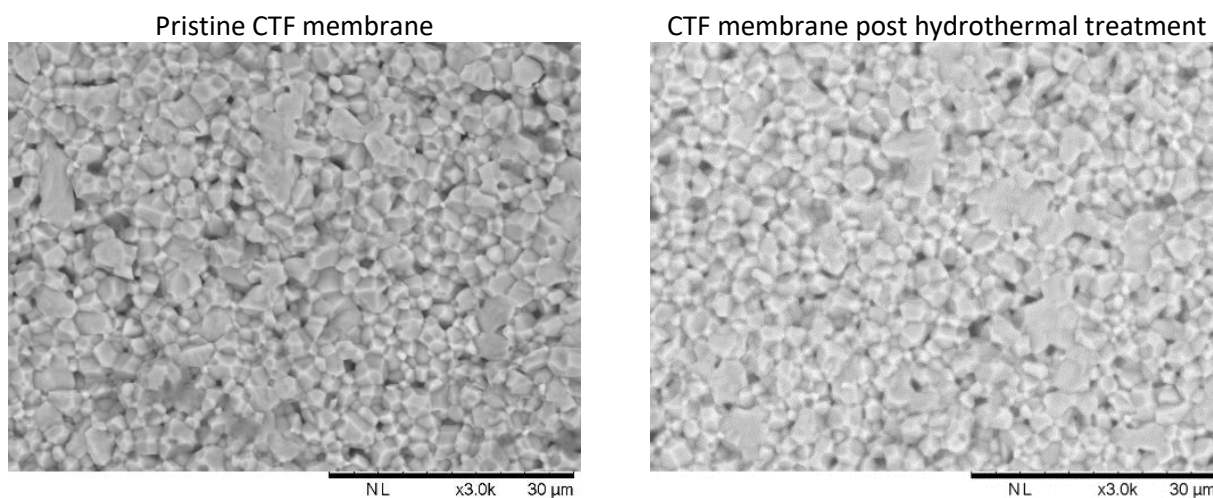


Figure 15: SEM images comparing a pristine membrane (left) with another membrane after a hydrothermal treatment (right).

The XRD pattern on the membrane after hydrothermal treatment is very similar to the one of a pristine CTF pellet and no additional phases are indexed (Figure 16).

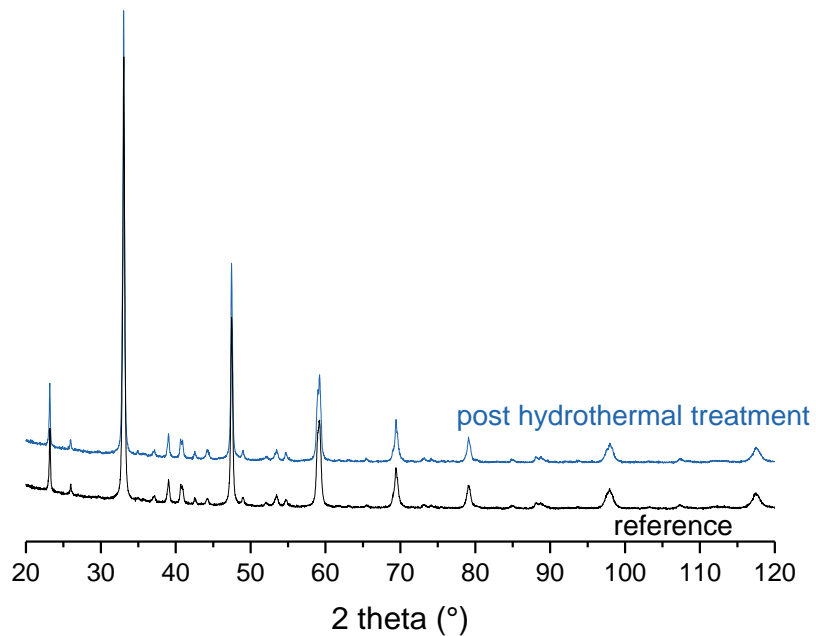


Figure 16: Normalized XRD patterns of a reference sample and a pellet after a hydrothermal treatment.

Conductivity measurements were performed on the pellet after the hydrothermal treatment and compared to a pristine CTF pellet to see if any change can be evidenced. Impedance spectroscopy was performed during heating or cooling between 130 °C and 700 °C (with a stabilization step of 2 hours) under air, and the Arrhenius plot of the total conductivity is shown in Figure 17.

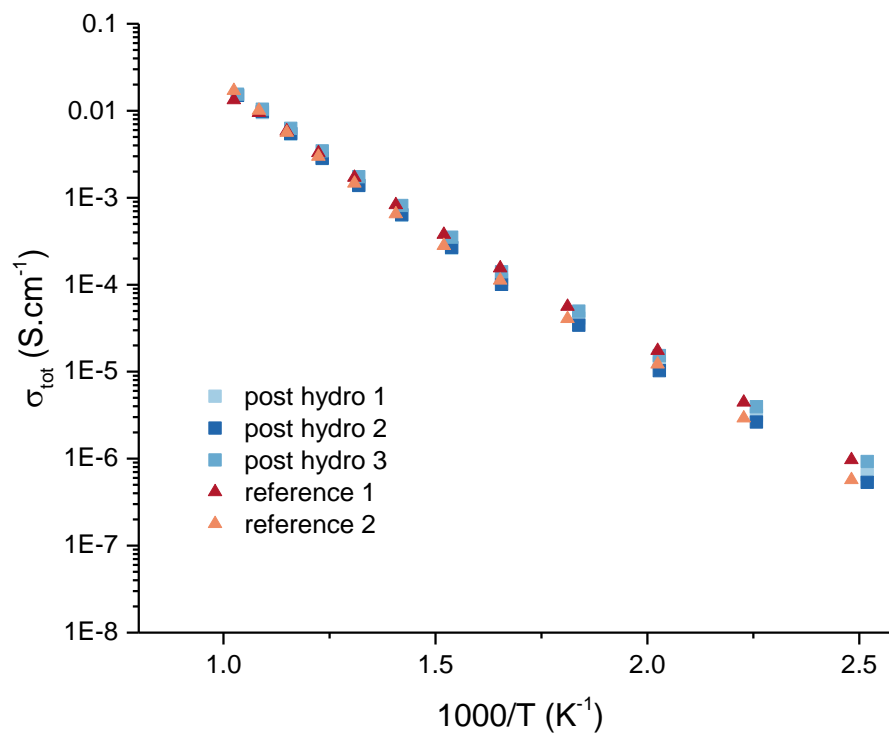


Figure 17: Total conductivity measured by impedance spectroscopy under air for a reference pellet and a pellet after hydrothermal treatment.

The measurement was made twice for each pellet and did not show major differences. Small differences can be evidenced at low temperature but the stabilization time was only 2 hours and the equilibrium may be no longer enough at low temperature.

With this experiment, no effect of water vapor on the microstructure and electrical properties of CTF pellet can be evidenced.

3.4 Effect of H₂

The effect of hydrogen on the oxygen semi-permeation was also investigated (Figure 18). Reduction was evidence under 3% H₂/Ar from 800 °C with the formation of metallic iron (Chapter 5).

However, during semi-permeation, the presence of oxygen changes the oxygen partial pressure because the oxygen reacts with H₂ to form water. Consequently, it is not possible to measure the oxygen partial pressure with the oxygen gauge when H₂ is sent on the lean side.

After 400 hours under CO₂ between 500 and 900 °C, atmosphere was changed to H₂ in the inner chamber for 80 hours. The gas tubing was heated to avoid any water adsorption. After that time, atmosphere was switched to CO₂ and only a slight decrease ($\approx 15\%$) of semi-permeation flux happened. However, no metallic iron was identified on the XRD analysis within the detection limit of the setup.

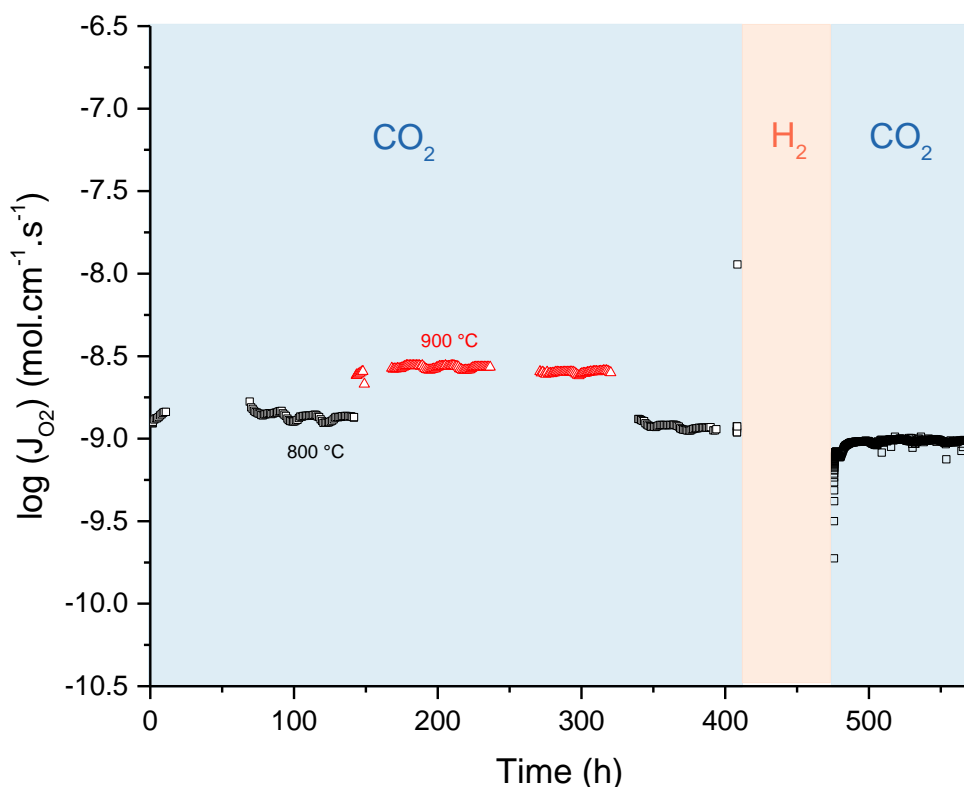


Figure 18: Oxygen semi-permeability flux as a function of time under CO₂ and H₂ atmospheres on the lean side.

3.5 Oxidation of methane

OTMs can be used as catalytic membrane reactor for the oxidation of methane for instance (cf. chapter 1). An experiment was performed on the CTF to study the stability of the membrane when methane is sent on

the lean side. Both the reductive atmosphere and the products formed during oxidation can damage the membrane. Indeed, even if the partial oxidation of methane is the desired reaction (Equation 1); total oxidation of methane (Equation 2) can occur. Water, hydrogen, carbon monoxide and carbon dioxide are then likely to be formed and can react with the membrane.



To be sure the CTF membrane will catalyze the CH_4 partial oxidation, a TPR (temperature programmed reduction) was done on CTF, sending 5% methane in helium while increasing temperature. The presence of hydrogen and carbon monoxide was evidence above 700 °C, approving the use of a CTF membrane without any catalyst to test the CTF stability (because it ensures that methane will oxidize and then form reactive gases).

5% methane was then sent on a CTF pellet with a porous layer on the lean side while oxygen was sent on the oxygen-rich side at 850 °C (Figure 19). The concentration of the reaction products as well as the methane content were followed by Mass Spectrometry (MS) (Figure 20) and Gas Chromatography (GC).

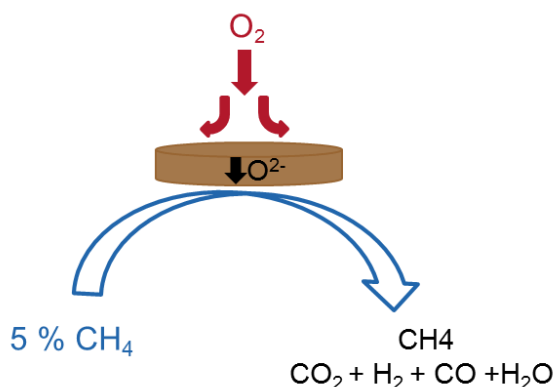


Figure 19: Schematic representation of the methane oxidation with the OTM.

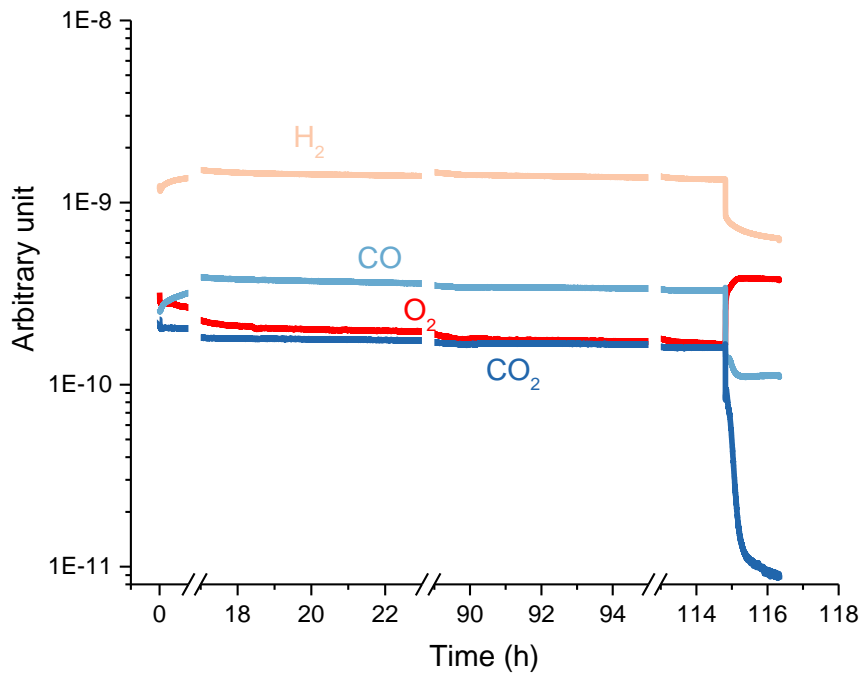


Figure 20: Evolution of the concentration of the product formed during the methane oxidation as a function of time measured by MS.

The concentration of the products was almost constant during the first hundred hours (the MS signal seems to decrease a bit but the calibration signal too).

Combining both the MS and GC results during the first 120 hours, ≈ 500 ppm of CH_4 reacted with 800 ppm of oxygen to form ≈ 110 ppm of CO and 220 ppm of H_2 during the partial oxidation of methane and 375 ppm of CO_2 during the total oxidation.

The membrane was under methane for 1000 hours. After around 500 hours, helium was sent briefly to measure the oxygen semi-permeability flux which was exactly the same than before introduction of methane (after 2 hours of equilibrium).

After 1000 hours, helium was introduced in the setup and the semi-permeability flux was measured as a function of temperature (Figure 21). The semi-permeability flux was the same than before methane exposure at 850°C and is very comparable to the reference membrane with porous layer, showing no specific degradation due to methane flow. However, surprisingly, the oxygen semi-permeability flux is higher at high temperature than the reference membrane.

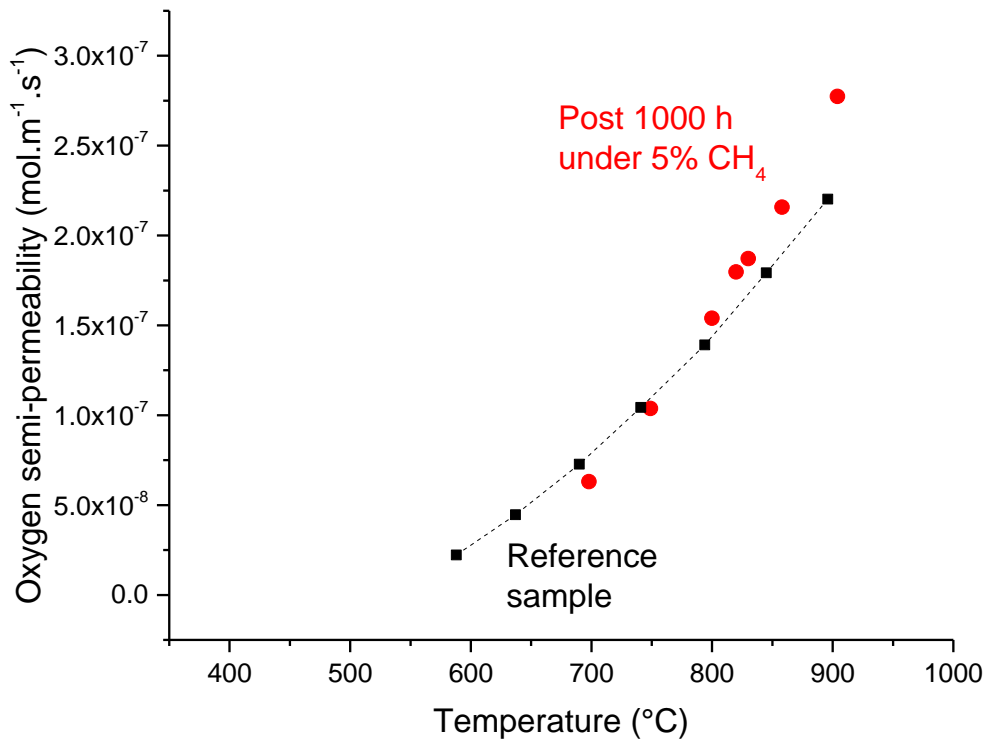
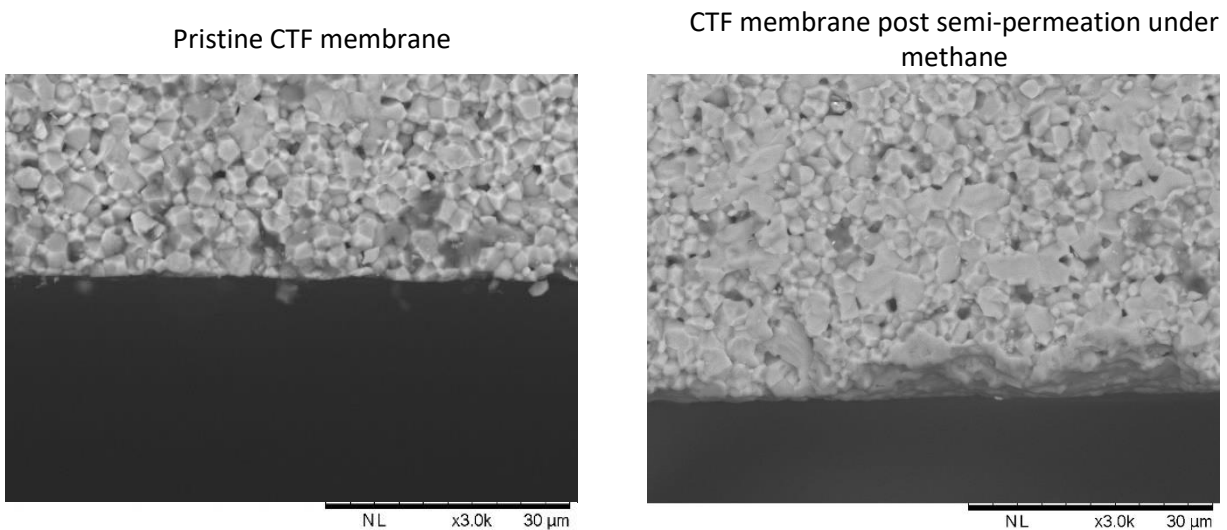


Figure 21: Oxygen semi-permeability flux as a function of temperature before and after 1000 h under 5% CH₄.

Post-mortem SEM and XRD analyses were done on the sample to study the effect of the reactive gases on the surface aspect and microstructure of the membrane. When CH₄ atmosphere reacts with the membrane, it can induce decomposition by reduction. Moreover, some cracks can appear due to the change in volume induced by the reduction (and the oxygen vacancies formation) [25]. Moreover, all the degradation due to CO₂, CO (i.e. carbonate formation, for instance) can also happen. SEM pictures of a fracture surface of a pristine CTF membrane and a membrane after semi-permeation under methane are represented in Figure 22. The grain size and the porosity remain roughly the same than on the pristine membrane.



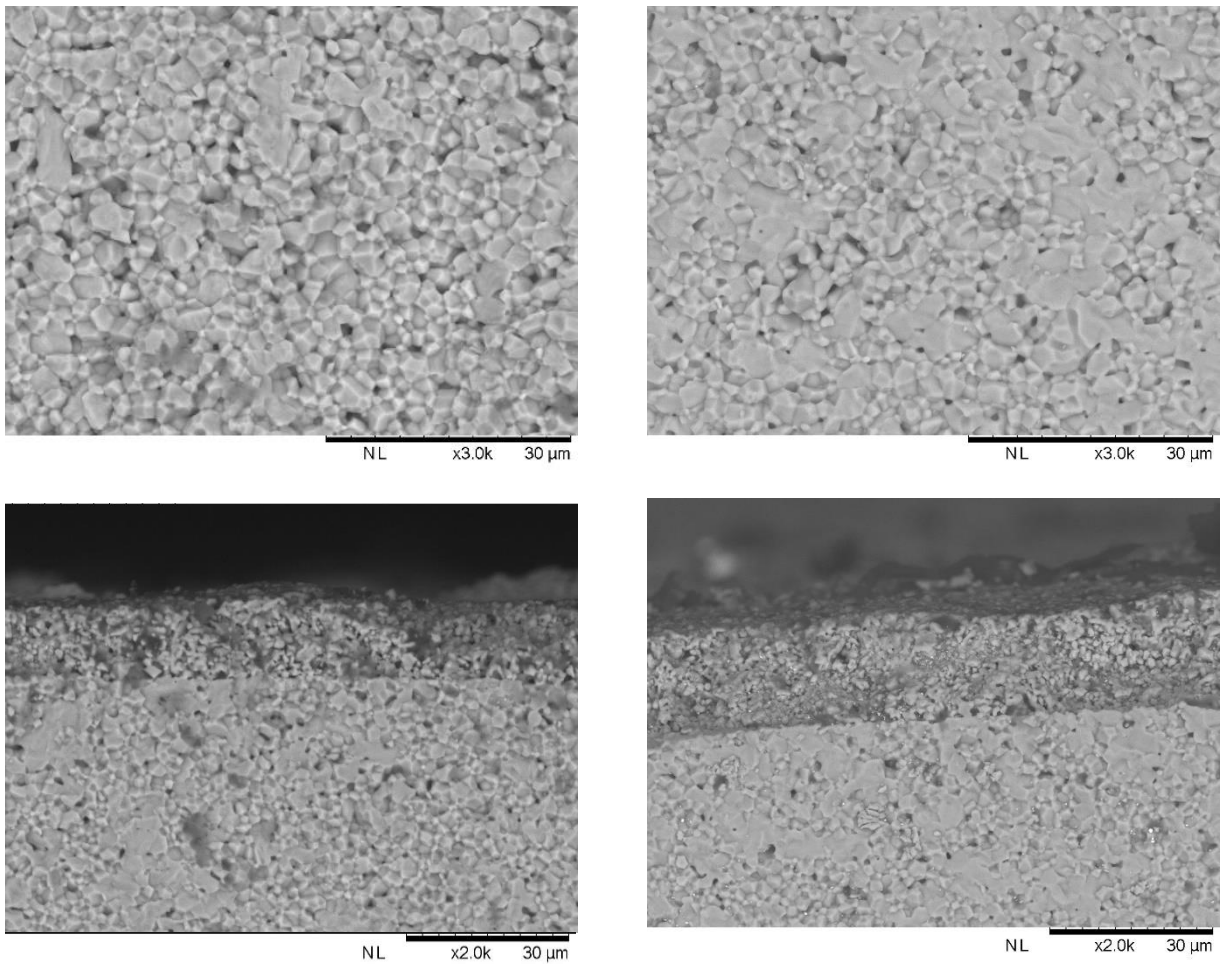


Figure 22: SEM images comparing a pristine membrane (left) with a CTF membrane after semi-permeation under methane during thousand hours (right).

Raman analyses were performed on the lean side surface (Figure 23) of a CTF pellet with a porous layer after thousand hours of semi-permeation under methane (top) or under argon (bottom). No peaks due to the presence of carbon are visible, only the one due to the perovskite structure, between 400 and 800 cm^{-1} were evidenced.

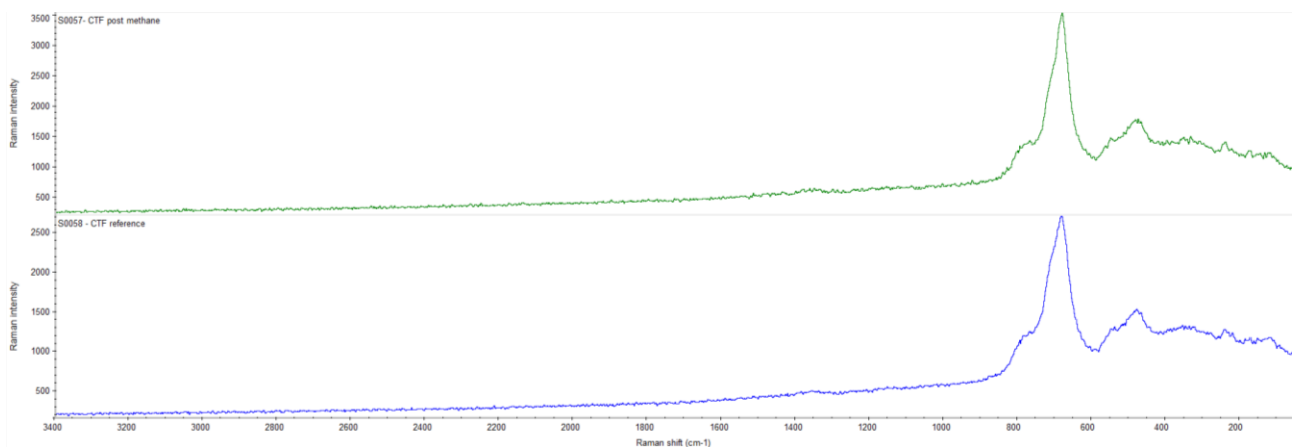


Figure 23: Raman analysis of the pellet post semi-permeation under methane (top) and a reference pellet post semi-permeation under argon (bottom). No peak due to the presence of carbon is visible, only the one due to the perovskite structure, between 400 and 800 cm^{-1} .

The XRD pattern of the membrane after the semi-permeation under methane is very similar to the one of a fired CTF pellet (Figure 24). Only an additional phase is indexed at 38.2°, corresponding to the diffraction peak of gold because a part of the gold seal was remaining on the membrane while performing the XRD analyses. No metallic iron was found indicating that the perovskite structure was not totally reduced to metallic iron.

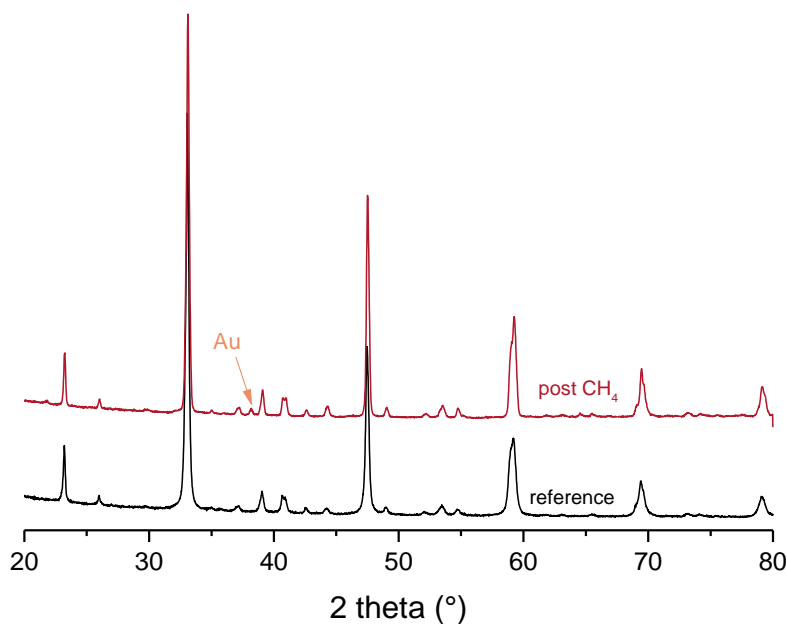


Figure 24: Normalized XRD patterns of a reference sample and the pellet after the semi-permeation under CH₄ for 1000 h.

There is no visible difference between the pristine membrane and the membrane after the semi-permeation under methane during thousand hours. This result confirms that no or a low degradation occurred and it is then a very promising result. It is interesting because it seems that the presence of CH₄ and its oxidation prevent the surface reduction which could happen at such low PO₂ (formation of metallic iron under H₂ at 850 °C). This behavior was already observed [26].

To be used for the partial oxidation of methane, study on the yield of the reaction and the selectivity between either the partial or the total oxidation of methane have to be performed. However, these results prove that the CTF membrane is stable under these reactive atmospheres and is then a material of choice for application under reactive atmospheres.

4. Redox stability potential

Redox stability measurements were performed on CTF10 samples. The aim of these experiments was mainly:

- to evaluate the impact of highly reducing atmospheres, either reduction by flowing hydrogen, or electrochemical reduction by passing an appropriate cathodic current (cf. chapter 2 § 7),
- to determine the potential of internal redox systems involved in the electrochemical process by using either a platinum or an iron measuring electrode,
- to study the possible aging after several reduction/reoxidation cycles.

4.1 Basic principle

The cell was briefly described in § 7 of Chapter 2. As previously recalled and illustrated in Figures 25 a to c, the method consists of two steps [27] :

- Firstly, the sample is chemically reduced, using a mixture of argon and hydrogen (Figure 25 a) or electrochemically reduced (Figure 25 b).
- Secondly, after interrupting the current (or the hydrogen flux), (argon with a few ppm of oxygen continuously flew through the setup), the relaxing open-circuit (o.c.) voltage of the cell with respect to the reference electrode, in contact with air (referred to as E (V/air) in Figure 25 c, is recorded during the slow reoxidation of the material by the traces of oxygen contained in argon.

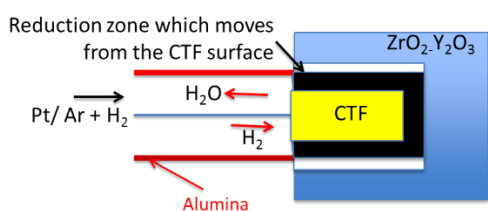


Figure 25 a: Principle of the chemical reduction by hydrogen.

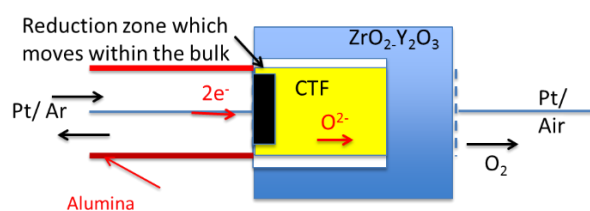


Figure 25 b: Principle of the electrochemical reduction.

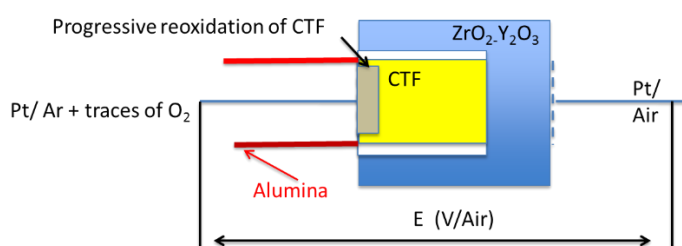


Figure 25 c: Principle of the electrochemical reoxidation (recording of E (V/Air) vs. time, during the reoxidation process).

A partial reduction of an oxide induces a valence change either of basic cations (Fe^{III} or Ti^{IV} in case of CTF, for example) or of a point defect (a dissolved impurity or a structural defect such as an oxide-ion vacancy). The main features associated with electrochemical reduction are: (i) a variation of the stoichiometry ratio due to oxygen release, (ii) a variation of the ionic and electronic conductivities, (iii) a coloration due to trapped electrons which can be excited to higher energy levels, (iv) a variation of the electrode potential which varies as a function of the reduction degree. The interpretation of the “waves” of reoxidation is often difficult and it was not the aim of this work to identify the redox couples responsible for the waves.

4.2 Electrochemical reduction (Pt electrode)

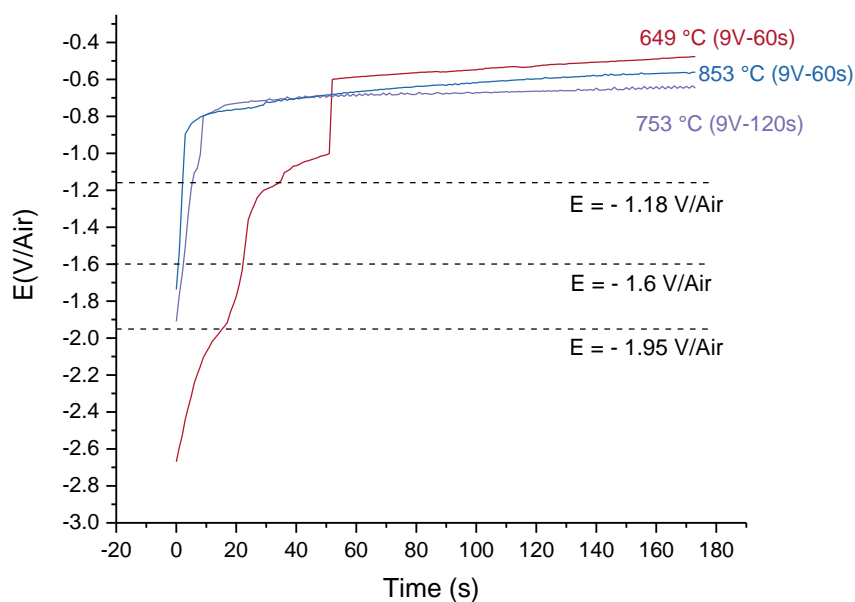


Figure 26: Examples of relaxation curves after electrochemical reduction.

Relaxations curves were recorded after electrochemical reduction and were plotted in Figure 26 for 649, 753 and 853 °C. It appears that the durations of the waves are very short, of the order of a few seconds, indicating that the buffer capacity of the redox systems involved in the reduction/reoxidation process is small. The zirconia tube was unchanged after many experiments, indicating that no reduction of the zirconia happened. Three waves are observed:

- The wave at - 1.95V/Air could be ascribed to the reduction of Zr^{4+} (YSZ tube) (which appears unlikely) or Ti^{4+} of the CTF sample;
- The wave at -1,6 V/Air could be ascribed to the electrochemical reduction of oxygen vacancies;
- The wave at - 1,18 V/Air and the following potential drop down to ca. - 0.6 V/Air seem to concern the CTF material.

It is interesting to note that the sample was partially covered with a shiny layer of metallic aspect which could be metallic iron.

4.3 Chemical reduction by hydrogen (Pt electrode)

Chemical reductions were carried out at various temperatures. Figure 27 gives examples of two different relaxation processes at 806°C, to evaluate the reproducibility of the results. It should be pointed out that, obviously, reducing by hydrogen cannot induce a reduction of the zirconia tube. The experimental error in the wave potential determination is of the order of 100 mV.

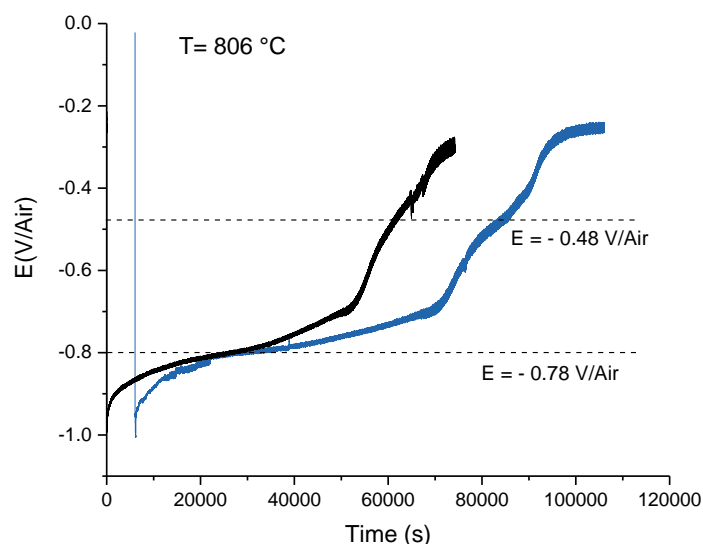


Figure 27: Examples of relaxation curves after chemical reduction by hydrogen.

4.4 Chemical and electrochemical reduction using iron electrode

To correlate the wave potentials with the redox couples involving iron, the setup was modified as illustrated in Figure 28; replacing the current lead from platinum to an iron wire.

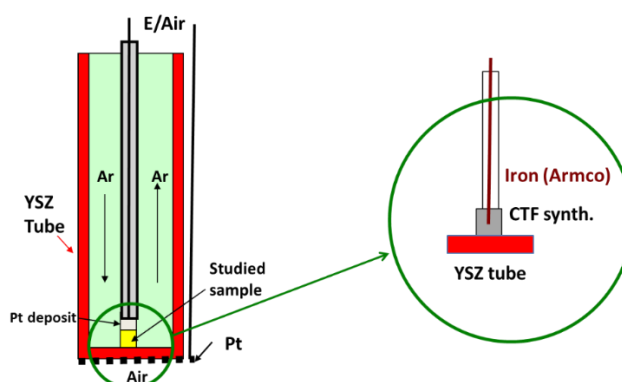


Figure 28: Schematic drawing of the setup including a Fe current lead.

Figure 29 and Figure 30 give examples of reoxidation curves after electrochemical and chemical reduction by hydrogen. The chemical reduction by hydrogen requires a sufficiently high temperature, that was not the case for the electrochemical reduction. For temperatures lower than 650 °C, the emf was - 0.35 V/Air, indicating that the iron wire was partially oxidized. On the other hand, with a high oxygen pressure in the setup during the reoxidation process, the cell voltage leads to a plateau at - 0.35 V/Air, meaning that metallic iron may not be involved, and then that the plateau at - 0,35 V/Air could correspond to the couple Fe^{II} / Fe^{III} .

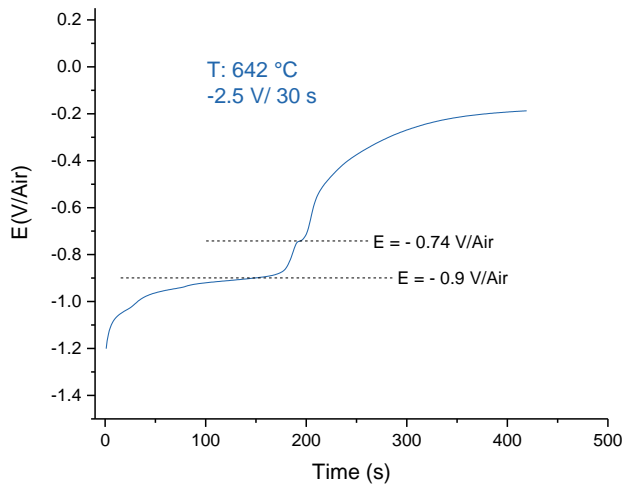


Figure 29: Example of reoxidation curve after electrochemical reduction.

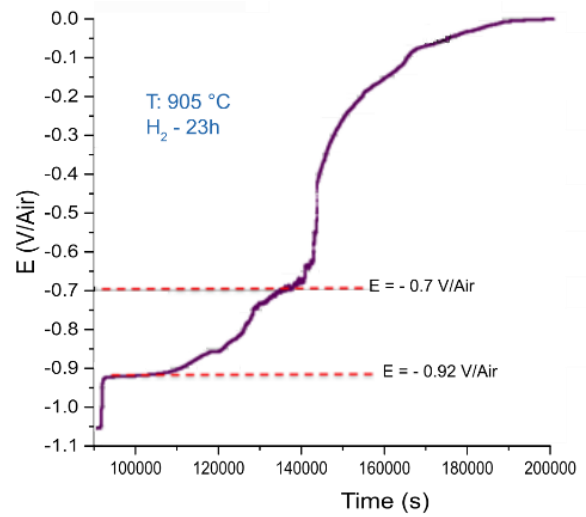


Figure 30: Example of reoxidation curve after chemical reduction by hydrogen.

4.5 First synthesis of the results

Figure 31 sums up all the potentials of the waves obtained, as a function of temperature.

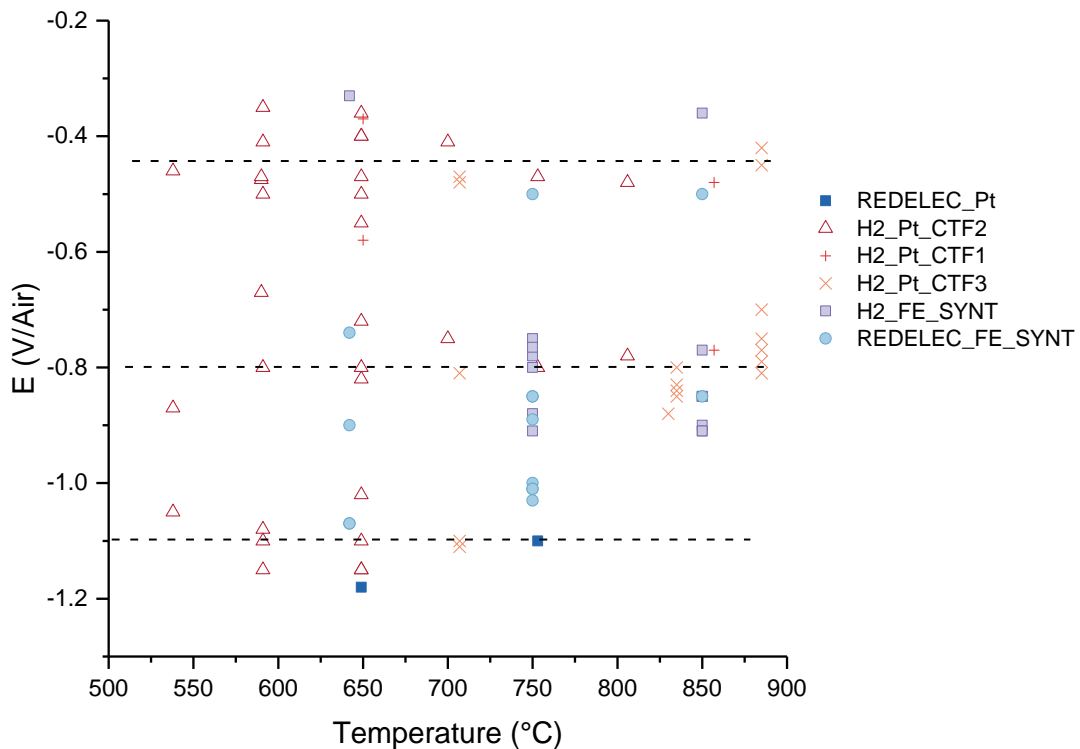


Figure 31: Reoxidation potentials of CTF10 as a function of temperature.

(REELEC_Pt and REDELEC-Fe: electrochemical reduction with Pt and Fe electrode, respectively, H2_Pt_CTF and H2_FE: chemical reduction of CTF10 with Pt and Fe current lead, respectively).

It can be concluded that, despite an experimental uncertainty of ± 100 mV, 3 reduction potentials can be found: at - 0,45 V/air, - 0,8 V/air and - 1,1 V/air. The potentials of the waves are the same, whatever the current lead (Pt or Fe), which could indicate that all the redox systems involved concern iron species. Furthermore, these results confirm the formation of metallic iron in highly reducing atmosphere.

Moreover, more than 150 “reduction/reoxidation” cycles were carried out, without modification of the results, confirming that the material is highly resistant to reduction.

5. Conclusion

The long-term stability of CTF was studied. First, CTF showed a very nice stability under non-reactive atmosphere for more than thousand hours. A maximal difference of 6% of oxygen semi-permeation flux was found whereas for BSFC for instance, after 1000 hours, the oxygen semi-permeation flux already decreased by 66%.

Moreover, it is important to study the stability under more reactive atmospheres typically found in standard operating conditions. Consequently, CO₂ as well as CO atmospheres were flowed on a CTF membrane and its stability was assessed. The semi-permeation under these atmospheres did not reveal a particular degradation, neither the SEM, EDS and XRD analyses. CTF was then not degraded under 1% CO₂ and 2% CO after 1200 hours. However, the presence of water vapor and CO₂ induced a degradation on the semi-permeation flux (\approx - 35% of oxygen semi-permeation flux), but it was totally recovered under helium sweeping. It was concluded that this decreased in term of flux was either due to a competition between the oxygen activity and the adsorption of other compounds (carbonates for instance) or a surface degradation which is totally reversible under helium sweeping.

Then, the effect of hydrogen was also assessed at 800 °C. It was showed previously (chapter 5) that a reduction of CTF under hydrogen happen, which could explain the slight decrease (\approx 15%) of semi-permeation flux observed.

Finally, the stability of CTF under methane atmosphere was assessed. Despite the presence of methane but also CO, CO₂, H₂O, and H₂ formed during the partial or total oxidation of methane, the semi permeation flux of the CTF membrane remained exactly the same at 850 °C after 1000 hours. No presence of metallic iron was found in Raman or XRD analyses and the SEM analyses did not reveal any degradation.

CTF appears then as a material full of promises with a very high stability, especially under methane which can be very interesting for some applications.

Finally, the redox stability potential on CTF samples were calculated. Despite an experimental uncertainty of \pm 100 mV, 3 wave potentials were found: at - 0,45 V/air, - 0,8 V/air and - 1,1 V/air. However, it is important and very interesting to note that the material is highly resistant to reduction, showing no particular degradation after more than 150 reduction/reoxidation cycles.

- [1] X. Li, Long term stability and permeability of mixed ion conducting membranes under oxyfuel conditions, Aachen University, 2013.
- [2] M.F. Carolan, P.N. Dyer, S.M. Fine, J.M. LaBar Sr., R.M. Thorogood, Process for recovering oxygen from gaseous mixtures containing water or carbon dioxide which process employs ion transport membranes, (1992).
- [3] M.F. Carolan, P.N. Dyer, J.M. LaBar Sr., R.M. Thorogood, Process for recovering oxygen from gaseous mixtures containing water or carbon dioxide which process employs ion transport membranes, (1992).
- [4] J. Sunarso, S. Baumann, J.M. Serra, W.A. Meulenberg, S. Liu, Y.S. Lin, J.C. Diniz da Costa, Mixed ionic – electronic conducting (MIEC) ceramic-based membranes for oxygen separation, *J. Memb. Sci.* 320 (2008) 13–41.
- [5] Z. Shao, W. Yang, Y. Cong, H. Dong, J. Tong, G. Xiong, Investigation of the permeation behavior and stability of a $\text{Ba}_{0.5}\text{Sr}_{0.5}\text{Co}_{0.8}\text{Fe}_{0.2}\text{O}_{(3-\delta)}$ oxygen membrane, *J. Memb. Sci.* 172 (2000) 177–188.
- [6] A.V. Kovalevsky, A.A. Yaremchenko, V.A. Kolotygin, F.M.M. Snijkers, V.V. Kharton, A. Buekenhoudt, J.J. Luyten, Oxygen permeability and stability of asymmetric multilayer $\text{Ba}_{0.5}\text{Sr}_{0.5}\text{Co}_{0.8}\text{Fe}_{0.2}\text{O}_{3-\delta}$ ceramic membranes, *Solid State Ionics.* 192 (2011) 677–681.
- [7] M. Arnold, H. Wang, A. Feldhoff, Influence of CO_2 on the oxygen permeation performance and the microstructure of perovskite-type $(\text{Ba}_{0.5}\text{Sr}_{0.5})(\text{Co}_{0.8}\text{Fe}_{0.2})\text{O}_{3-\delta}$ membranes, *J. Memb. Sci.* 293 (2007) 44-52.
- [8] A. Leo, S. Liu, J.C. Diniz Da Costa, Production of pure oxygen from BSCF hollow fiber membranes using steam sweep, *Sep. Purif. Technol.* 78 (2011) 220–227.
- [9] S.F.P. Donkelaar, Development of Stable Oxygen Transport Membranes, Twente University, 2015.
- [10] F. Schulze-Küppers, S.F.P. ten Donkelaar, S. Baumann, P. Prigorodov, Y.J. Sohn, H.J.M. Bouwmeester, W.A. Meulenberg, O. Guillon, Structural and functional properties of $\text{SrTi}_{1-x}\text{Fe}_x\text{O}_{3-\delta}$ ($0 \leq x \leq 1$) for the use as oxygen transport membrane, *Sep. Purif. Technol.* 147 (2015) 414–421.
- [11] J. Garcia-Fayos, V.B. Vert, M. Balaguer, C. Solís, C. Gaudillere, J.M. Serra, Oxygen transport membranes in a biomass/coal combined strategy for reducing CO_2 emissions: Permeation study of selected membranes under different CO_2 -rich atmospheres, *Catal. Today.* 257 (2015) 221–228.
- [12] F.M. Figueiredo, M.R. Soares, V.V. Kharton, E.N. Naumovich, J.C. Waerenborgh, J.R. Frade, Properties of $\text{CaTi}_{1-x}\text{Fe}_x\text{O}_{3-\delta}$ Ceramic Membranes, *J. Electroceramics.* 13 (2004) 627–636.
- [13] Y. Chen, N. Galinsky, Z. Wang, F. Li, Investigation of perovskite supported composite oxides for chemical looping conversion of syngas, *Fuel.* 134 (2014) 521–530.
- [14] M. Balaguer, S. Escolástico, J.M. Serra, Oxygen permeation and stability of $\text{CaTi}_{0.73}\text{Fe}_{0.18}\text{Mg}_{0.09}\text{O}_{3-\delta}$ oxygen-transport membrane, *J. Memb. Sci.* 524 (2017) 56–63.
- [15] V.V. Kharton, A.V. Kovalevsky, A.P. Viskup, F.M. Figueiredo, A.A. Yaremchenko, E.N. Naumovich, F.M.B. Marques, Oxygen permeability and faradaic efficiency of $\text{Ce}_{0.8}\text{Gd}_{0.2}\text{O}_{2-d}-\text{La}_{0.7}\text{Sr}_{0.3}\text{MnO}_{3-d}$ composites, *J. Eur. Ceram. Soc.* 21 (2001) 1763–1767.
- [16] K. Efimov, T. Klande, N. Juditzki, A. Feldhoff, Ca-containing CO_2 -tolerant perovskite materials for oxygen separation, *J. Memb. Sci.* 389 (2012) 205–215.
- [17] Z. Zhang, D. Chen, F. Dong, X. Xu, Y. Hao, Z. Shao, Understanding the doping effect toward the design of CO_2 -tolerant perovskite membranes with enhanced oxygen permeability, *J. Memb. Sci.*

519 (2016) 11–21.

- [18] J. Yi, M. Schroeder, T. Weirich, J. Mayer, Behavior of Ba(Co, Fe, Nb)O_{3-δ} Perovskite in CO₂-Containing Atmospheres: Degradation Mechanism and Materials Design, *Chem. Mater.* 22 (2010) 6246–6253.
- [19] Z. Zhang, D. Chen, F. Dong, Z. Shao, Efficient and CO₂-tolerant oxygen transport membranes prepared from high-valence B-site substituted cobalt-free SrFeO_{3-δ}, *J. Memb. Sci.* 495 (2015) 187–197.
- [20] M.C. Steil, J. Fouletier, P.-M. Geffroy, Surface exchange polarization vs. gas concentration polarization in permeation through mixed ionic-electronic membranes, *J. Memb. Sci.* 541 (2017) 457–464.
- [21] H. Cheng, P. Wang, H. Zhao, K. Li, X. Lu, Q. Xu, Synthesis, CO₂-tolerance and rate-determining step of Nb-doped Ce_{0.8}Gd_{0.2}O_{2-δ}-Pr_{0.6}Sr_{0.4}Co_{0.5}Fe_{0.5}O_{3-δ} ceramic membranes, *Ceram. Int.* 43 (2017) 6477–6486.
- [22] I. Kaus, K. Wiik, B. Krogh, M. Dahle, K.H. Hofstad, S. Aasland, Stability of SrFeO₃-Based Materials in H₂O/CO₂-Containing Atmospheres at High Temperatures and Pressures, *J. Am. Ceram. Soc.* 90 (2007) 2226–2230.
- [23] A. Yan, B. Liu, Y. Dong, Z. Tian, D. Wang, M. Cheng, A temperature programmed desorption investigation on the interaction of Ba_{0.5}Sr_{0.5}Co_{0.8}Fe_{0.2}O_{3-δ} perovskite oxides with CO₂ in the absence and presence of H₂O and O₂, *Appl. Catal. B Environ.* 80 (2008) 24–31.
- [24] M.A. Henderson, Evidence for bicarbonate formation on vacuum annealed TiO₂(110) resulting from a precursor-mediated interaction between CO₂ and H₂O, *Surf. Sci.* 400 (1998) 203–219.
- [25] H.J.M. Bouwmeester, Dense ceramic membranes for methane conversion, *Catal. Today.* 82 (2003) 141–150.
- [26] A. Löfberg, S. Boujmiaï, E. Capoen, M.C. Steil, C. Pirovano, R.N. Vannier, G. Mairesse, E. Bordes-Richard, Oxygen permeation versus catalytic properties of bismuth-based oxide ion conductors used for propene oxidation in a catalytic dense membrane reactor, *Catal. Today.* 91–92 (2004) 79–83.
- [27] S. Boulfrad, E. Djurado, J. Fouletier, Electrochemical characterization of nanostructured zirconias, *Solid State Ionics.* 180 (2009) 978–983.

CONCLUSIONS AND PERSPECTIVES

A specific setup was used to determine the limiting steps of semi-permeation through a CTF membrane. It appeared that the oxygen semi-permeability flux of the CTF membrane was mixed limited (both by surface exchange reactions and bulk diffusion) at low temperature but was mainly limited by the bulk diffusion at temperature higher than 750 °C. These findings were confirmed with other experiments such as isotopic exchange and measurements of the oxygen semi-permeability flux of membranes with a porous layer deposited on the membrane surface. Indeed, isotopic exchange confirmed that the critical thickness, L_c , decreases with temperature increase, meaning that the semi-permeation process becomes mainly limited by bulk diffusion when temperature increases. Moreover, using a porous layer to increase the surface exchange on the oxygen-lean side enabled to increase the oxygen semi-permeability flux at low temperature, where it was found that the flux was mixed limited. The B_c parameter of these membranes confirms that the porous coating changes the limitation from a mixed process (for a bare membrane) to a process limited by oxygen diffusion below 750 °C.

However, for all temperatures, it was evidenced that the surface had a limiting effect, approving the need to use the oxygen activity instead of the oxygen partial pressure of the gas to characterize the oxygen semi-permeation, unless using complex model taking into account the effect of the surface.

The defect chemistry of the CTF was studied and an important work was done on the CTF conductivity. Indeed, in semi-permeation, it was found that the flux was limited by the ionic conductivity at low temperature but was limited by the electronic conductivity at high temperature. A study on the total conductivity of the CTF was performed and evidenced that the ionic transport number increased with increasing temperature. This is especially due to the higher activation energy of the ionic conductivity (≈ 0.9 eV) compared to the activation energy of the electron hole conductivity (≈ 0.5 eV) calculated via a simple defect model. However, this model assumes that the ionic conductivity is constant over a wide range of P_{O_2} and then ionic conductivity was measured on the plateau of the ionic conductivity curves as a function of P_{O_2} (i.e. at a P_{O_2} between 10^{-15} and 10^{-5} bar).

However, under low P_{O_2} , the CTF can be reduced, changing its concentration of oxygen vacancies, responsible of the ionic conductivity. A study of the oxygen non-stoichiometry, δ , as a function of P_{O_2} was also performed. It was found that under atmospheric pressure $\approx 20\%$ of Fe^{IV} were present in the material leading to a $\delta = 0.04$. These Fe^{IV} ions were reduced when P_{O_2} decreases, and were no more present at 600 °C, after a reduction under 3% H_2 . Under these conditions, only Fe^{III} were found in the material, leading to a $\delta = 0.05$. Under more reductive conditions, for temperature higher than 800 °C, metallic iron was observed (27% of metallic iron after 1 hours at 1000 °C under 3% H_2).

Considering that $\delta = 0.04$ under air, the ionic conductivity was calculated from different methods. For all these methods (isotopic exchange, semi-permeation, impedance spectroscopy), the same activation energy (≈ 0.9 eV) was found. However, the values were 2 to 3 times higher with impedance spectroscopy compared to the other methods. It was assumed that the oxygen partial pressure at which the ionic conductivity was measured was responsible of this difference. However, only the difference in concentration of oxygen vacancy by itself could not imply such a difference of ionic conductivity. It was assumed that the change of

local environment of the iron on the CTF lattice while reducing could influence the concentration of mobile oxygen vacancies and/or their mobility, explaining such a change in ionic conductivity.

The evolution of ionic conductivity as a function of P_{O_2} was calculated using the total conductivity obtained by impedance spectroscopy and the ionic conductivity calculated under air by isotopic exchange. It appeared that the ionic conductivity increased while decreasing the P_{O_2} and stabilized in a plateau close to the ionic conductivity determined in impedance spectroscopy between 10^{-15} - 10^{-5} bar.

Another important part of this work was the study of the long-term stability, especially under reactive atmospheres. First, the long-term stability under non-reactive atmospheres was studied, revealing the good properties of the CTF which was very stable. Only, a decrease of 6% of the semi-permeability flux was observed after more than 1000 h of semi-permeation. Compared to the BSCF for instance, which decreased by 66% after 1000 h, the CTF appeared as a very stable material.

The stability under more reactive atmosphere was also assessed, to fulfill with typical atmosphere found in standard operating conditions. No degradation was observed (in term of flux, microstructure...) after 1200 hours under 1% CO_2 and 2% CO. However, a slight decreased (\approx - 35% of oxygen semi-permeation flux), was observed in the presence of water vapor and CO_2 , but this was totally reversible and the same semi-permeation flux was recovered after sweeping helium. This can be due to the adsorption of compounds on the surface which prevent the oxygen activity or a surface degradation but the bulk was not degraded as it could happen for the BSCF for instance.

Finally, the effect of methane atmosphere on the CTF was assessed, which could be interesting for potential application as catalytic membrane reactor for instance. During 1000 hours, methane was flowed on a CTF pellet, and was partially or totally oxidized, forming CO, CO_2 , H_2O , and H_2 . Despite the presence of all these components and the reductive atmosphere, the same permeation flux was recovered after flowing back helium. No presence of metallic iron was evidenced in Raman or XRD analyses and the SEM analyses did not reveal any degradation. It is interesting because it seems that the presence of CH_4 and its oxidation prevent the surface reduction which could happen at such low PO_2 (formation of metallic iron under H_2 at 850 °C).

Consequently, despite relatively low performance (5×10^{-3} mL.min⁻¹.cm⁻¹ at 900 °C), CTF appears then as a material full of promises with a very high stability, especially under methane which can be very interesting for some applications.

Some additional work can be done, especially the study of the stability under SO_2 , which can be present as pollutant in industrial applications. A complete study of the partial and total oxidation of methane (and a work on the selectivity of the reactions) has also to be performed.

Moreover, the flux performance could be improved when increasing slightly the iron content. Experiments were performed on $CaTi_{0.8}Fe_{0.2}O_{3-6}$ (CTF20) which was supposed to have a higher ionic conductivity.

ANNEXE 1: CTF20

Experiments were performed on $\text{CaTi}_{0.8}\text{Fe}_{0.2}\text{O}_{3-\delta}$ (CTF20) which was supposed to have a higher ionic conductivity. The powder was synthesized via a modified Pechini synthesis and was referred to as CTFsc (cf. chapter 3 §5). It was compared to the powder synthesized via electrofusion referred to as CTF-SG.

Total conductivity of CTF-SG, CTFsc10 and CTFsc20 were measured by impedance spectroscopy (Figure 1).

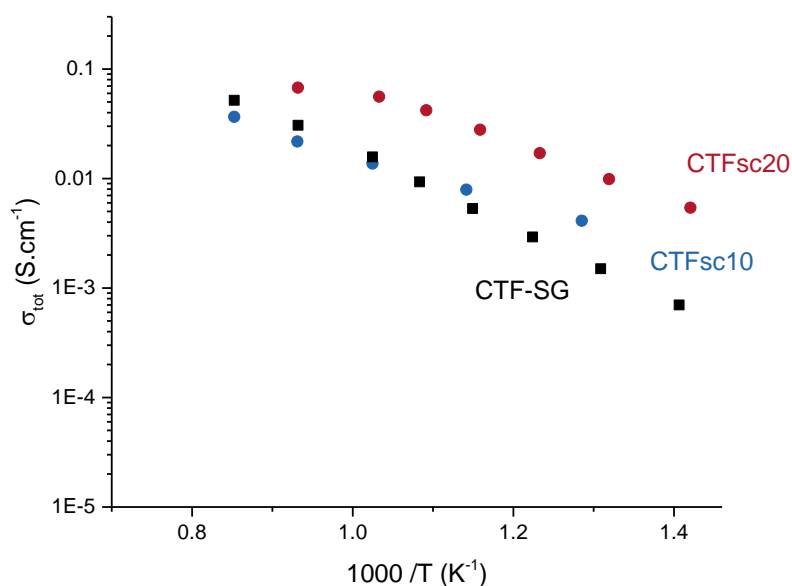


Figure 1 : Total conductivity as a function of temperature of CTF-SG, CTF-sc10 and CTF-sc20 obtained by impedance spectroscopy.

The total conductivity of CTFsc20 was higher than the one of CTF10 as expected [1,2], however, it was not possible yet to determine the ionic conductivity and the ambipolar conductivity with this preliminary experiments.

However, a first experiment in semi-permeation was performed with CTF20 and results are plotted in Figure 2.

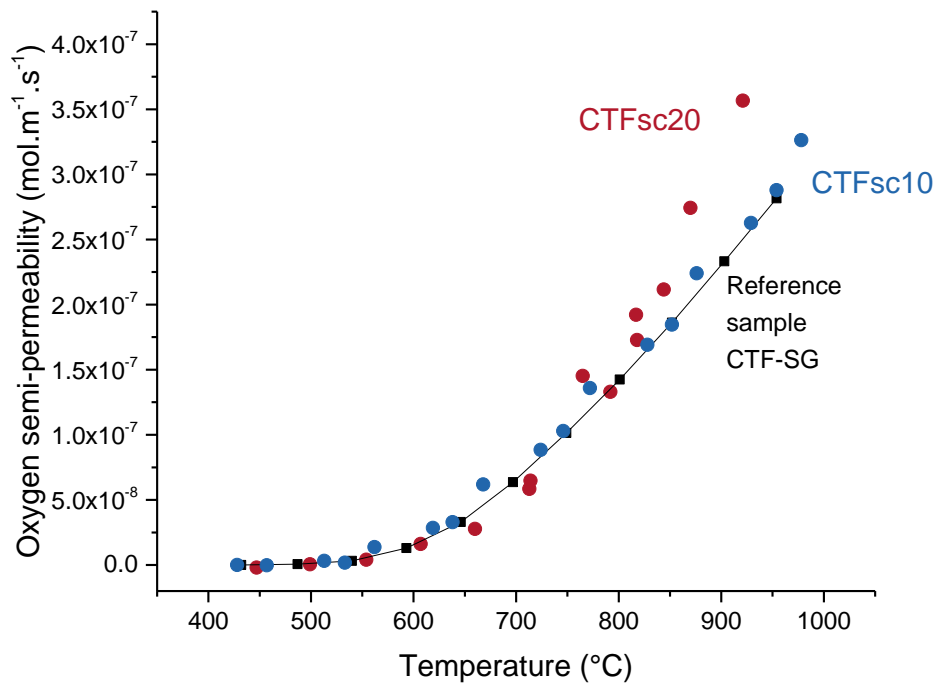


Figure 2 : Oxygen semi-permeability flux as a function of temperature for CTF-SG, CTFsc10 and CTFs20.

Results are similar at low temperature but it can be explained because at temperature lower than 700 °C, $B_c < 0.5$ meaning that the flux is mixed limited. But for $T > 700$ °C, only a slight increase of semi-permeability flux for CTF20 is visible. Knowing that the total conductivity is at least 3 times higher for CTF20 than for CTF10 at $T < 800$ °C, a higher difference in semi-permeation flux is expected....

More experiments have to be performed to fully understand the semi-permeation of the CTF20 (especially determining the ionic and ambipolar conductivity) and the long-term stability has to be studied because if the performances increase, it may decrease the stability.

- [1] S. Marion, A.I. Becerro, T. Norby, Ionic and electronic conductivity in $\text{CaTi}_{1-x}\text{Fe}_x\text{O}_{3-\delta}$ ($x = 0.1-0.3$), *Ionics* (Kiel). 5 (1999) 385–392.
- [2] L.A. Dunyushkina, A.K. Demin, B. V Zhuravlev, Electrical conductivity of iron-doped calcium titanate, *Solid State Ionics*. 116 (1999) 85–88.